Edge Biasing in the WEGA Stellarator

vorgelegt von

Oliver Lischtschenko

geboren am 18.12.1979

in Berlin, Spandau

Greifswald, den 27. November 2008

Dekan: _____

1. Gutachter: _____

2. Gutachter: _____

Tag der Promotion: _____

Zusammenfassung der Dissertation

zum Thema "Edge Biasing in the WEGA Stellarator"

vorgelegt von

Oliver Lischtschenko

Experimente zur Plasmapolarisation erlaubten eine Leistungssteigerung in modernen Tokamaks und Stellaratoren [KTT$^+$06b, VGM$^+$01]. Es konnte gezeigt werden, dass der Einsatz von vorgespannten Divertoren die Leistung verbessern und die Beherrschbarkeit des Divertorplasmas vereinfachen kann [RTH$^+$97, SLM$^+$91]. Ein anderer Aspekt ist, dass der Zugang zum H-Mode-Regime vereinfacht wird, da Plasmapolarisation die Leistungsgrenze zum H-Mode-Regime reduziert [JOWB98, WOB$^+$92].

In Rahmen der vorliegenden Arbeit an dem Greifswalder Stellarator WEGA wurden grundlegende Experimente zur Plasmapolarisation durchgeführt, welche die Möglichkeiten zur Modifikation des radialen elektrischen Feldes im Plasma demonstrieren.

Auf Grund der geringen verfügbaren Heizleistung von maximal 26 kW an WEGA und der vergleichsweise hohen H-Mode Leistungsgrenze von ca. 100 kW an erforderlicher Heizleistung kann die WEGA nicht in der H-Mode oder in der Nähe des H-Mode-Übergangs betrieben werden. Typische Plasmadichten für den Niedrigfeldbetrieb mit Argon an WEGA liegen bei $n_e \approx 10^{18}\,\mathrm{m}^{-3}$. Typische Elektronentemperaturen liegen zwischen 4 und 12 eV. Als Heizquelle fungieren 2,45 GHz Mikrowellengeneratoren, welche via OXB-Modenkonversion das Plasma heizen.

Es ist bekannt, dass die Verscherung des radialen elektrischen Feldes, zum Beispiel, Einfluss auf Plasmaturbulenz hat [HPD$^+$04, HDH$^+$99, II88, Ram05, VGM$^+$01]. In dieser Arbeit liegt der Schwerpunkt auf dem Einfluss der Polarisationssonde auf das radiale elektrische Feld und anderen Plasmaparameter. In dem WEGA Stellarator ist eine Entladungsart gewählt worden, die nur wenig Turbulenz zeigt, um möglichst ungestörte Messungen der Auswirkungen der Polarisation zu erhalten.

Im Gegensatz zu anderen Plasmapolarisationsexperimenten sind in der WEGA die Argonionen des Plasmas nicht durch das magnetische Feld eingeschlossen. Diese bisher nicht betrachtete Kombination macht Polarisationsexperimente an WEGA einzigartig.

Der Einsatz einer großen emissiven Polarisationssonde führte zu einer Erhöhung der Zentraldichte, wie auch zu steileren Randgradienten. Dies konnte allerdings dem Betrieb der Sonde in Emission und nicht dem Vorspannen der Sonde zugeschrieben werden. Durch positives Vorspannen der Polarisationssonde konnte das radiale elektrische Feld am Plasmarand von anfangs $E_r = 40\,\frac{\text{V}}{\text{m}}$ auf etwa $120\,\frac{\text{V}}{\text{m}}$ angehoben werden. Hierbei zeigt sich eine lineare Abhängigkeit des elektrischen Feldes vom Polarisationsstrom. Ein vergleichbares Verhalten wurde auch in anderen Polarisationsexperimenten beobachtet [WOB+92, VGM+01].

Bei Vorspannungen größer als $U_{bias} = +60\,\text{V}$ wurde der Übergang in einen anderen Plasmazustand beobachtet. Dieser, im Folgenden als dichter und heißer Zustand bezeichnete, Zustand weist deutlich höhere Plasmadichten und Temperaturen auf. Erstmalig konnte auf diese Art eine Elektronentemperatur größer als 20 eV im Niedrigfeldbetrieb in Argon in der WEGA etabliert werden. Das radiale elektrische Feld im dichten, heißen Zustand ist niedriger als im vergleichbaren weniger dichten, kälteren Plasmazustand. Dies ist zunächst nicht ungewöhnlich, da im dichteren und heißeren Zustand ein geringerer Strom über die Polarisationssonde fließt. Genauer betrachtet ist das radiale elektrische Feld aber deutlich geringer als bei vergleichbarem Strom im weniger dichten Zustand. Es zeigt sich überdies ein Einfluss des sich in der fernen Abschälschicht befindlichen Limiters. Während sich mit eingebautem Limiter ein sprunghafter Übergang vom weniger dichten in den dicheren und heißeren Zustand zeigt, wird im Falle ohne Limiter eine kontinuierliche Entwicklung des dichten, heißen Plasmazustandes beobachtet. Eine Destabilisierung des dichten, heißen Zustandes konnte bei ausgebautem Limiter nur bei deutlich reduzierter Heizleistung und erhöhtem Neutralgasdruck erzielt werden.

Verglichen mit dem weniger dichten Zustand konnte im dichten, heißen Zustand eine Erhöhung der eingeschlossen Energie um einen Faktor 2 erzielt werden. Im direkten Vergleich mit der nicht vorgespannten Entladung beträgt die Steigerung noch 40%. Dies liegt im Bereich dessen, was an Experimenten mit Turbulenzreduktion und Übergängen in H-Mode-Plasmen erzielt wurde. Da eine weitere Reduktion der Turbulenz ausgeschlossen werden kann, ja sogar das Turbulenzniveau steigt, muss ein anderer Mechanismus die Ursache hierfür sein.

Da der dichte, heiße Zustand eine Leistungsskalierung zeigt, wie sie auch von den Standardentladungen bei Erhöhung der Heizleistung beobachtet wird, wird dieser Aspekt zunächst untersucht. Hierzu werden mittels zwei Modellen die Teilchen- und Energiebilanz betrachtet. Da die Mikrowellenheizung die einzige Quelle ist, muss sie sämtliche Verlustprozesse bilanzieren. Mittels der Modelle lässt sich so die insge-

samt absorbierte Mikrowellenleistung ermitteln und eine Aussage zur Heizeffizienz tätigen, welche sonst nur schwer zugänglich ist. Durch den Vergleich der beiden Plasmazustände kann gezeigt werden, dass die Heizeffizienz von $\eta_{mw} \approx 30\,\%$ - für nichtvorgespannte Entladungen, sowie der vorgespannten weniger dichten Zustände - auf Werte von größer als $80\,\%$ im Falle des dichten, heißen Zustandes gesteigert werden kann. Der betrachtete Übergang kann daher einer Effizienzsteigerung der Mikrowellenheizung zugeschrieben werden.

Abstract to the Thesis

"Edge Biasing in the WEGA Stellarator"

submitted by

Oliver Lischtschenko

Biasing experiments are reported to improve the performance of tokamaks and stellarators [KTT+06b, VGM+01]. It has been shown that biased divertors perform more efficient and achieve a better control over the divertor plasma [RTH+97, SLM+91]. Biasing is applied in plasma fusion research in order to reduce the power threshold required to reach the H-mode operational regime [JOWB98, WOB+92].

Within the frame of this work, conducted at the WEGA stellarator at IPP Greifswald, fundamental experiments concerning biasing have been conducted to demonstrate the option of altering the radial electric field in a plasma by means of an externally biased probe. Due to the low available heating power of 26 kW at maximum in WEGA compared to the H-mode threshold, requiring a minimum of at least 100 kW, WEGA cannot be operated in the H-mode or near the H-mode threshold. Typical plasma parameters are in the order of $n_e \approx 10^{18}\,\mathrm{m^{-3}}$ and $T_e = 4 - 12\,\mathrm{eV}$ for a typical WEGA argon plasma in low magnetic field operation ($B = 56\,\mathrm{mT}$). The plasma is heated by OXB-mode conversion using 2.45 GHz microwave sources.

The shape of the radial electric field profile is known to be important for the magnitude of the turbulent transport[HPD+04, HDH+99, II88, Ram05, VGM+01]. Within the frame of this work the focus is on the impact of biasing on the radial electric field and other plasma parameters. Biasing in the WEGA stellarator is conducted in discharges, in which only little turbulence is found. This is done in order to investigate the effect of the biasing without the considerations on the effects on the turbulence, which might obscure the results.

In contrast to other biasing experiments the argon ions are not confined due to the low magnetic field in WEGA. This combination makes the conduction of biasing experiments in the low field operation of WEGA unique.

Using a large emissive probe for biasing, significantly increases the peak density and causes a steepening of the density gradient at the plasma edge. It is found that this effect is related to the emissive operation of the probe and not an aspect related

to biasing. Using positive biasing, the radial electric field can be increased linearly from the minimum value of $E_r \approx 40 \frac{V}{m}$, observed without biasing, to about the threefold of its original value ($E_{r,\,biased} \approx 120 \frac{V}{m}$). Similar observations have been reported from other biasing experiments as well [WOB$^+$92, VGM$^+$01].

With biasing voltages exceeding $U_{bias} = +60\,V$, a transition to an alternative plasma state is observed. This state shows a significant increase in temperature and density compared to the standard plasma state and is, thus, called high n_e-T_e state. For the first time electron temperatures larger than $T_e = 20\,eV$ have been established in low field argon operation in WEGA. The radial electric field in the high n_e-T_e state is reduced compared to the low n_e-T_e state. This is understandable as the drawn biasing current is reduced as well. Looking at this in more detail reveals the radial electric field in this state being lower than expected from current scaling of the low n_e-T_e state. It turns out that the presence of the limiter in the far SOL has an impact on the performance of the plasma state. Without the limiter installed, the high n_e-T_e state evolves gradually and the obtained radial electric field is higher than in the case of a transition from the low n_e-T_e state as is observed with the limiter installed. A destabilization of the high n_e-T_e state has only occurred at reduced heating power and increased gas pressure.

Compared to the low n_e-T_e state, the confined energy of the high n_e-T_e state is larger by a factor of ≈ 2. Compared to the reference discharge, this is an increase of about $40\,\%$. This is similar to the achievement of devices in which biasing has been used to reduce turbulence and where improved confinement regimes have been obtained. As a further reduction of turbulence can be ruled out (even an increase in the level of turbulence is observed), a different mechanism has to be responsible for this change of the plasma.

The observed high n_e-T_e state shows power degradation similar to the standard discharges. It is, thus, attempted to understand this aspect. Using two basic models, the particle and power balance for WEGA is evaluated. As the microwave power is the single input power source, its power flux has to be balanced by the loss processes. This allows calculating the total absorbed microwave power and to give a statement on the conversion efficiency of the complex heating a quantity otherwise hard to assess. By comparing the different states, it is shown that the observed high n_e-T_e state is related to a change in the heating efficiency, which is increased from $\eta_{mw} \approx 30\,\%$ - for the low n_e-T_e state or unbiased discharges - to values exceeding $\eta_{mw} \geq 80\,\%$. The observed transition can hence be attributed to a change in the microwave heating efficiency.

"Even a mistake may turn out to be the one thing necessary to a worthwhile achievement. "

Henry Ford (30.07.1863 - 07.04.1947)

für Anu, Alexandra und Kevin

Contents

Chapter 1

Introduction

As the discussion about energy prices and global warming becomes more fierce, the quest for a sustainable, yet cheap, energy source becomes more important. Many renewable resources are either lacking the ability for continuously supplying energy or the ability to compensate fast increases in demand. These two features, besides a good cost-value-ratio, are the most important features of present fossil resource-based power plants. Burning fossil fuels leads to emission of carbon dioxide, which is in turn undesired. One candidate to replace fossil-based power plants in the future is a power plant based on thermonuclear fusion. Here, one exploits the relation $E = mc^2$, where the energy of a body E is directly related to its mass m by the speed of light c. This may be used to gain free energy if one is able to increase the binding energy of the nucleons shown in figure 1.1. This can be achieved by either
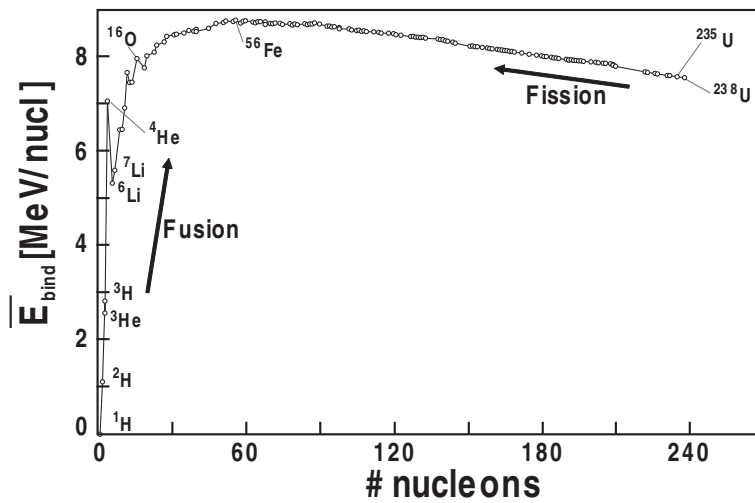

Figure 1.1: Average binding energy per nucleon.

breaking heavy elements (e.g. uranium) up into lighter elements or by fusion of light elements. The D-T reaction is chosen as the most appropriate candidate for use in a fusion power plant. Before a power plant can be built and operated economically efficient, the output fusion power has to be substantially larger than the power required to maintain the burning plasma condition. The so-called fusion product is an indicator for the capability of a plasma reactor. It is defined as the product of particle density (n_i), temperature (T_i) as well as the energy confinement time (τ_E):

$$n_i \left[\mathrm{m}^{-3}\right] \ T_i \left[\mathrm{K}\right] \ \tau_E \left[\mathrm{s}\right] > 6 \cdot 10^{28} \ \left[\mathrm{Ksm}^{-3}\right] \tag{1.1}$$

In order to achieve a stably burning fusion reaction, this value needs to exceed $6 \cdot 10^{28} \, \mathrm{Ksm}^{-3}$. This is also known as the Lawson criterion for fusion [Law55]. One must go to high temperatures as the cross section for fusion reactions strongly depends on the temperature of the involved particles, having a maximum near 100 keV[1]. Different approaches can be made in order to achieve this value. While temperature is more or less fixed, one has the option of either making the plasma as dense as possible taking into account the very short confinement times (inertially confined fusion) or go to long confinement times in the order of seconds at lower density. The later path is chosen for magnetically confined fusion using plasmas.

Here, the fusion particles are confined by a strong magnetic field, insuring a high degree of thermal insulation, with respect to the reaction vessel. The plasma is heated externally to reach the required temperature in the order of several ten million degrees. Linear machines are not capable of providing the required degree of confinement due to the losses occurring at their ends. For achieving a high fusion product, bending the linear device to a torus to avoid losses at the end plates is more useful. A simple torus, on the other hand, is not confining by its nature as will be explained later. Nevertheless, the concept of a toroidal shape has been kept since then as it is possible to create confining toroidal geometries.

One issue addressed in present-day fusion devices is how to extend the energy confinement time to the required value of ~2 seconds. In the past, large progress has been made in meeting this requirement for magnetically confined fusion. Until 1982 fusion devices have been operated in low confinement regime or "L-mode". In 1982 the discovery of the H-mode [WBB+82], an improved confinement regime, in the ASDEX device was a major breakthrough. Here, the energy confinement time could be increased substantially. Until today, many other magnetic fusion devices

---

[1] 1 eV $\hat{=}$ 11605 K

have been able to reach H-mode operation regimes [FIS⁺98, HPD⁺04, IKT⁺97, KTT⁺06a, VAA⁺03]. The H-mode is considered to be the standard operating regime for the first energy producing fusion reactor ITER[2], currently under construction in Cadarache, France. In the mean time a lot of work has been carried out in the attempt to understand the principles of physics of the L-H transition of the plasma [II88, SC89, Ten97]. Nevertheless, a full description of the transition and its underlying mechanisms is still lacking. Despite lacking such theoretical descriptions quite some progress has been made in the last 25 years by gaining experience in achieving the H-mode regime experimentally. Starting from the knowledge of the original H-mode being triggered by applying more heating power than a certain threshold to the plasma, a substantial amount of research has been carried out. It has become clear early on that one way to obtain H-mode plasmas is simply increasing the heating power above the threshold value. Once a critical value, the so-called threshold power, is reached the plasma state changes rapidly and a more favorable regime of operation is obtained. By comparing many different experiments a scaling for the threshold power has been found. The heating power threshold scales with the toroidal magnetic field, the plasma density and the plasma size. The observed scaling for the threshold power has been derived from comparing different fusion experiments to be [RSB⁺98, RTDG02, SIHMTDWG00, RTDWG98, GC98, FTK⁺98]:

$$P_{thres} = 1.42 \cdot n_e^{-0.58} \cdot B_0^{0.82} \cdot a^{0.81} \cdot R \qquad (1.2)$$

with electron density n_e in $10^{21}\,\mathrm{m}^{-3}$, magnetic field B_0 in T, plasma radius a and major radius R in m and threshold power P_{thres} in MW. Special interest has been put to the reduction of the heating power threshold. It has been found that the L-H-transition is closely related to the underlying radial electric field and its radial profile [Ida98].

1.1 Biasing

The finding of the radial electric field [Man94, Str93, UAB⁺91] playing an important role in the L-H-transition, is where the original idea of biasing enters: One places a conducting object into the plasma region and biases this conductor with respect to the vessel or a specific structure. The additional electric field $\vec{E}$ leads to a current

---

[2]ITER stands for **I**nternational **T**hermonuclear **E**xperimental **R**eactor

$\vec{j}$ according to

$$\vec{j} = \sigma \vec{E}, \tag{1.3}$$

with σ being the conductivity in the plasma.

This rather crude approach has been demonstrated to work well in many different experiments [Boi92, GAAT02, HPD$^+$04, IKT$^+$97, KTT$^+$06b] in triggering transitions to H-mode plasmas even without reaching the threshold power. Biasing is often very specialized with respect to the distinct surrounding at the given machine. A broader overview on biasing experiments is given in section 2.5. It has been shown in a number of devices that the transition to H-mode plasma states can be externally triggered using biasing probes [TBF$^+$89, WOB$^+$92] or biasing whole sets of plasma facing components in fusion devices [JOWB98, Str93] - even without reaching the threshold power [KTT$^+$04, WOB$^+$92].

The biggest problem with using biasing probes to optimize the parameters of a fusion plasma is based in the origin of biasing gear. Any biasing probe is an object in contact to or even immersed in the hot fusion plasma. Typical biasing probes consist of the same materials as plasma facing components in order to withstand the harsh environment conditions existing inside a present device. Extrapolating today's results to a reactor would mean further increasing the heat and particle load to the biased structure. The tremendously large heat load and particle flux in a fusion reactor would disintegrate any known material within a very short time, destroying the probe in the process. Also, the eroded material would have quite a severe impact on the plasma as bremsstrahlung and line radiation of probe material ionized in the plasma will lead to additional, undesired, cooling of the hot plasma. Besides this, the material eroded from the probe could form dust storing part of the radioactive tritium used for the fusion reaction. This would be a significant risk. Due to all these consequences biasing with a probe will not be used in a fusion reactor. In a later part of the thesis also the aspect of biasing in a reactor without the use of biasing probes will be addressed. For modifying the radial electric field in hot plasmas also neutral beams or microwaves can be used alternatively [RHB$^+$99]. The academic interest in biasing is still active nonetheless. The main reason here is, that biasing has proven to be an interesting option for altering the plasma parameters, as well as studying the impact of the electric field on turbulence, making new fields of research accessible even in small machines. Also biasing in smaller machines does not put as much requirements to the biasing equipment, as hotter reactors, due to the modest plasma parameters.

The work presented in this thesis will focus on the impact of deploying a biasing probe to the low temperature plasma of the WEGA stellarator and document the results obtained with biasing the WEGA argon plasma in low field operation. The biasing equipment used in WEGA is dimensioned in such fashion, that it is possible to rival the main heating source with the power of the biasing gear.

1.2 Structure of the Thesis

This thesis will be structured in three major parts making up a total of eight chapters aside this introduction.

Chapters 2 to 4 will first present the prerequisites for understanding the content of this thesis. Terms related to magnetic field properties will be explained in chapter 2. In chapter 3 an introduction to basics of spectroscopy will be given. Here, broadening mechanisms to spectral lines will be introduced. A small part on basic optics is covered, as far as it is required to understand this thesis. In chapter 4 the experimental apparatus consisting of the WEGA stellarator and its diagnostics will be introduced. The designs of the biasing probes can be found within this chapter as well.

The second part of this thesis, consisting of chapters 5 to 7 will present the experimental work, as well as the results of the modeling, conducted within the frame of this thesis. In chapter 5 the reference configuration will be presented. This is followed by the characterization of different argon plasmas produced without the introduction of the biasing probe to the vessel. The impact of deploying the unbiased biasing probe to the plasma is documented in this chapter as well. The results obtained with the energized biasing probe will be presented in chapter 6. Following this, a consistency check of the presented data involving two basic models will be made in chapter 7.

The last part of this thesis, which is divided into two chapters, will be used to summarize the experimental results in chapter 8. The results will be discussed with respect to opening alternative operating scenarios including biasing in chapter 9. Also the further development of the model will be discussed in chapter 9, as will be the future of the used diagnostics.

Chapter 2

Magnetic Confinement

In this chapter the aspect of using magnetic fields to realize magnetic confinement of the hot fusion plasma will be briefly introduced. As mentioned in the introduction a linear magnetic device cannot be used for fusion due to losses at the end plates. It seemed logical to bend the field into a toroidal geometry. First, the toroidal geometry will be introduced. Then, features of the confining magnetic field will be highlighted. Finally, the option of biasing plasmas in toroidal geometries will be discussed and conclusions to the WEGA biasing campaign will be drawn.

2.1 Toroidal Coordinate System

It is useful at this point to introduce the toroidal coordinate system since rectangular coordinates will be more the exception within this thesis. The typical coordinate system is called toroidal coordinate system described by (r, φ, θ), the minor radius r, the toroidal angle φ, and the poloidal angel θ. Figure 2.1 shows the toroidal coordinate system.
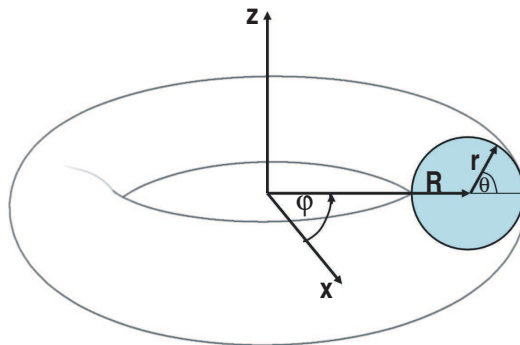

Figure 2.1: The toroidal coordinate system (r, φ, θ).

7

The transformation from the usual rectangular space coordinates (x, y, z) to torus coordinates (r, φ, θ) is given by

$$
\begin{aligned}
x\,(\,r,\,\varphi,\,\theta\,) &= \cos\varphi \cdot (\,R + r \cdot \cos\theta\,) \\
y\,(\,r,\,\varphi,\,\theta\,) &= \sin\varphi \cdot (\,R + r \cdot \cos\theta\,) \\
z\,(\,r,\,\varphi,\,\theta\,) &= r \cdot \sin\theta
\end{aligned}
\tag{2.1}
$$

Some descriptions may be given in a coordinate R instead of r, giving the distance from the center of the torus or the major radius. $R_0\,(r=0)$ is also related to as the major radius of the device. Note that r is the distance from the center of the poloidal cross section of a given major radius R. The minor plasma radius is commonly labeled with a.

2.2   Consequences of the Toroidal Geometry

Toroidal geometry introduces forces on the plasma particles, leading to drift motions, which are described in detail in appendix A. Except for $\vec{E} \times \vec{B}$-drift, the drift motions introduced in appendix A share one common aspect: They are charge dependent heading into opposite directions for electrons and ions. This would lead to charge separation in a pure toroidal magnetic field. A pure toroidal magnetic field B_φ has a radial dependence of $B_\varphi(R) \propto \frac{1}{R}$, hence $\nabla\vec{B}$ is pointing inward. The curvature of the magnetic field amplifies this, as the corresponding force is acting in the same direction as $\nabla\vec{B}$. This leads to the positively charged particles accumulating on the upper side of the torus, while negatively charged particles would accumulate in the lower part of the torus. Charge separation in the torus would produce an electric field. This field in combination with the magnetic field then leads to radial drift motion overlapping with $\nabla\vec{B}$- and curvature drift expelling particles even faster from the confined region.

A radial electric field would lead to a drift motion (as explained in appendix A) in poloidal direction equation A.7 from the appendix can be simplified in toroidal coordinates to

$$
v_{\theta,\,\vec{E} \times \vec{B}} = \frac{E_r}{B_\varphi} + \frac{E_\varphi}{B_r},
\tag{2.2}
$$

as gradients in toroidal direction are relaxed fast due to the high mobility of particles parallel to the magnetic field ($E_\varphi \approx 0$). The second term in equation 2.2 becomes very small compared to the first and can be neglected in a stellarator with pure ECRH heating as WEGA as the heating system does not introduce momentum to

the plasma as heating with neutral beams would cause for example.

2.2.1 Stellarator & Tokamak

A different magnetic geometry is needed in order to avoid the loss of particles due to charge separation in a pure toroidal field. The introduction of an additional poloidal magnetic field component B_θ, superimposed to the toroidal field, allows connecting the regions on the top and the bottom of the torus via a magnetic field line. Charged particles, which can travel parallel to the field line without restrictions, are now able to move parallel to the magnetic field line from the low field side of the device to the high field side and vice versa. Charge separation is suppressed. It is sufficient to have a very small poloidal field component compared to the toroidal field.

Historically, there are two different approaches in how this field is created. The first approach was the "stellarator"[1]using external field coils to create the poloidal (magnetic) field component in addition to the field coils producing the toroidal magnetic field. The stellarator concept was introduced by the American physicist Lyman Spitzer Jr. in 1951 [Spi51]. In 1952 the Russian physicists Sacharow and Tamm introduced the "Tokamak"[2] using the transformer principle to induce a toroidal current in the plasma by a central transformer coil. This can be done due to the fact that a plasma consists of charged particles. The plasma column acts as the secondary winding of the transformer.

The tokamak is limited, by its nature of being a transformer, to pulsed operation or the need for non-inductive current drive to maintain the poloidal field component in steady state. A stellarator on the other hand can work continuously as all field components are produced by external coils. Another major difference between stellarators and tokamaks is that a tokamak is a two- dimensional system showing axissymmetry and a stellarator is a fully 3-dimensional system. This has been a severe limitation for designing stellarators in the past. With the availability of more powerful computers, allowing the calculation of such complex three dimensional magnetic field geometries within reasonable time, large progress has been made in realizing advanced stellarators. The performance advantage of a tokamak has already been made up by the current generation of optimized stellarators and also stellarators do not suffer from severe instabilities limiting the operation space of a tokamak. The result of an international optimization effort for stellarators, Wendelstein 7-X, the

---

[1]stellarator is derived from the Latin words "stella" - star - with an appended "machine"

[2]"Tokamak" is an abbreviation from Russian: toroidal chamber with magnetic field coils; "Tok" is also a Russian word for current

most advanced stellarator, is presently being built at the Max-Planck-Institut für Plasmaphysik in Greifswald, Germany.

Transitions to improved confinement regimes have been observed in tokamaks [RTDWG98, RSB$^+$98, RTDG02, SIHMTDWG00, TBF$^+$89, WBB$^+$82, Wol03] as well as in stellarators [BGK$^+$00, SII$^+$01, Toi96].

2.2.2   Periodicity

In order to classify different classical stellarators, the periodicity is introduced. Periodicity in classical stellarators is categorized in two numbers - the poloidal periodicity l and the toroidal periodicity m. The poloidal periodicity l determines the symmetry of the magnetic surfaces in a poloidal cross section ($\varphi = const.$). It is defined as the number of pairs of helical windings on a classical stellarator. One set of helical windings leads to a circular shape ($l = 1$); two sets lead to an elliptical shape ($l = 2$) and three sets of coils to a triangular shape ($l = 3$).

The number of revolutions the helical coil system does poloidally before closing upon itself is called toroidal periodicity m. Due to this helical symmetry identical flux surfaces in WEGA can be found at toroidal angles $\varphi = \varphi_0 + N \cdot \frac{360^o}{m}$ with $N \epsilon \{ 0, 1, 2, ..., m - 1 \}$.

2.3   Flux Surfaces

The existence of a poloidal magnetic field component allows the definition of flux surfaces. A flux surface Ψ is defined by

$$\nabla \Psi \cdot \vec{B} = 0. \tag{2.3}$$

In a more intuitive picture, a flux surface is created by following a magnetic field line, having a toroidal as well as poloidal component, around the torus. If the field line does not close in itself after a number of toroidal turns, which is then called rational surface or only rational, the field line spans a magnetic flux surface. The radial structure formed by multiple flux surfaces is called a set of nested magnetic flux surfaces, if the flux surfaces are nested within each other. At rational surfaces magnetic islands, in itself sets of nested magnetic flux surfaces, can exist either as feature of the magnetic configuration (natural islands) or as result of errors due to e.g. coil alignment mistakes (non-natural islands).

In a tokamak the existence of flux surfaces can be calculated, but measuring them accurately is a problem, as it is not possible doing so without plasma. In a stellarator the existence of nested magnetic flux surfaces is not guaranteed as equation 2.3 cannot be solved in a closed fashion in three dimensions. The existence of flux surfaces in a stellarator can be shown experimentally with very high accuracy as the confining magnetic field is created by external coils. The well-established electron beam technique [OLW03] has been used to demonstrate the existence of nested magnetic flux surfaces in WEGA. The magnetic field topology can be calculated by different established field line tracing codes such as the GOURDON code [Gou70] or the w7 code [Wer]. Theoretical prediction and experimental results agree well for WEGA for a large parameter range [OLW03].

A typical result of such a calculation with the w7 code for the WEGA conditions is shown in figure 2.2. Every point in the plot marks a field line passing the poloidal plane at the given toroidal angle. This type of plot is called Poincaré plot and will be found often in this thesis showing the magnetic field topology at a given poloidal plane. The Poincaré plots shown in this thesis will not only show the results of the magnetic field calculation, but will also display important machine features, such as e.g. diagnostic ports, diagnostics or their lines of sight.
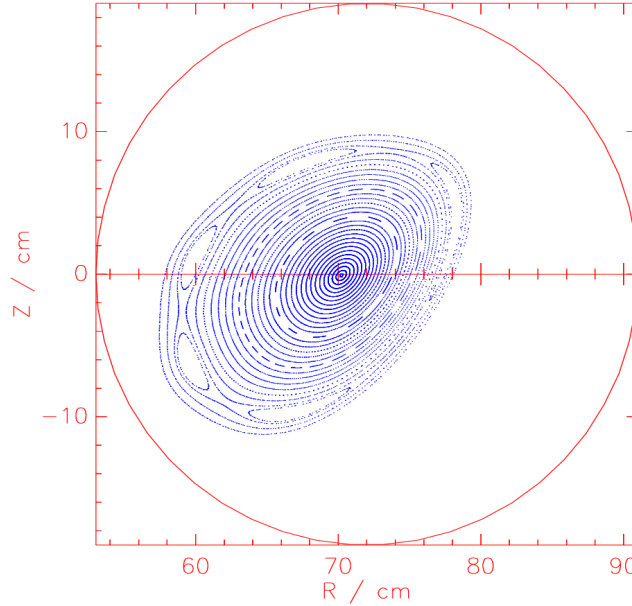

Figure 2.2: Poincaré plot of the flux surfaces for the reference configuration at a toroidal angle of $\varphi = 144\,°$ as given by the w7 code including the vessel contour.

For the configuration presented in this thesis, the beginning of the non-confined area (scrape-off layer - SOL) is determined by the position of the first plasma fac-

ing component, here the microwave heating antennas. Positions of diagnostics or relevant parts can be shown in Poincaré plots as well.

As the description of plasmas in real space coordinates (toroidal coordinates) is often not very meaningful, it is useful to introduce a reasonable description for comparing different real space positions with respect to the given magnetic configuration. A common description trades the minor radius r in for the effective radius r_{eff}. r_{eff} directly relates the complex geometry of a flux surface to the more intuitive description of a circular plasma having the same covered area. The toroidal coordinate system is then changed from $(r, \varphi, \theta) \rightarrow (r_{eff}, \varphi, \theta)$. The scheme is shown in figure 2.3.

In a stellarator a slightly altered convention is chosen due to the fully 3-dimensional structure of the magnetic field.
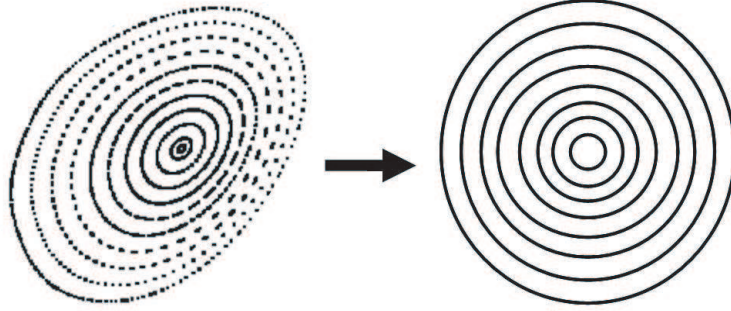
Figure 2.3: Sketch of $r_{reff}-$mapping of a flux surface geometry to circles of equivalent area.

The flux surface geometry of a stellarator can change its poloidal cross section while going around the torus toroidally. It is useful to find a parameter to express similarities. The effective radius for a stellarator is defined by the radius of a circle having the same area as the average of the poloidal cross section areas of the corresponding flux surfaces at the plane of symmetry and half a field period away from the plane of symmetry. For WEGA the plane of symmetry is defined by the toroidal position of the mirror symmetry to $z = 0$ in a poloidal cross section ($\varphi = const.$). This results in the following equation:

$$\pi \cdot r_{eff}^2 = \frac{1}{2} \cdot \pi \cdot \left(\left[\int r' dr' \right]^{\varphi = -18^\circ} + \left[\int r' dr' \right]^{\varphi = 18^\circ} \right). \qquad (2.4)$$

An important consequence of the existence of flux surfaces is the non-necessity for measuring perpendicular to the flux surface in order to derive a quantity per-

pendicular to the flux surface. Due to the high mobility of particles parallel to the field line pressure gradients are compensated by particles streaming along the field line. Flux surfaces are isobars as far as plasma pressure is concerned.

A special magnetic field configuration featuring a separatrix (magnetically defined LCFS) is the divertor configuration. Modern tokamaks can feature a divertor which is commonly produced by installing an additional coil in the bottom of the vessel. A simple comparison between a configuration limited by a plasma facing component (PFC), one being limited by a magnetic separatrix and a divertor configuration are sketched in figure 2.4.

The divertor configuration was found to be effective for controlling the amount of impurities in the plasma. The improvement with divertors is in the remote (with respect to the magnetic field) location of the divertor plates.
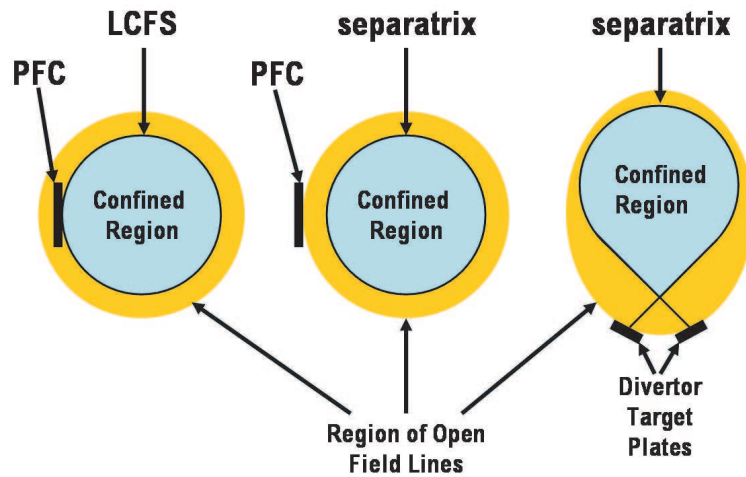

Figure 2.4: Left to right: Limiter, separatrix and divertor configuration.

A buffer plasma zone in front of the divertor plates reduces the heat load to the divertor structure struck by the separatrix. A divertor allows the neutralized impurities to be pumped away effectively, which would not be possible in the main chamber.

2.4 Rotational Transform

The next term to be aware of is rotational transform ι, describing the pitch of the magnetic field line given by the geometry of the toroidal and poloidal field components. It is defined as the derivative of the poloidal magnetic flux χ to the toroidal magnetic flux Φ:

$$t = \frac{d\chi}{d\Phi} \tag{2.5}$$

with the poloidal flux χ defined by

$$\chi = \frac{1}{2\pi} \int \left(\vec{B} \cdot \nabla\varphi \right) d^3r \tag{2.6}$$

and the toroidal flux Φ given by

$$\Phi = \frac{1}{2\pi} \int \left(\vec{B} \cdot \nabla\theta \right) d^3r. \tag{2.7}$$

The definition can be visualized by turning to the simple picture of following a field line around the torus. Looking at a $\varphi = const.$- plane, one can identify each pass of a field line. t is then given by the average angle in radians between passes of a field line per toroidal turn,

$$t = \frac{1}{2\pi} \lim_{n \to \inf} \left(\frac{\iota_n}{n} \right), \tag{2.8}$$

with ι_n being the angle between the starting point and the nth pass through the $\varphi = const.$- plane with respect to $r = 0$. The existence of a finite rotational transform connects the outward side of the plasma to the inward side of the torus as a magnetic field line now runs from the outside to the inside of the torus and vice versa. This is essentially a short circuiting of the outside of the tours and the inner side - respectively the upper and lower edge of the plasma - thus compensating the charge separation caused by curvature and $\nabla\vec{B}$-drift.

2.5   Biasing Plasmas

As is mentioned in the introduction, the idea of biasing plasmas in toroidal geometries has been around for more than 30 years now, starting with the proposal by Kerst in 1975 [Ker75]. Using biased electrodes in the plasma or in the plasma edge, it was shown that the radial electric field can be externally induced and controlled [Boi92, Str93, WOB+92]. With fusion devices being equipped with divertors, also these have been used for biasing, as has been reviewed in [Man94, Sta95a]. Recently, very sophisticated designs have been employed. Ramisch has recently demonstrated the use of biasing electrodes matching the topology of the magnetic field [Ram05] and also advanced materials, like LaB_6, have been employed as has been reported in [IKT+97, KTT+04, SFN+06].

Using biasing to achieve H-mode plasmas in a device, it was often sufficient to bias the plasma with little power compared to the main plasma heating source. In the CASTOR tokamak currents in the order of 40 A have been drawn to the limiter while the biasing probe was energized to 200 V [VAA$^+$03]. On the other hand significant biasing power ($\approx 360\,\mathrm{kW}$) has been required using a biasing probe in the TEXTOR-94 experiment, where up to 600 V at 600 A have been used [VAA$^+$03]. In stellarators biasing requires less power to achieve H-mode conditions as has been reported from machines, like the TU-Heliac. Biasing powers in the kW range have been sufficient to trigger transitions to the H-mode [KTT$^+$04, KTT$^+$06a].

It has been found that the L-H- transition is closely related to the degree of turbulence. The level of turbulence in H-mode plasmas is reduced compared to the standard L-mode plasma [KTT$^+$06a, VAA$^+$03, SII$^+$01]. In a simple picture the potential induced by biasing adds an additional sheared electric field modifying the statistical properties of turbulent structures [JOWB98, VSG$^+$01].

Aside from these reported transitions to H-modes, also transitions to plasma states not quite fitting the common understanding of an H- mode have been observed. Such transitions have for instance been found in the Australian H-1 NF heliac in the mid 1990ies [SRB$^+$96]. Usually, those non-H-mode transitions have not been pursued further as it became obvious that they are not transitions to H-mode conditions, but are often related to complex plasma heating schemes.

Also theoretical effort has been spent into modeling the L-H transition. Biasing has been used to check the models for evoking H-modes in a very reproducible way in machines without having to meet the H-mode power threshold. Here, different approaches to the transition problem have been considered. Shiang et al. related the transition to the underlying radial electric field [II88, SC89], where Hinton explains a transition to improved confinement by temperature increases [Hin91]. In all approaches to the problem the ions are confined by the magnetic field. In anticipation on chapter 4.1.1 stating that a large fraction of argon ions in WEGA are not confined by the low magnetic field, the ions have to be treated as not magnetized, whereas the electrons are well confined by the magnetic field. This feature renders all approaches taken in H-mode modeling useless as all relate to magnetically confined ions.

The chosen path for conducting biasing experiments in WEGA is laid out more basic than the attempt to produce an H-mode plasma in WEGA. Instead, this thesis will join with WEGA's tradition of basic plasma research and will focus on the systematic approach to the problem. It will first demonstrate the capability of

the diagnostics to accurately measure the radial electric field as well as the general plasma parameters of a specific discharge. Then, the impact of the biasing probes on the discharge conditions will be documented. This includes determining if the presence of the biasing probe changes the plasma conditions met in WEGA. Then, the current path inside the vessel will be traced. One experimental goal set is to demonstrate the ability to control the radial electric field. Finally, it will be attempted to produce transitions to operating regimes with improved performance, e.g. higher density, temperature or even improved confinement.

Chapter 3

Basics of Spectroscopy

After introducing basics of magnetic confinement in a stellarator and a basic working plan in the last chapter, a brief introduction to the basics of spectroscopy, one of the employed diagnostic techniques, will be given in the following chapter. Line broadening mechanisms due to motion, as well as atomic processes, will be reviewed. Both are crucial for the correct interpretation of results obtained from spectroscopic measurements. A short introduction into basic optics will be given as measuring in the visible part of the spectrum implies building a proper image.

3.1 Line Broadening Mechanisms

For several spectroscopic techniques the shape of the spectral line is of interest. There are several mechanisms leading to broadening of spectral lines. These mechanisms will now be shortly presented. Their influence on the line shape will be discussed.

3.1.1 Natural Line Broadening

Natural line broadening of spectral lines exists due to the finite lifetime of exited states. In the quantum mechanical treatment of radiation processes the number of atoms in a distinct state is

$$N = N_0 \cdot e^{-\frac{\Gamma}{2}t}. \tag{3.1}$$

In the above formula, $\frac{\Gamma}{2}$ resembles the inverse half lifetime of an exited state. The amplitude $A(t)$ of the emitted line radiation starting at $t = 0$ decays exponentially according to

$$A(t) \propto e^{i\omega_0 t} \cdot e^{-\frac{\Gamma t}{2}}, \tag{3.2}$$

17

where $\omega_0 = \frac{(E_i - E_f)}{\hbar}$ is the frequency of the transition. E_i and E_f are the binding energies of the initial and final states. The Fourier- transformed of the above equation is proportional to

$$A(\omega) \propto \int_{-\infty}^{\infty} \exp[\left(-\tfrac{\Gamma}{2} + i(\omega_0 - \omega)\right) t] dt,$$
$$A(\omega) \propto \sqrt{\Gamma} \cdot \frac{1}{i(\omega_0 - \omega) - \frac{\Gamma}{2}}. \tag{3.3}$$

The spectral intensity distribution $I(\omega)$ is proportional to the square of the amplitude of the emitted light:

$$I(\omega) \propto |A(\omega)|^2. \tag{3.4}$$

The line profile is of Lorentzian shape. It is described by

$$I(\omega) \propto \frac{\Gamma}{(\omega - \omega_0)^2 + (\frac{\Gamma}{2})^2}. \tag{3.5}$$

The natural line broadening for lines in the visible part of the spectrum is of the order of 10^{-5} nm. Under most circumstances this is negligible compared to other forms of broadening. Light sources having a bandwidth in the order of the natural line width are considered to be of single frequency.

3.1.2 Doppler Broadening

Doppler broadening in plasmas is produced by thermal motion of the particles. The Doppler effect describes the shift in resonance frequency of a moving source or moving detector. Light emitted by a moving particle is observed by a stationary detector as

$$\omega = \omega_0 \cdot (1 \pm \frac{v}{c}), \tag{3.6}$$

with ω_0 being the original angular frequency of the emitted light wave and v the velocity component of the particle moving along the line of sight of the detector. In thermodynamic equilibrium particle velocities are distributed according to Maxwell-Boltzmann- statistics:

$$n(v) dv = N \cdot \left(\frac{m_0}{2\pi k_B T}\right)^{1/2} \cdot \exp\left[\frac{m_0 v^2}{2 k_B T}\right] dv, \tag{3.7}$$

resulting in a line intensity distribution of the following shape

$$I(\omega) = const \cdot \exp\left[\frac{m_0 c^2 (\omega - \omega_0)^2}{2 k_B T \omega_0^2}\right]. \tag{3.8}$$

This describes a Gaussian curve centered at a frequency ω_0 having a full width at half maximum (FWHM) $\Delta\omega_D$ of

$$\Delta\omega_D = \frac{2\sqrt{2 \cdot ln2}}{c} \cdot \omega_0 \cdot \left(\frac{k_B T}{m_0}\right)^{1/2}. \tag{3.9}$$

The FWHM is inversely proportional to the square root of the atomic mass of the emitter. Expressing the above as a function of wavelength and temperature gives:

$$\Delta\lambda_D = 7.716 \cdot 10^{-5} \cdot \lambda_0 \cdot \left(\frac{T\,[\mathrm{eV}]}{A_{rel}}\right)^{\frac{1}{2}} \tag{3.10}$$

or

$$T[eV] = 1.68 \cdot 10^8 \cdot A_{rel} \cdot \left(\frac{\Delta\lambda_D}{\lambda}\right)^2. \tag{3.11}$$

In high temperature low density plasmas, Doppler broadening is usually the most dominant line broadening effect.

3.1.3 Zeeman Splitting

Zeeman splitting describes the splitting of atomic or ionic states under the influence of external magnetic fields of not too high amplitude. The splitting of the states is directly proportional to the strength of the magnetic field.

3.1.3.1 Normal Zeeman Effect

The normal Zeeman effect describes the splitting of singlet states. Here, the total spin is equal to zero and the quantum number of total angular momentum j is equal to the quantum number of orbital angular momentum l. From quantum mechanics it is known that the interaction of an atom with a surrounding homogeneous magnetic field, given by its flux density $\vec{B}$, leads to a splitting of the electron energy levels of the atom according to

$$\Delta E = -\vec{\mu} \cdot \vec{B} = -\mu_z \cdot B = m_l \cdot \mu_B \cdot B = m_l \cdot \frac{e\hbar}{2m_e} B. \tag{3.12}$$

Every level splits into $2l + 1$ level, as there are exactly $2l + 1$ eigenvalues m_l to a level having a quantum number of angular momentum l.

3.1.3.2 Anomalous Zeeman Effect

The more common anomalous Zeeman effect occurs when transitions with initial or
final states having a total spin not equal to zero are exposed to magnetic fields. The
calculation of the splitting of the level energies is much more complicated in this
case. The quantum number of the total angular momentum has now values that are
in general not a natural number, but are rational numbers, e.g. $\frac{3}{2}$, due to a non-zero
total spin. As a result of the uncertainty in two of the three directional components
of spin $(\vec{S})$, the magnetic momentum $\vec{\mu}$ is not parallel to the vector of total angular
momentum $\vec{L}$. The magnetic moment $\vec{\mu}$ is defined as

$$\overrightarrow{\mu} = -\frac{\mu_B}{\hbar}\left(\overrightarrow{L} + \overrightarrow{S}\right). \tag{3.13}$$

The shift of the level energies in the case of non-zero spin is

$$\Delta E = -\overrightarrow{\mu} \cdot \overrightarrow{B} = \frac{\mu_B}{\hbar}\left(\overrightarrow{L} + \overrightarrow{S}\right) \cdot \overrightarrow{B} = m_j \cdot g_L \cdot \mu_B \cdot B \tag{3.14}$$

with $g_L = 1 + \frac{j(j+1)+s(s+1)-l(l-1)}{\hbar j(j+1)}$.

Due to the weak magnetic field used in the experiments on WEGA, the splitting
of energy levels is not noticeable. Zeeman splitting of the energy levels and its
impact on the spectral line profile is neglected.

3.1.4 Instrument Broadening

Instrument broadening occurs as imaging of an instrument cannot be perfect. Espe-
cially, when very high precision is necessary, this correction is required. In general
the instrument function has to be monitored in all setups. The instrument function
of a spectrometer is created on one hand by the interference pattern created by the
individual rays interfering and on the other hand by the image of the homogeneously
lit slit on the detector. A slight tilting of the entrance slit leads to a tilting of the
whole image. The instrument function has to be determined for every working point
as the instrument function can vary with wavelength. Measuring with an optical
instrument always delivers the convolution of the real spectrum (F) with the in-
strument function (I). This can be compared to the transfer function of an electric
circuit and similarly expressed as

$$S = F \otimes I, \tag{3.15}$$

where $\otimes$ refers to the convolution operator. In Fourier space convolution becomes a simple multiplication of the Fourier-transformed $F(\omega)$ & $I(\omega)$ of the real spectrum and the instrument function,

$$S(\omega) = F(\omega) \cdot I(\omega). \tag{3.16}$$

In real space this is resembled by the convolution integral,

$$s(t) = \int_{-\infty}^{\infty} f(t_0) \cdot i(t - t_0) dt_0. \tag{3.17}$$

The instrument broadening for the employed spectrometer can be approximated with a Gaussian. More to the details of the employed system can be found in chapter 4.3.

3.1.5 Combination of Different Profile Types

As measured line profiles are subject to many different types of broadening mechanisms, also different broadening processes can occur at the same time. Natural line broadening, for instance, leads to Lorentzian-shaped profiles. Their Fourier-transformed spectrum can be written as

$$L(\omega - \omega_0, \Gamma) = \frac{\Gamma}{2\pi} \cdot \frac{1}{(\omega - \omega_0)^2 + \left(\frac{\Gamma}{2}\right)^2}, \tag{3.18}$$

while the Doppler effect causes a Gaussian-shaped profile:

$$G(\omega - \omega_0, \sigma) = \frac{1}{\sqrt{2\pi} \cdot \sigma} \cdot \exp\left[-\frac{1}{2}\left(\frac{\omega - \omega_0}{\sigma}\right)^2\right]. \tag{3.19}$$

Convolution of both functions produces a Voigt profile, which can occur when both broadening mechanisms are comparable,

$$V(\omega - \omega_0, \Gamma/\sigma) = L \otimes G = L(\omega - \omega_0, \Gamma) \cdot G(\omega - \omega_0, \sigma). \tag{3.20}$$

The convolution of two profiles of identical type can be expressed by

$$\begin{aligned} L_3 = L_1 \otimes L_2 &\Rightarrow \quad \Gamma_3 = \Gamma_1 + \Gamma_2 \\ G_3 = G_1 \otimes G_2 &\Rightarrow \quad \sigma_3^2 = \sigma_1^2 + \sigma_2^2 \end{aligned}. \tag{3.21}$$
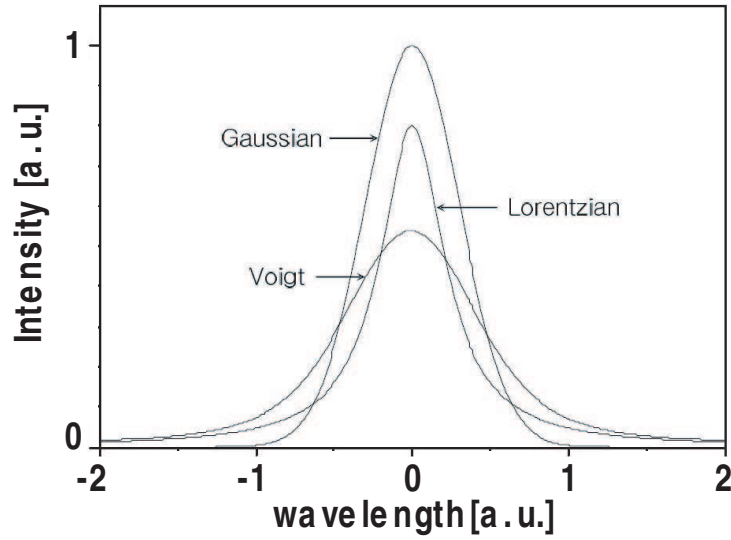
Figure 3.1: Comparison of a Gaussian, a Lorentzian and a Voigt profile.

Figure 3.1 shows a comparison of the three types of profiles. The two important broadening mechanism for spectra presented in this thesis are Doppler broadening and instrument broadening.

3.2   Basic Optics

The following section gives a brief introduction into optics, a bit beyond standard geometric optics. It will not start with the lens maker's equation or its thin lens approximation, but will build up on the general aspects, such as the definition of focal plane and other common terms. More on general geometrical optics can be found in [BSN93, Der16, FBS86]. This section will focus on important aspects related to the design of optics in a more theoretical approach. It will deal with the aspect on how to build a "sharp" image and give a description of common optical flaws and how they can be dealt with.

3.2.1   Sharpness & Depth of Field

In first order approximation a point object can be focused perfectly to a point image only in a single plain. If the point gets slightly out of focus, the point object will be imaged as a spot. A criterion for an acceptable sharpness is given by the size limit of a so-called circle of confusion, commonly labeled with c. Figure 3.2 shows a sketch on how the circle of confusion is created. The size limit for the circle of confusion is, in the case of using a CCD, determined by the pixel size.
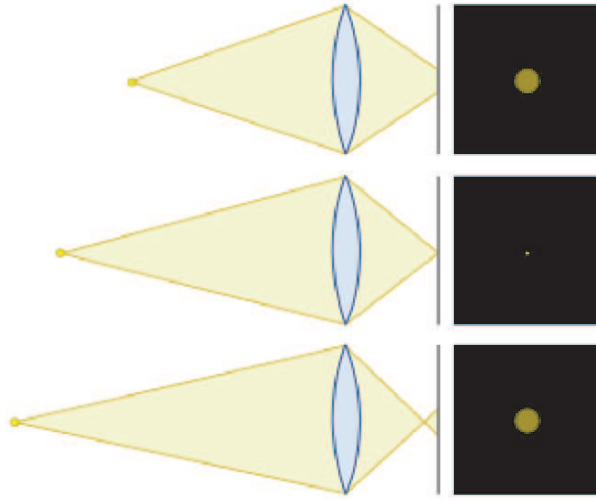
Figure 3.2: Sketch of the circle of confusion for point object at distance shorter than the single focal length (top), single focal length (middle) and beyond single focal length (bottom) of a symmetrical lens.

An image with circle of confusion smaller than or equal to the limit c is considered to be "in focus". The area in which objects can be placed in order to be imaged sharply is called the depth of field (DOF).
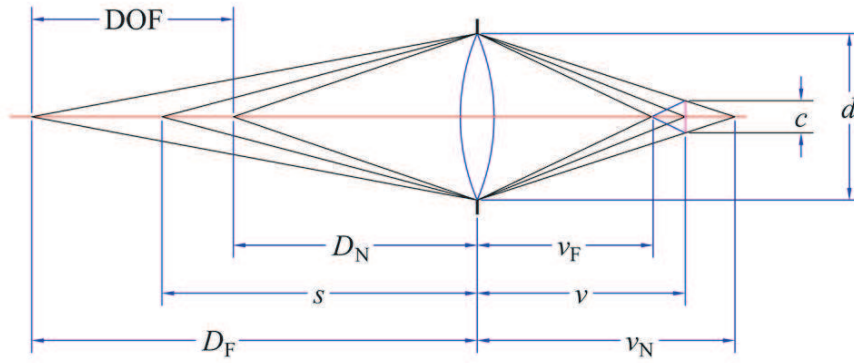

Figure 3.3: Sketch for the calculation of the depth of field for a symmetrical biconvex lens.

The near and far limits of the DOF can be calculated from the similar triangles shown in figure 3.3

$$\frac{v_n - v}{v_n} = \frac{c}{d} \qquad \frac{v - v_f}{v_f} = \frac{c}{d} \tag{3.22}$$

with variables according to figure 3.22. Now using the thin lens equation

$$\frac{1}{s} + \frac{1}{v} = \frac{1}{f}, \tag{3.23}$$

this leads to the limits of the DOF to be

$$D_n = \frac{sf}{f + \frac{c}{d}(s-f)} \quad \text{and} \quad D_f = \frac{sf}{f - \frac{c}{d}(s-f)} \ . \tag{3.24}$$

One special case for the limit of the DOF is the so-called hyperfocal distance H. Here, the far point of the DOF is at infinity ($D_f \to \infty$). The hyperfocal distance can be calculated by setting the denominator equal to 0. This leads to the hyperfocal distance,

$$H = \frac{f \cdot d}{c} + f. \tag{3.25}$$

A more practical equation including the f number $N = \frac{f}{d}$ of the used lens reads as

$$H = \frac{f^2}{Nc} + f. \tag{3.26}$$

In most cases the second term can be neglected as it is small compared to the first. The near point of the DOF can be calculated by inserting equation 3.25 into the first equation of 3.24 to be

$$D_n(s = H) = \frac{H}{2}. \tag{3.27}$$

The image is in-focus ("sharp") between $\frac{H}{2}$ and ∞. For typical single objectives the
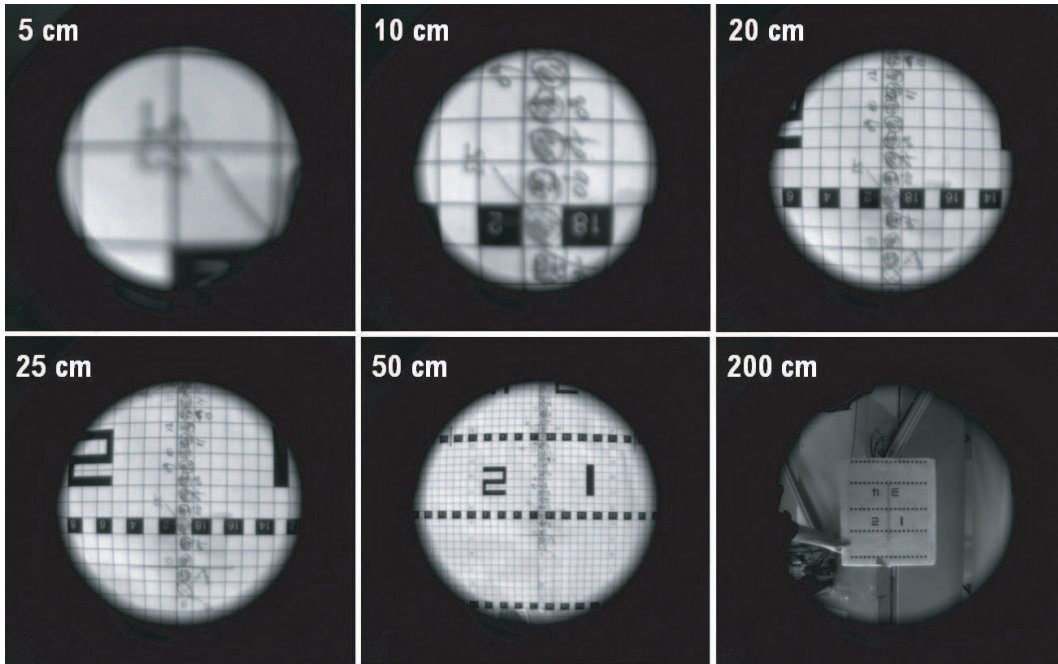

Figure 3.4: Images captured with an infinite depth of field optical system (H = 44 cm) at different distances to the front of the first lens.

hyperfocal point is in the order of 100 m or more from the lens. However, it is also possible to build systems with a very short hyperfocal distance. An optics layout with a hyperfocal distance in the order of tens of cm is also referred to as "infinite DOF system".

The optical system of the coherence imaging spectrometer installed on WEGA shows such properties, with a hyperfocal length in ranging between 5 and 22 cm depending on the exact camera settings. The data recorded with such a system is a true line-integral over the line of sight. This is mentioned here as the spectroscopic system used within this thesis shares the first lens, a reversed PENTAX objective (C25011KP), with the optics of an infinite DOF system. Images obtained with an infinite DOF system are displayed in figure 3.4.

After clarifying when an image is sharp, the properties of the image can now be dealt with.

3.2.2 Image Distortion

Image distortion is a term used to describe the deviation of a rectilinear projection versus the original object. This type of distortion is typically radially symmetric owing to the radial symmetry of lenses. Image distortion can be split into barrel and cushion distortion. Barrel distortion is due to the magnification of the lens decreasing radially outwards from the center of the lens. Cushion distortion, on the other hand, is due to an increase of the lens's magnification radially outward from the center.

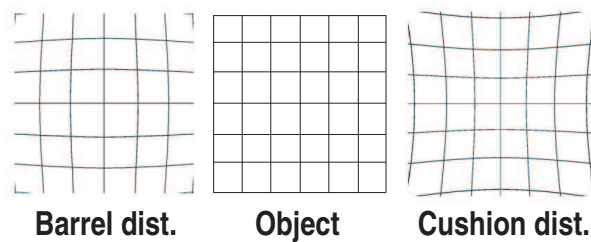**Barrel dist.**　　**Object**　　**Cushion dist.**

Figure 3.5: Barrel (left) and cushion (right) distortion of a rectilinear projection (center).

Barrel distortion, often also called "fish-eye-effect", is used in some optical systems to capture a hemispherical view. Distortion is common to most basic lenses as they are not specially corrected for. Figure 3.6 shows a rectilinear projection seen via a standard non-corrected as well as an especially corrected lens.
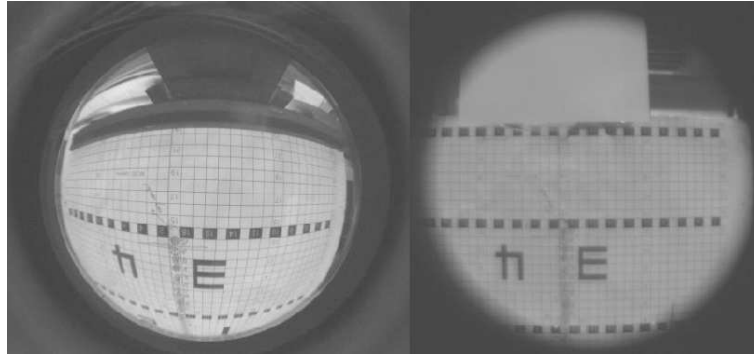
Figure 3.6: Rectilinear projection via a single f=50mm standard lens - barrel distorted (left) ; rectilinear projection via a corrected f=50mm PENTAX/Cosmicar f/1.4 photo objective type C25011KP (right).

Besides barrel and cushion distortion, a mixture of cushion and barrel distortion can occur. This is referred to as mustache distortion. In this case the more central part of the image is barrel distorted and the outer region is cushion distorted. This effect can be created using special retro-focus lenses or large range zoom or macro objectives. In a more practical approach, one can also observe mustache distortion when looking through a wine glass. The surface of objectives showing mustache distortion is typically not a simple curved surface.

Today, software solutions exist for a large number of lenses and objectives for remapping such simple distorted images. Many common picture editing programs already include filters to revert simple barrel or cushion distortion to a better or worse degree, also depending on the underlying lens database. A further disadvantage of a software corrected image is that it does not contain the original data, but is largely interpolated. In this thesis a corrected lens has been available, so that numerical corrections of the image are not necessary.

3.2.3 Spherical & Coma Aberration

When dealing with optical systems, covering geometric optics and distortions is often not sufficient. One has to take care of aberrations as these are inherent to any but especially corrected lens systems. Especially, when dealing with spectrometers in combination with lenses, it is required to ensure the quality of the imaging system.

While a perfect lens focuses all incoming parallel rays to a single point regardless of their elevation to the optical axis, a real lens with a spherical surface will show spherical aberration. The lens will focus rays to a shorter distance, the further away from the optical axis they enter the lens. It does not produce an ideal focal point.

The image will nevertheless be sharp, but will show a decreased contrast. Spherical aberration can be corrected for to some degree by using a combination of convex and concave spherical lenses. Spherical aberration can be fully avoided using aspherical lenses as typically used in standard photo objectives. Figure 3.7(a) shows spherical aberration schematically.
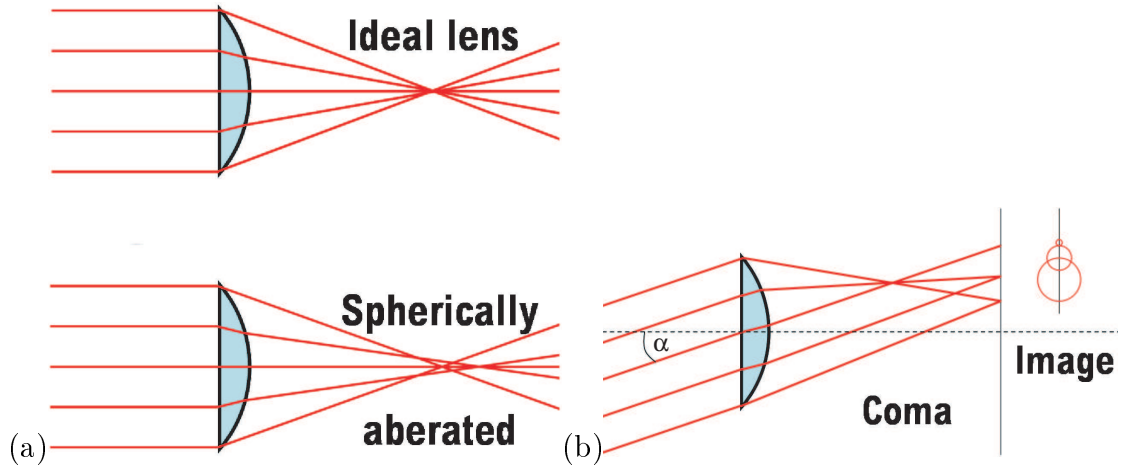

Figure 3.7: Spherical aberration of an lens (a); coma aberration with a convex lens (b).

Another type of aberration to occur in an optical system is comatic aberration. It originates of asymmetry. Light striking the lens under an angle α to the optical axis is focused off the optical axis. This leads to the formation of a cometary coma. The effect is worse the larger the angle to the optical axis. Comatic aberration can be minimized using lens surfaces with a proper curvature to match the application. Comatic aberration can also be caused by simple misalignment (tilting) of a given lens or objective with respect to its ideal position. This can most easily be corrected by appropriate positioning. Figure 3.7(b) sketches comatic aberration of a convex lens. For the WEGA imaging system both types of aberrations are avoided by choice of lenses and proper positioning.

3.2.4 Overlapping & Binning

Since the input to the spectrometer is done using fibers forming the entrance slit with each fiber having its own acceptance angle, one has to ensure that neighboring input fibers do not overlap on the detector. In order to test this, every input fiber has individually been exposed to a defined light source. The resulting images then have been evaluated in order to find pixel lines that are exposed to light from two

input fibers. The hardware-binning of the camera has been chosen in such fashion that those pixel lines are not used for measurements. In figure 3.8 the pixel rows illuminated by a single input fiber, when exposed to light, are marked red and blue. Overlapping of the illuminated areas can occur and the area with overlapping fields of illumination by two adjacent fibers is marked purple. Such overlapping areas are not taken into account.
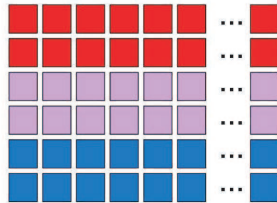

Figure 3.8: Simultaneous use of pixel rows by two adjacent input fibers (schematic).

To avoid smearing of the image, the pixel line next to the overlapping area is not used for binning. In the case of the UHRS at WEGA this overlapping of the channels' images reduces the effective area of the chip in use to about half of its original size. Binning several pixel lines together also allows a faster readout of the camera. Typically 3-14 pixel lines are binned together, giving a total of 29 channels covering the viewing area.

Chapter 4

Experimental Apparatus

In this chapter the WEGA device as well as its portfolio of available diagnostics will be described. The description of the ECR-heating scenario of the WEGA plasma will be given in this chapter after a general introduction to the machine. Also an introduction to the biasing probe setup will be given in this chapter.

4.1 The WEGA Device

WEGA[1] is a medium-sized toroidal magnetic confinement device. It was originally built as a hybrid tokamak and stellarator experiment as part of a French and German cooperation in Grenoble, France, in the 1970s. It was already named WEGA back then with WEGA standing for **W**endelstein **E**xperiment in **G**renoble for the **A**pplication of radio frequency heating. It was operated mainly as a tokamak in Grenoble. In the 1980s WEGA was moved to Stuttgart, Germany, where it had been operated mainly for magnetic flux surface mapping. Finally, the Greifswald branch of the Max-Planck-Institut für Plasmaphysik took over the machine in 2000 and modernized it completely. First experiments were carried out in 2001. Presently, more than 28,000 discharges have been performed. The WEGA vessel has a major vessel radius of $R = 0.72\,\mathrm{m}$ and a minor vessel radius of $r = 0.19\,\mathrm{m}$. Forty planar toroidal field coils create toroidal magnetic fields of $B_{mod} = \left| \overrightarrow{B} \right| = 50 - 500\,\mathrm{mT}$. Two sets of helical windings ($l = 2$), with a toroidal mode number $m = 5$, are used to produce the poloidal field component. WEGA has identical quasi-elliptically shaped poloidal cross sections every 72° toroidally, e.g. $\varphi = 0, 72, 144, 216, 288\,°$. Additionally, a set of vertical field coils in a Helmholtz setup provide a vertical field component to shift the plasma radially. A schematic of the WEGA coil systems

---

[1] **WEGA** is an abbreviation for "**W**endelstein **E**xperiment in **G**reifswald zur **A**usbildung"

is shown in figure 4.1. The toroidal field coils are marked blue. The helical wind-
ings are colored red and green in order to show the different polarity. The sets of
Helmholtz vertical field coils are colored gray. Additionally, the ports of the WEGA
(different colors) as well as the 0-degree axis in the horizontal plane (green line) are
shown. This setup allows a wide range of parameters to be covered.

Two different microwave heating systems are available to produce plasma inside
the vessel. One system operating at $f_{MW} = 2.45\,\text{GHz}$ and one at $f_{MW} = 28\,\text{GHz}$,
delivering up to 26 kW and 10 kW of heating power to the vessel, respectively. Both
systems can work in cw mode. Within the frame of this thesis only the 2.45 GHz
sources have been used. The so-called OXB-mode conversion process is used for
heating the plasma [PLW$^+$07]. As the heating mechanism is quite complex, it will
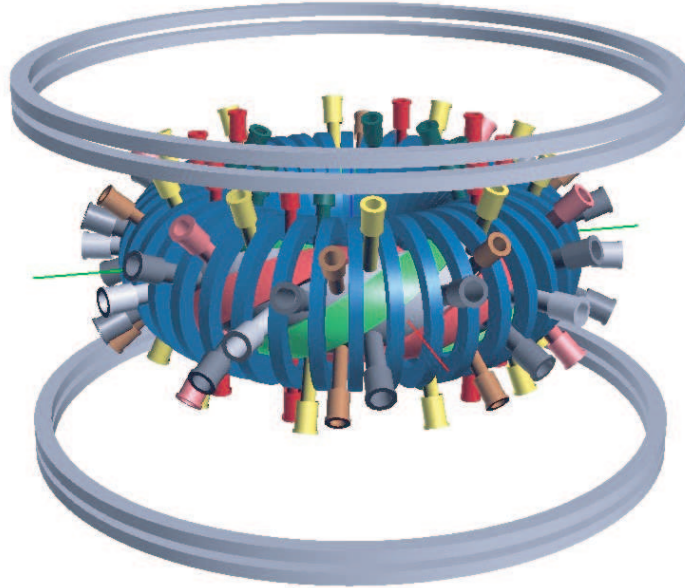be explained in more detail in chapter 4.1.2.

Figure 4.1: Schematic of the WEGA stellarator.

The typical peak plasma density of an ECR-heated argon plasma is around
$n_e = 10^{17} - 10^{18}\,\text{m}^{-3}$ with ion temperatures in the eV range[2] and up to 15 eV
for thermal electrons depending on the input microwave power. A small fraction
of super-thermal electrons has been observed close to the heating mode conversion
zone with temperatures of a few hundred eV [Hor04].

WEGA can be operated with different working gases. Usual working gases are
argon and helium, less common is operation using neon or hydrogen.

---

[2]1 eV corresponds to a temperature of 11605 K

4.1.1 Properties of the Magnetic Field

This passage will summarize the more general features of WEGA's magnetic field in low field operation at $B_{mod} = 0.65 \cdot B_{res} = 56\,\text{mT}$. It will discuss to what degree the plasma particles are indeed confined by the magnetic field in WEGA. The base of assessment is the w7 code [Wer]. The configuration has $t = 0.186$. The figures shown in this part show the trajectories of single particles traveling in the WEGA magnetic field. The magnetic field geometry is indicated by the concentric circles.
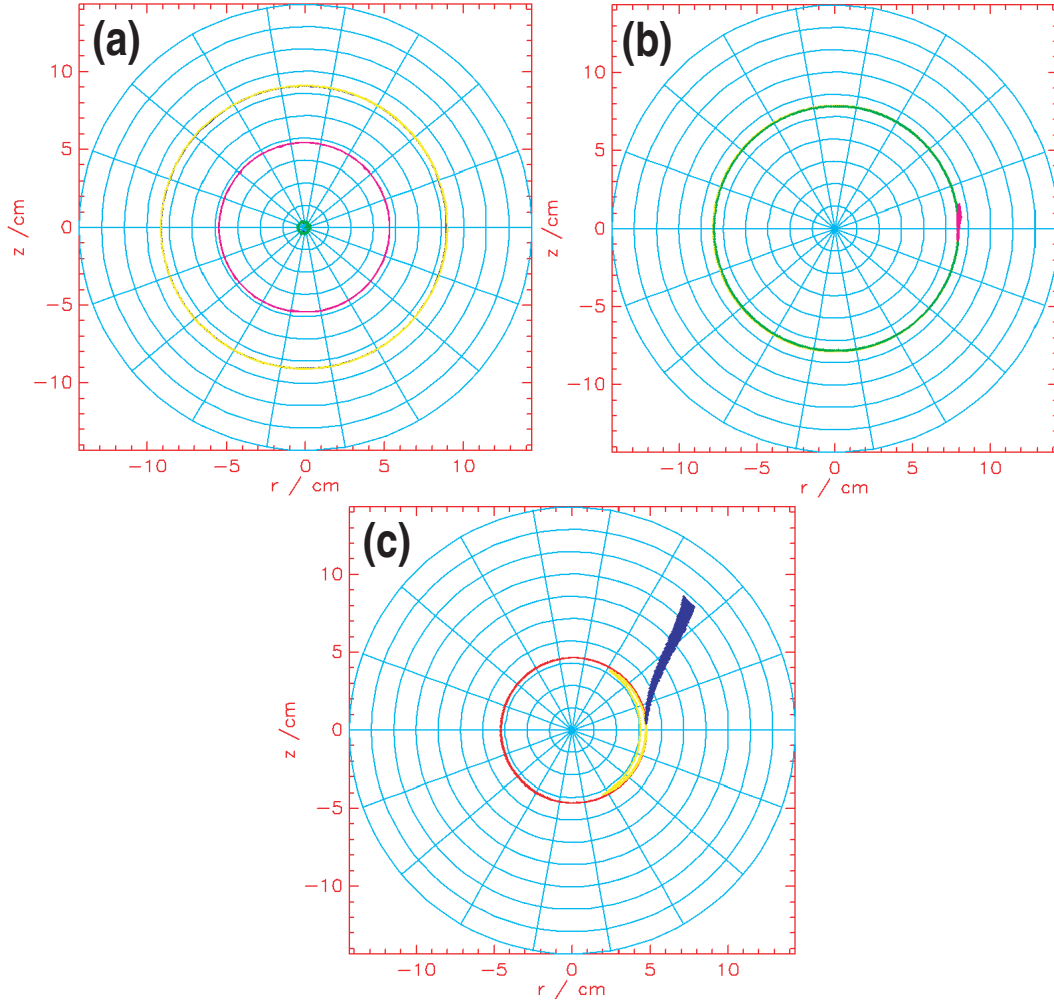
Figure 4.2: Electron orbits for 5 eV electron with varying starting position (blue-R=70 cm, pink-R=75 cm and yellow-R=77.5 cm) (a) ; with varying pitch angle (yellow-30°, green-60°, magenta-90°) (b) ; with varied pitch angle (red-60° = passing particle, yellow-75° = banana particle, blue-90° = particle drifting due to ∇B) (c) .

Figure 4.2 shows the confinement of 5 eV electrons with varying starting position and pitch angle with respect to the magnetic field vector. The transition between an electron following the magnetic field line around the torus, a trapped particle and

an electron with sufficient perpendicular motion, drifting only outward, is shown in
figure 4.2 (c).

As can be seen, electrons are well confined as long as their pitch angle to the
magnetic field vector is not too large. WEGA can be operated with different gases
spanning a large range of masses from 1 amu (hydrogen) to 40 amu (argon)[3]. The
ion Larmor radius for singly charged argon ions under the given situation is in the
order of $r_{L,\mathrm{Ar}^+} \approx 2.3\,\mathrm{cm}$. The trajectories shown are not the trajectories of the
guiding center, but the true trajectory of the ions. The ion orbits of different masses
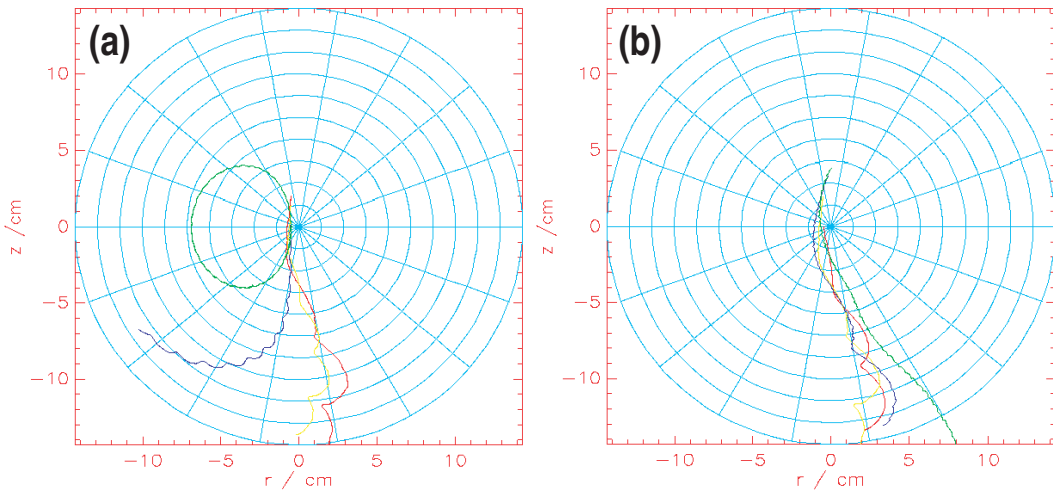for a given starting point are shown in figure 4.3(a).

Figure 4.3: 5 eV Ar$^+$ orbits for (a) different masses (green-H, blue-He, yellow-Ne,
red-Ar) ; (b) different pitch angles for argon (red-0°, yellow-30°, blue-60°, green-90°).

As can be seen hydrogen ions are barely confined to the magnetic field, whereas all
other ions are lost for the magnetic field configuration under consideration. Figure
4.3(b) shows the motion of argon ions for different pitch angles against the magnetic
field. As one can see the pitch angle has an impact on how long the particles remain
inside the magnetically confined region. The general feature of the particles being
lost remains for all pitch angles. The same property is also valid if the starting point
of the particle is varied as is shown in figure 4.4(a).

Changing the particle energy does not lead to significant changes as can be seen
for a varied ion temperature in figure 4.4(b). Also adding a radial electric field does
not change this behavior as is shown in figure 4.5. The radial electric field in figure
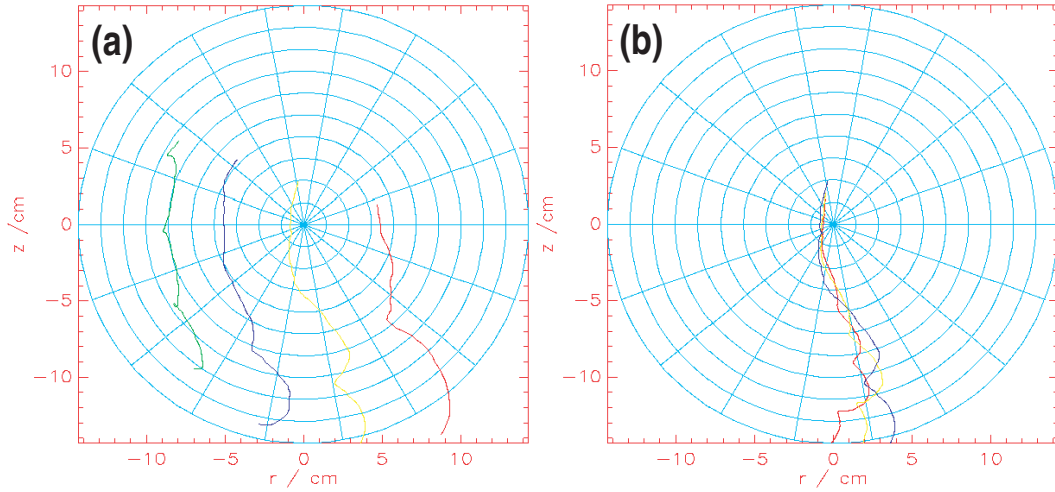
---

[3]1 amu $= 1.66053886 \cdot 10^{-27}\,\mathrm{kg}$

Figure 4.4: Ar$^+$ orbits for (a) different starting positions (green-R=60 cm, blue-R=65 cm, yellow-R=70 cm, red-R=75 cm; E=5 eV, pitch=30°); (b) different particle energies (red-3 eV, yellow-5 eV, blue-10 eV; pitch=30°, R=70 cm).
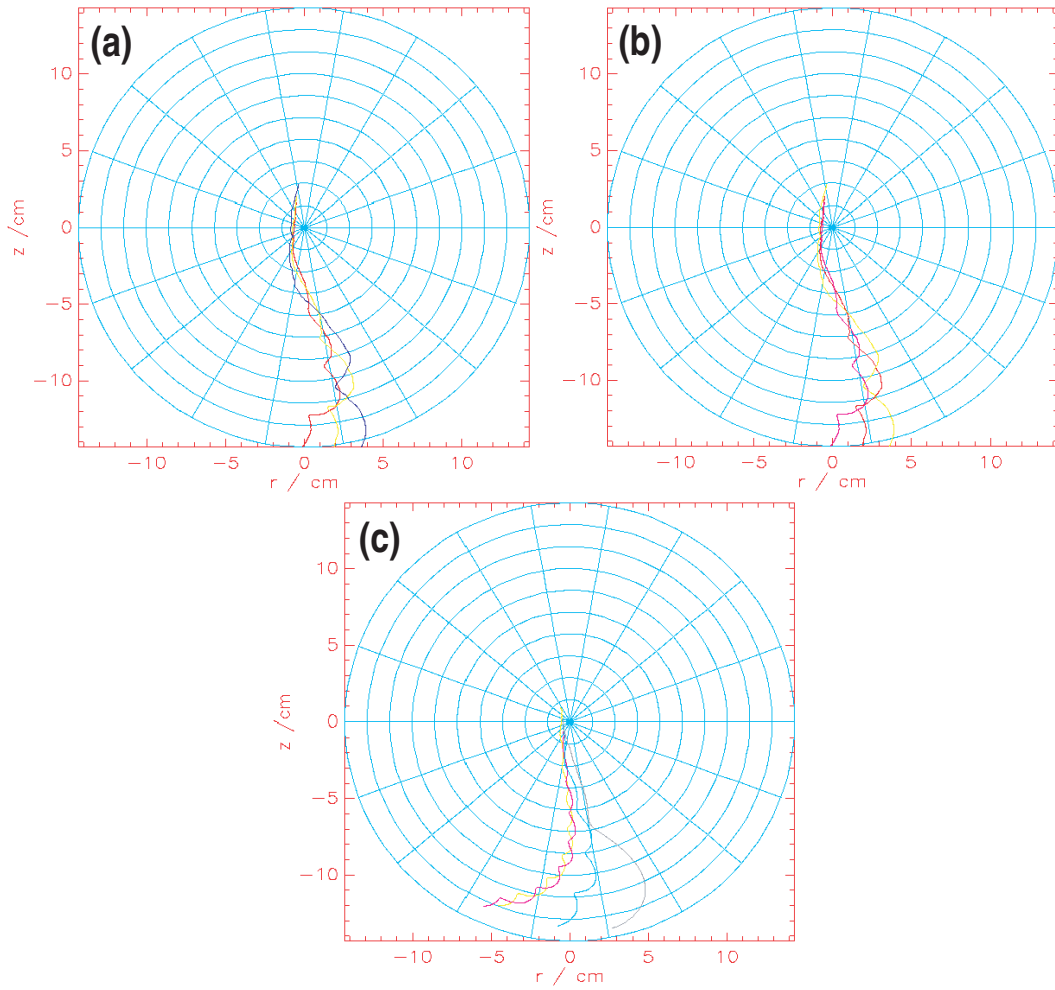

Figure 4.5: Ar$^+$ ion orbits for no (a), 80 V/m (b) & 800 V/m (c) radial electric field (red-3 eV, yellow-5 eV, blue-10 eV; pitch=30°; R=70 cm).

4.5(b) is already larger than the one measured in WEGA during common argon discharges. More to the radial electric field can be found in chapters 5 & 6.

Summing up the passage, it can be concluded that argon ions are not confined in WEGA by the magnetic field.

4.1.2   Heating Scheme

The plasmas investigated in this work are produced using microwave heating systems at a frequency of 2.45 GHz. The heating scenario was optimized for OXB-mode-conversion heating within the restrictions of the WEGA's port geometries [Pod06]. An O-Mode mode wave is launched from a double-slot antenna on the low-field side under an oblique angle of $\pm 42\,°$ to the magnetic field vector. The O-mode wave propagates up to the region of the O-mode cutoff layer ($n_e = n_{e,cutoff} = 7.5 \cdot 10^{16}\,\mathrm{m}^{-3}$), where the wave is partly converted into a slow-X-mode wave which propagates outward. The non-converted part of the O-mode wave is reflected. The SX-mode travels up to the upper hybrid resonance layer (UHR layer) where it is converted to an electrostatic Bernstein wave (EBW) [PK73]. The EBW then propagates inward. As the EBW does not have a density limit, the wave can reach the confined plasma region where it is absorbed by electron cyclotron damping. Figure 4.6 schematically illustrates the mode conversion process in WEGA.
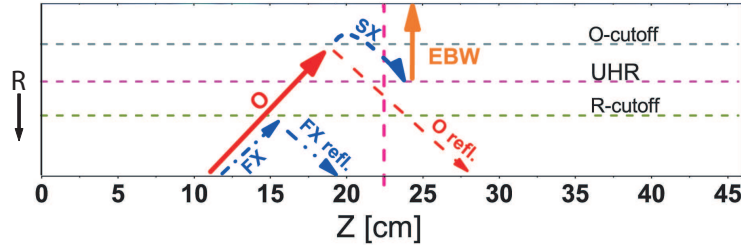

Figure 4.6: Mode conversion scheme for the ECR-heating scenario in low-field operation of WEGA, z is the distance in toroidal direction to the center of the double slot antenna (arrow for R indicates the direction of the major radius)
figure: courtesy of Y. Podoba [Pod06]

The electron temperature profiles in WEGA are typically hollow for operation in the low-field case ($B_{mod} < 90\,\mathrm{mT}$) as the wave is absorbed near, but inside the LCFS as has been predicted by full wave calculations and experimentally verified by Podoba [Pod06]. Optimum plasma heating for the 2.45 GHz system has been found at non-resonant magnetic flux densities being reduced compared to the nominal resonant fluxes to $0.65 \cdot B_{res} \approx 56\,\mathrm{mT}$ [PLW$^+$07].
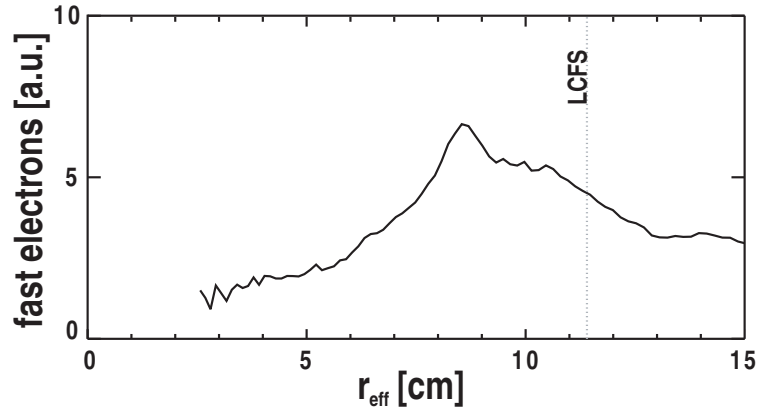
Figure 4.7: Super-thermal electron population originating of the heating mechanism for an argon discharge with $B_{mod} = 56\,\text{mT}$ and $t = 0.2$ produced using 6 kW ECRH power.

The resulting density profiles show values well above the cutoff density and are typically centrally peaked. The electron temperature profile shows a maximum around the LCFS as the majority of the heating power is absorbed there, creating a fraction of super-thermal electrons. The super-thermal electrons are used as an indicator for the power deposition. Their radial profile is shown in figure 4.7. This will be used in modeling the discharges later on.

4.2 General WEGA Diagnostics

The following section is devoted to the working principles of the used diagnostics as well as explaining various WEGA relevant changes to the usual proceedings when measuring with such systems. The diagnostics and other systems necessary for the work during this thesis are positioned at different toroidal angles as shown in figure 4.8. The diagnostics were chosen in order to have access to a large number of plasma parameters as well as basic machine characteristics. Not mentioned is the current measurement of WEGA's coil currents. A list of the used diagnostics can be found in table 4.1. For a better impression the diagnostic port's position is marked in figure 4.8. In addition to the diagnostics the antennas of the used ECRH system are included. The antennas are important when it comes to determining the last closed flux surface (LCFS) as they are acting as limiting objects to the plasma for the studied configuration.

In case of an inserted biasing probe the antennas will not limit the plasma, but the biasing probe will represent the inner most plasma-wall contact. The position

Name of the diagnostic (abbr.)	quantities measured	derived parameters	φ [°]
Ultra-high resolution spectrometer (UHRS)	$I(\nu, r_{eff})$	$I_0\left(r_{eff}\right)$ $T_i\left(r_{eff}\right)$ $v_i\left(r_{eff}\right)$	252
Fast reciprocating Langmuir probe (FLP)	$I(U, r_{eff})$	$T_e\left(r_{eff}\right)$ $n_e\left(r_{eff}\right)$ $V_{pl}\left(r_{eff}\right)$	144
Emissive probe	$V_{fl,\,Emi}$	$E_r\left(r_{eff}\right)$	144
Mach-Zehnder- interferometer (MZI)	$\Delta\Phi$	$\int n_e dl$	216
Biasing probe (BP)	U_{Bias}, I_{Bias}	P_{Bias}	108
Shunt resistors	$U_{Torus\,A\rightarrow gnd}$ $U_{Torus\,B\rightarrow gnd}$ U_{gnd}	$I_{Torus\,A\rightarrow gnd}$ $I_{Torus\,B\rightarrow gnd}$ I_{gnd}	-
Avalanche diode w/ filter	$U\left(\nu_{filter}\right)$	$I_0\left(\nu_{filter}\right)$	234
Bolometer	U_{Bolo}	$P_{rad}\left(r_{eff}\right)$	9

Table 4.1: Diagnostics overview (measured quantities, derived parameters and toroidal angle).
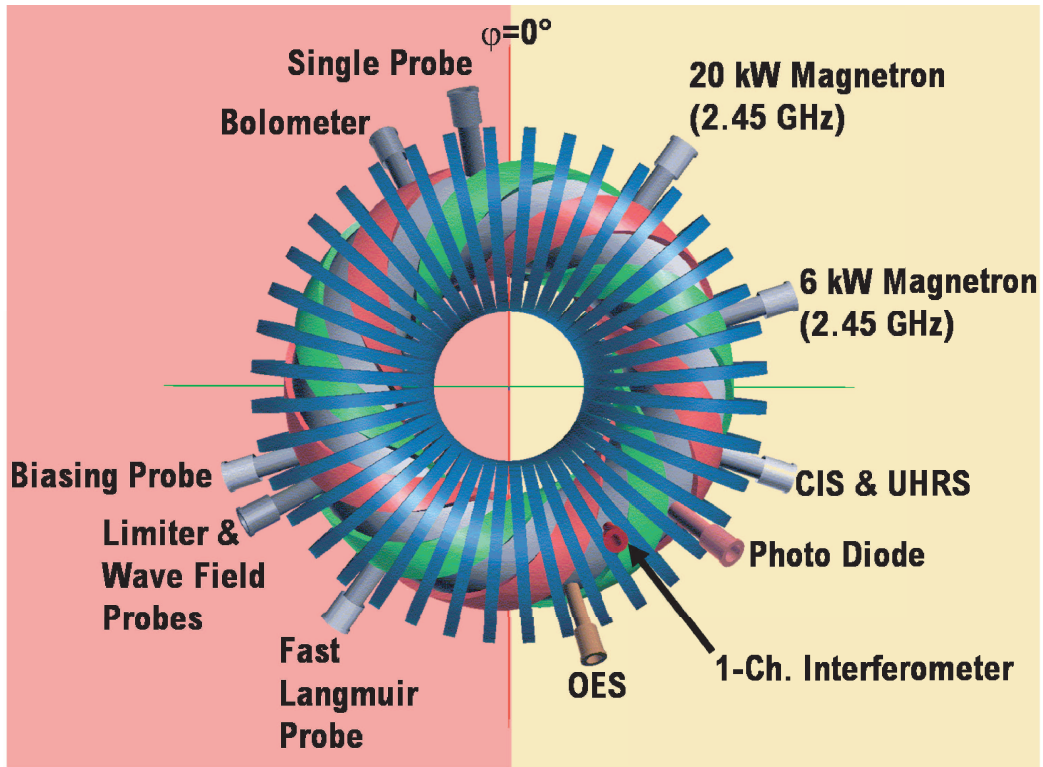

Figure 4.8: Positions of diagnostics, heating sources and important equipment at the WEGA stellarator, red and yellow underlay indicate the two isolated vacuum vessel parts (red-movable half-torus A; yellow-stationary half-torus B).

of the biasing probe tip is always indicated in the plots (BPtip), as is the position

of the last closed flux surface (LCFS) defined by the antennas. A more detailed analysis of the impact of the biasing probe can be found in chapter 5.3.

4.2.1 Mach- Zehnder- Interferometer

The interferometer is used to measure the line-integrated electron density. A finite plasma density leads to a change of the optical path in the measurement leg of the MZI, as the plasma is a dispersive medium. This change in the optical path results in a phase shift between the reference wave and the probing wave. A Mach- Zehnder-type interferometer consists of two legs, one being the reference leg, the other one being the leg containing the object to study - in this case the plasma. The principle of a Mach- Zehnder interferometer is sketched in figure 4.9.
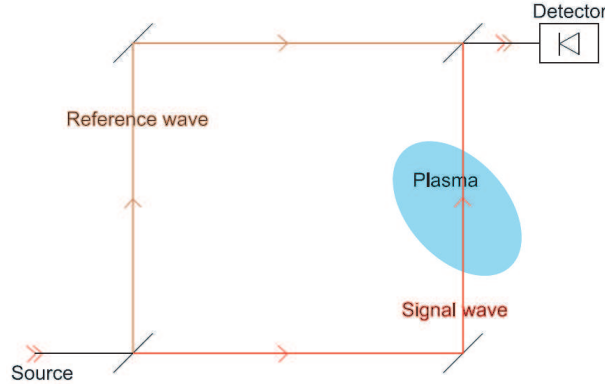

Figure 4.9: General layout of a Mach- Zehnder- type interferometer.

Due to the comparably low density the probing wave in WEGA is of rather long wavelength (2.54 mm). The interferometer measures the phase shift along the line of sight. The phase shift $\Delta \Phi_{MZI}$ is related to the electron density n_e via

$$\Delta \Phi_{MZI} \left(t \right) = r_e \cdot \lambda \int_L n_e \left(r', t \right) dr', \tag{4.1}$$

where r_e is the classic electron radius and λ is the probing wave's wavelength. Thus, the line-integrated electron density $\int n_e dl$ can be expressed as

$$\int n_e dl = 1.66 \cdot 10^{16} \cdot \Delta \Phi_{MZI} \left[\mathrm{m}^{-2} \right]. \tag{4.2}$$

In WEGA a single-channel Mach- Zehnder- type microwave interferometer (MZI) is placed at a toroidal position of $\varphi = 216\,°$. The line of sight of the interferometer does not cross the magnetic axis, as it is located around $R = 73\,\mathrm{cm}$. Figure 4.10

shows a typical $\iota = 0.2$- configuration at the toroidal position of the interferometer.

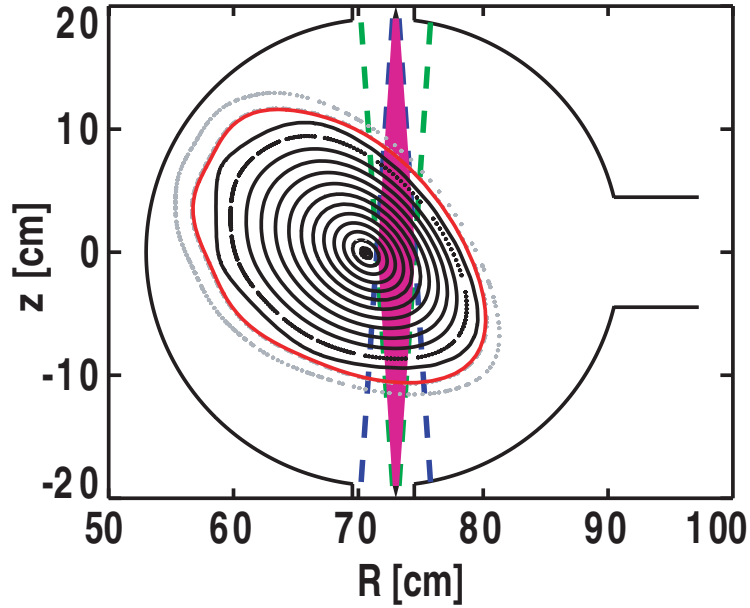Figure 4.10: Poincaré plot for the poloidal cross section of the Mach-Zehnder-type microwave interferometer ($\varphi = 216°$) for the reference configuration (dashed lines - antenna characteristics of the microwave horns; colored region - line of sight of the interferometer).

The line of sight is determined by the antenna characteristics of the two microwave horns. The interferometer does not relate to local values, thus, an additional profile diagnostic is required. Langmuir probes will be used as electron density profile diagnostic. More on probes can be found in chapter 4.4.

4.2.2   Avalanche Diode

An additional standard diagnostic used for monitoring light emission on WEGA is a single avalanche photo diode used in connection with multiple filters. The available filters cover different central wavelengths, corresponding to strong lines in the spectrum of the different working gases. Table 4.2 shows the central wavelength and the working gas of the different filters, as well as their bandwidth.

Central wavelength	FWHM	Gas
800 nm	10 nm	Ar
587 nm	10 nm	He
565 nm	10 nm	H_2

Table 4.2: Filters available for WEGA's avalanche photo diode setup.

The single line of sight is not only going through the edge regions of the plasma, but is also crossing the center of the plasma.
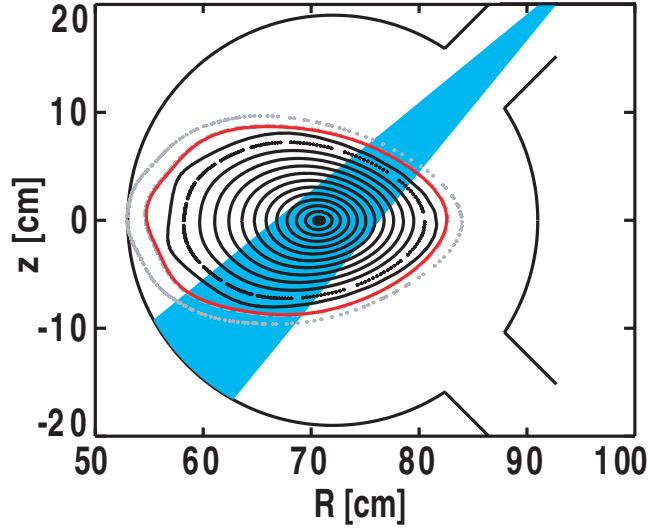

Figure 4.11: Line of sight of the avalanche photo diode on WEGA (for a 0.2- configuration).

The diode is positioned at a toroidal angle of $\varphi = 234\,°$. Its viewing area is shown in figure 4.11 for the case of the t=0.2 configuration. The neutral line emission intensity recorded by the avalanche diode acts as an indicator for energy losses due to recombination.

4.2.3 Shunt Resistors

A set of shunt resistors has been installed into the grounding network of WEGA to trace the biasing current. The shunt resistors allow measuring the biasing current distribution onto WEGA's two half tori. The set has primarily been installed in order to ensure that no secondary discharge channel is formed from the biasing probe onto specific in-vessel components, e.g. the heating antennas or the calorimetric limiter. As is has not been possible to isolate all in-vessel components, which are commonly grounded by contact with the vessel, the current on the respective half tori is a first indicator, if a component is connected directly to the biasing probe. In such a case, the biasing current flowing to the ground connection of the torus is registered by the shunt resistor. From the w7 code and experimental flux surfaces mapping the magnetic field of WEGA is well known. A direct connection (within one toroidal turn) of the biasing probe to e.g. the ECR heating antennas is not predicted by the

w7 code. The set of shunt resistors will primarily be used to verify this routinely. The position of the shunt resistors is indicated by the red arrows in figure 4.12 below. The black arrows indicate the industrial current flow direction of the currents drawn during positive biasing. The WEGA support structure is indicated by the gray lines.
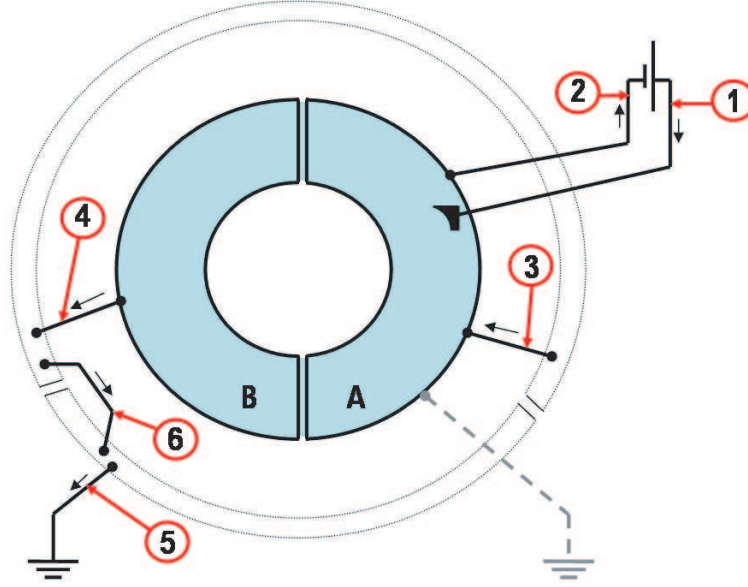

Figure 4.12: Placement of the shunt resistors (position indicated by red arrows & number) in the grounding concept of WEGA including biasing probe and parasitic grounding (dashed gray), also shown is the support structure of WEGA (gray lines), not shown are the isolators between the half tori as well as between the two parts of the isolated support structure; the plasma is represented by the light blue shade.

The current flowing between the biasing probe and half torus A is determined by exploiting Kirchhoff's current law. A schematic of Kirchhoff's current law for determining the current between the biasing probe and the WEGA half torus is indicated in figure 4.13.
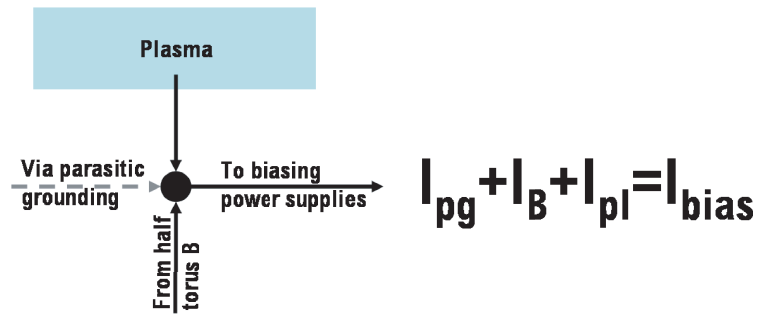

Figure 4.13: Schematic of Kirchhoff's current law for determining the current between the biasing probe and the WEGA half torus A (movable half).

The current from the plasma can hence be calculated by

$$I_{pl \to A} = I_{Bias} - I_B - I_{pg}, \tag{4.3}$$

with $I_{pl \to A}$ being the current drawn from the plasma onto the half torus A and $I_{Bias,B,pg}$ being the biasing current, current to half B and currents flowing over parasitic connections or in correspondence to figure 4.12:

$$I_{pl \to A} = I_2 - I_3 - I_5. \tag{4.4}$$

For more precise measurements of the current a set of current clamps can be used which have a much smaller measurement uncertainty of ± 0.15 A. The shunt resistors and the attached amplifiers are not expected to perform better than $15 - 20\,\%$, but this is more than sufficient for routine checks.

4.3 Ultra-High Resolution Optical Emission Spectroscopy

The following section will deal with the optical emission spectroscopy setup used on WEGA. Optical emission spectroscopy (OES) is a passive method of observing the plasma. It uses the electromagnetic radiation emitted by the plasma in the visible part of the spectrum. In order to obtain information about density, temperature and velocity of the emitting species, one can use a variety of different techniques, such as measuring relative line intensities [Hor04], highly resolve a single line [Lis05], defined multiplets [Chu04] or use the coherence imaging technique [How99]. For this thesis the highly resolved measurements of a single line is chosen. Ultra-high resolution spectroscopy is used in the context of this thesis to measure the poloidal flow velocity of the ions v_i, which can be related to the radial electric field in WEGA, as is explained in appendix A. The system is also capable of deriving the ion temperature T_i from Doppler broadening of a spectral line, as well as the intensity radiated by the selected transition $I_0(\lambda)$.

The section features a description of the ultra-high resolution optical emission spectrometer (UHRS), shown in figure 4.14. It is used in connection with a water-cooled back-illuminated Roper MicroMax frame-transfer CCD camera. CCD camera related issues can be found in appendix B, here only spectrometer related issues will be covered.

Figure 4.14: SOPRA 1150 mm UHRS system with prism-based pre-monochromator, fiber connector board and the attached water-cooled Roper MicroMAX back-illuminated frame transfer CCD camera.

The UHRS system shares a line of sight with the WEGA coherence imaging spectrometer (CIS) placed at $\varphi = 252°$. A sketch of the joint optical system is displayed in figure 4.15.
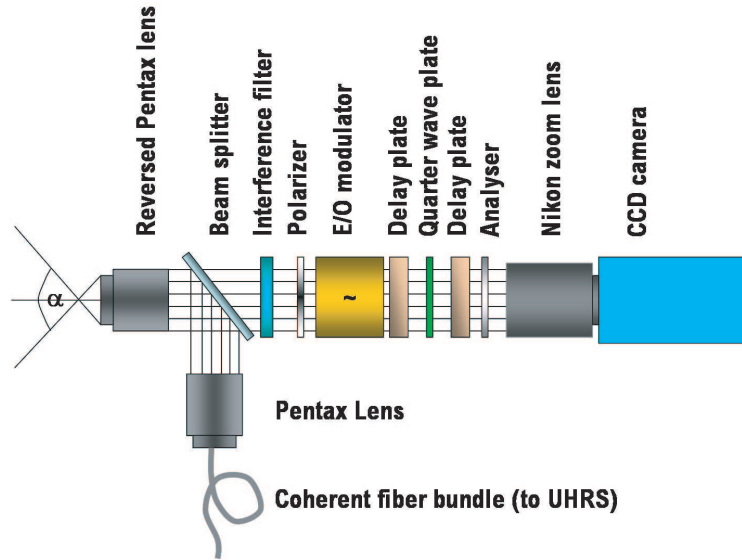

Figure 4.15: Joint optical setup of the UHRS and CIS optical diagnostics on WEGA.

The lines of sight cover most of the poloidal cross section of the plasma as can be seen in figure 4.16. The remarkable point of the optical system is that it allows obtaining an image with an infinite DOF for the CIS setup, as well as a limited DOF of $\approx \pm 1$ cm for the UHRS system. It is a system with a limited depth of field

conducting a local measurement - with local referring to averaging over the depth of field - although sharing the first lens with an infinite DOF system.
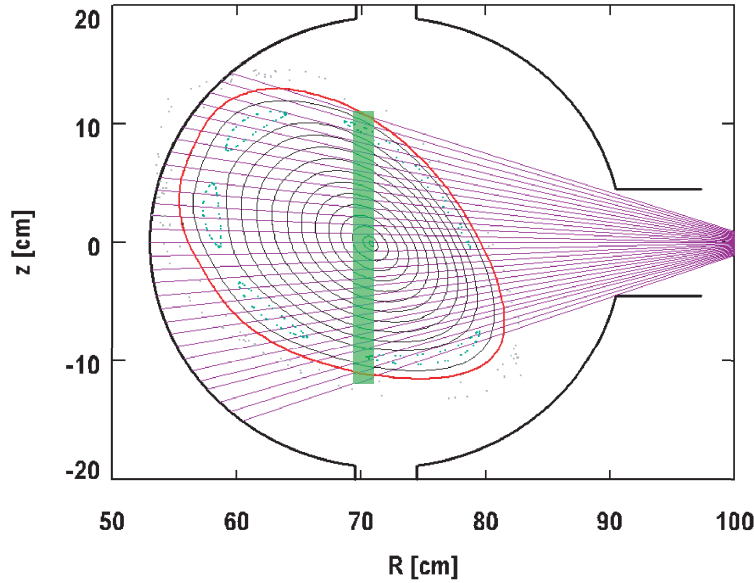

Figure 4.16: Lines of sight of the WEGA UHRS system for a large plasma configuration (finite DOF is indicated by green box).

The entrance slit of the pre-monochromator is formed by a set of 51 optical fibers glued together in the shape of a vertical line. Each fiber has a diameter of $200\,\mu$m and is connected to a connector board. This connector board allows to connect the fibers forming the entrance slit to the ones transferring the light from the WEGA port to the spectrometer system. The UHRS system itself consists of two spectrometers. First, a narrow part of the spectrum is selected using a prism-based pre-monochromator as can be seen in figure 4.17. The resulting low resolution spectrum is imaged onto the entrance of the main monochromator, a SOPRA 1150 mm Echelle grating spectrometer. A schematic of the system is shown in figure 4.17.
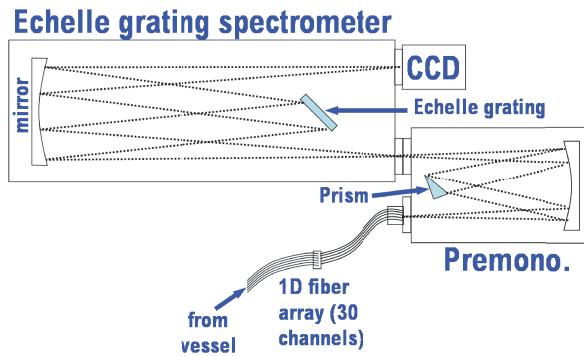

Figure 4.17: Layout of the ultra-high resolution spectrometer system on WEGA.

noindent Using a pre-monochromator allows avoiding different orders of diffraction overlapping on the CCD-chip at the end of the Echelle grating spectrometer.

The time resolution of the WEGA UHRS system is limited by the light intensity to typically $\Delta t = 1\,\mathrm{s}$. The ultra-high resolution spectrometer uses a small part of the full spectrum emitted by the WEGA plasma and resolves this fraction of the spectrum highly in the light's frequency.

The spectrometer is capable of monitoring light in eighth to 17th order of diffraction depending on the exact wavelength of the light. The order m can either be calculated by the spectrometer equation for a symmetric Ebert-Fastie spectrometer according to

$$\lambda_0 = m \cdot \lambda = k \cdot 2\sin\alpha_{blaze} \cdot \cos\varepsilon. \tag{4.5}$$

Here, λ_0 is the fundamental wavelength of the system, λ is the wavelength of the selected line, k is the grating constant, α_{blaze} is the blaze angle and ε is the Ebert angle. For the WEGA UHRS the characteristics are documented in table 4.3.

characteristic	value
λ_0	5706 nm
k	$\frac{1}{312}\,\mathrm{mm}$
α_{blaze}	63.2°
ε	4.2°

Table 4.3: Characteristics of the WEGA SOPRA 1150 mm Echelle grating spectrometer.

One specific treat of the WEGA UHRS system is that the system's dispersion relation is globally non-linear due to the fact that different orders of diffraction are covered by the instrument. One has to take into account that the dispersion of the system leads to a change in the effective resolution of the camera with some regions of the spectrum being higher resolved than others. Figure 4.18 shows the dispersion relation of the system. Jumps in the curve are due to a change in the order of diffraction. As the dispersion is rapidly changing at the wavelength of the selected argon ion line at 487.999 nm, mechanical movement of the spectrometer is critical. The absolute wavelength position on the camera is not precisely reproduced when moving the spectrometer.

As a more convenient reference for the absolute wavelength position, the line of sight running through the center of the plasma can be used as a reference for the velocity. This has been confirmed by using a Picarro CYAN diode laser at 488.0 nm as reference.
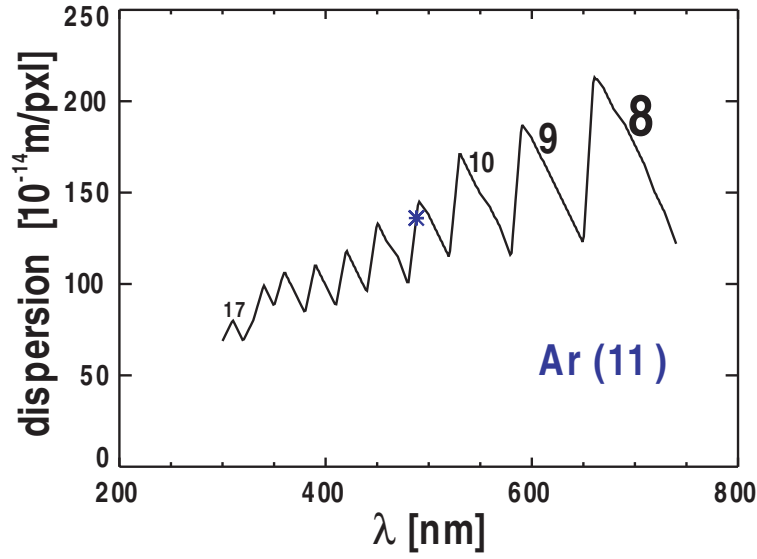
Figure 4.18: Dispersion relation of the UHRS over the wavelength - also indicated is the order in which the light is observed (number of order is given in parenthesis).

The laser has a full width at half maximum (FWHM) specified by the manufacturer to be less than 10^{-14} m. The typical resolution of the WEGA ultra-high resolution spectroscopy (UHRS) system is $1.36 \cdot 10^{-12} \frac{m}{pxl}$ at 488.0 nm. The laser can also be used to determine the instrument function at the wavelength. The instrument function of high resolution spectrometers changes with wavelength as the resolution of the system is wavelength dependent. For the selected argon line the instrument function has been determined to 0.1 Å.

4.4   Probes

A typical diagnostic for low temperature and low density plasmas is the electrostatic probe, also called Langmuir probe. The diagnostic has been introduced in the 1920's by Langmuir. A basic Langmuir probe consists of a metal wire, that is to some extend, exposed to the plasma to be diagnosed.

If an electrically isolated probe is immersed in a plasma more electrons than ions hit the surface as the thermal velocity of the electrons is higher than the ion's thermal velocity. The probe is charged negatively with respect to the plasma. To preserve quasineutrality ions from the plasma will surround the probe shielding the excess negative charge until the electron and ion current to the probe are equal. The resulting potential of the probe is called floating potential V_{fl} and is more negative than the plasma potential at the position of the probe.

Depending on the probe potential three different regimes can be found:

1. Ion saturation branch ($U \ll V_{fl}$)

2. Electron residual current region (shaded region in figure 4.19(a))

3. Electron saturation region (not shown in figure 4.19)

If the probe is biased to potentials less than $\approx 2V_{fl}$ [Ott00], only positively charged particles are able to reach the probe surface. Negatively charged particles (electrons) are repelled by the probe. This regime is called ion saturation branch of the characteristic. With more positive probe bias also electrons are able to reach the probe. The current contribution of the electrons is depending on the electron density as well as the electron energy distribution function. The residual electron current is growing exponentially with the probe voltage in case of a Maxwellian energy distribution. The corresponding regime of the current-voltage characteristic is called electron residual current region. Finally, the probe bias is exceeding the plasma potential. Now ions are repelled by the probe and only electrons are able to reach it. This regime is called electron saturation current. Depending on the probe geometry, the electron saturation current may not saturate to a constant value. This is observed in the cylindrical probes as used in WEGA.

Important plasma parameters, such as n_e, T_e, V_{pl} as well as the energy distribution function of the electrons $f(E)$ can be determined from probe characteristics under optimum conditions [Ott00]. For the conditions in WEGA not all of this is possible as the presence of the magnetic field and the applied heating method make interpretation more difficult. A second important aspect is the presence of super-thermal electrons in the edge, which have a significant impact on the probe characteristic [Sta95b]. Also, the probe dimensions are similar to relevant scale lengths in the plasma [Mar08]. The high noise level requires careful treatment and renders common techniques for determining the electron energy distribution inapplicable. A typical WEGA probe characteristic is displayed in figure 4.19. As can be seen the probe current displayed in figure 4.19 does not saturate completely for negative voltages.

The most robust parameter to be derived from Langmuir probes is the electron temperature. In case of a Maxwellian electron energy distribution function, the drawn electron current I_e is exponentially increasing with the probe voltage U in the electron residual region:

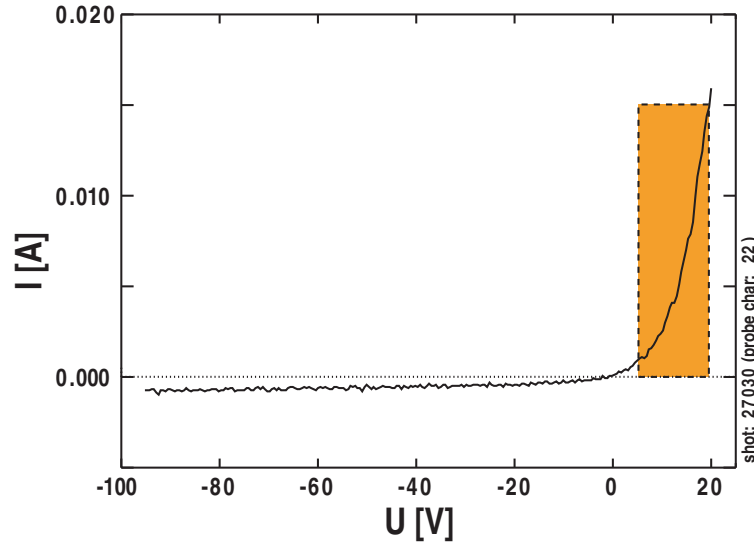$$I_e = I_{e,\,sat} \cdot \exp \frac{e\,(U - V_{pl})}{k_B T_e} \tag{4.6}$$

Figure 4.19: (a) Typical current- voltage characteristic of a WEGA Langmuir probe, shaded area can be used to derive electron temperature.

with $I_{e,sat}$ being the electron saturation current, V_{pl} the plasma potential and T_e the electron temperature. Equation 4.6 can be used to derive the electron temperature from the slope of a semi-logarithmic plot of the probe data as is shown in figure 4.20. In this case the electron temperature is derived to $T_e \approx 4.75\,\text{eV}$.
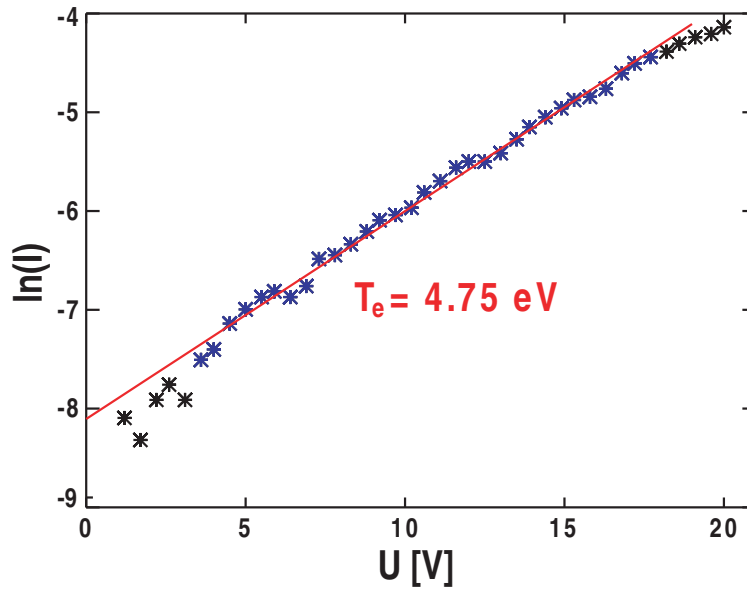

Figure 4.20: Shaded region of figure 4.19 as semi-logarithmic plot (black - data, blue - used for fit, red - fit) with derived electron temperature.

In the following a short overview related to probe measurements and their application under WEGA's plasma and probe conditions is given. For a more detailed

overview of using probes in the WEGA environment please refer to [Mar08] and references therein.

4.4.1 WEGA Langmuir Probe

A typical WEGA Langmuir probe has cylindrical geometry. It is built from tungsten wire, having a probe tip diameter of $100\,\mu$m and an exposed length of a few millimeters. The probe shaft is isolated from the tip by a ceramic tube. The schematic in figure 4.21 shows the typically employed Langmuir probe design as used on WEGA.

Typical WEGA plasmas generally do not limit the use of probes, however several precautions have to be taken in order to ensure the persistence of the probe in the environment of WEGA. The probe system is exposed to the plasma for only a very short time period (typically a second) in order to prevent the probe from thermal damage. This is done by a pneumatically-driven fast reciprocating midplane manipulator giving the system its name: FLP - Fast Langmuir Probe.
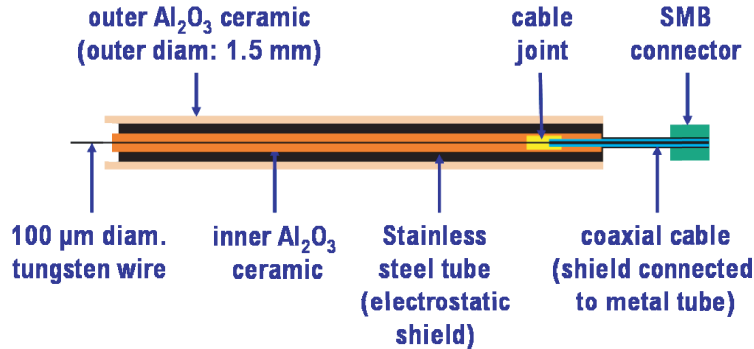

Figure 4.21: WEGA Langmuir probe (tungsten, $100\,\mu$m).

The current setup can hold up to 14 probes. Thirteen probes are positioned to form a poloidal array with a vertical distance of 0.5 cm between the probes and one additional probe can be mounted slightly elevated between the probes at z=0 and 0.5 cm (not shown in graph). This additional holder is used to mount the emissive probe which will be introduced in chapter 4.4.2. A schematic of the FLP probe array in the reference configuration is shown in figure 4.22. The probe array fits to the LCFS of a $\iota = 0.25$ configuration [Mar08].

Determining plasma density or plasma potential, in order to gain accurate quantitative information about plasma parameters, is not easy under WEGA conditions, as is described in [Mar08].
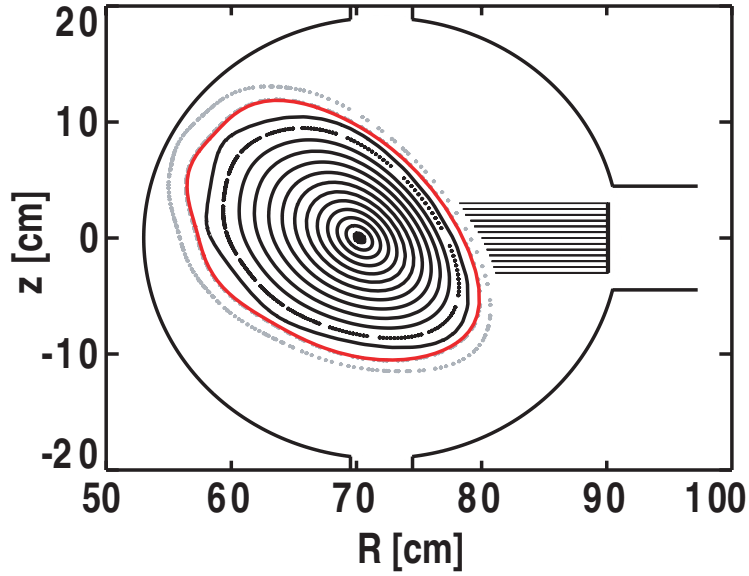
Figure 4.22: Sketch of the 13 tip Langmuir probe array on WEGA in reference configuration.

Careful interpretation of the probe data is required. The equations describing the motion of the plasma change their character due to the boundary formation of the probes. This point in particular is explained in more detail in [Che77]. In case of the standard Langmuir probe operated in WEGA, having a probe radius of $R_p = 50\,\mu\text{m}$, probe theory according to Allen, Boyd and Reynolds [ABR57] is used. The theory assumes a Maxwellian electron energy distribution. The ion density, n_i, is derived from the ion flux, Γ , per unit length, $2\pi r$, of the probe as

$$n_i v_i = \frac{\Gamma}{2\pi r}, \tag{4.7}$$

with $v_i = \sqrt{\frac{-2eV}{M}}$ and M being the ion mass and V the potential difference between the probe and the plasma potential. The above equation can be used to rewrite Poisson's equation to be,

$$\frac{1}{r}\frac{\partial}{\partial r}\left(r\frac{\partial V}{\partial r}\right) = -\frac{e}{\varepsilon_0}\left[\frac{I}{2\pi r}\frac{1}{\sqrt{\frac{-2eV}{M}}} - n_0 \exp\left(\frac{eV}{k_B T_e}\right)\right]. \tag{4.8}$$

n_0 is the density far away from the probe. Using the normalized temperature $\eta = -\frac{eV}{k_B T_e}$ and the normalized probe radius $\xi = \frac{r_{probe}}{\lambda_D}$ with $\lambda_D = \sqrt{\frac{\varepsilon_0 k_B T_e}{n_0 e^2}}$ and the normalized probe current to the probe $J = \frac{eI}{2\pi k_B T_e}\sqrt{\frac{M}{2\varepsilon_0 n_0}}$ equation 4.8 can be

rewritten as

$$\frac{\partial}{\partial \xi} \left(\xi \frac{\partial \eta}{\partial \xi} \right) = J\sqrt{\eta} - \xi \exp\left(-\eta\right). \tag{4.9}$$

According to Chen [Che01, Che03], the solution of this differential equation can be fitted by

$$\frac{1}{J^4} = \frac{1}{(A\eta^B)^4} + \frac{1}{(C\eta^D)^4}, \tag{4.10}$$

with A, B, C and D according to

$$\begin{aligned} A, C &= a\xi^b + c\xi^d \\ B, D &= a + b\ln\xi + c\left(\ln\xi\right)^2 \end{aligned} \tag{4.11}$$

and a, b, c & d from table 4.4.

Probes also introduce a systematic error onto the measurements. As the probe is essentially a surface, the plasma density in front of the probe will be reduced. In combination with the probe movement, this would lead to a rectification of the probe profiles and the density measured in the center will be underestimated.

As an absolute reference plasma to calibrate the probes is lacking, the absolute calibration of the system is done by mapping the probe results to the interferometer line of sight and comparing the two.

	a	b	c	d
A	0.864	1.500	0.269	2.050
B	0.479	-0.030	-0.010	-
C	1.008	1.700	0.336	2.050
D	0.384	-0.150	0.013	-

Table 4.4: Coefficients for computing ABR curves according to Chen. [Che01, Che03]

When comparing probes to the interferometer, the plasma existing outside the LCFS plays a critical role as has been noted before [Hor04, HLLW04]. Figure 4.23 indicates the mapping procedure which is used to map the probe data to the interferometer line of sight for comparison. The comparison of the interferometer to the probe data yields a correction factor γ describing the ratio between the mapped probe results and the MZI signal. The correction factor is then used to rescale the probe data according to

$$\int\limits_{-r}^{r} n_e\left(r\right) dl_{MZI} = \gamma \int\limits_{t_0}^{t} n_e\left(r\right) dl_{FLP}. \tag{4.12}$$
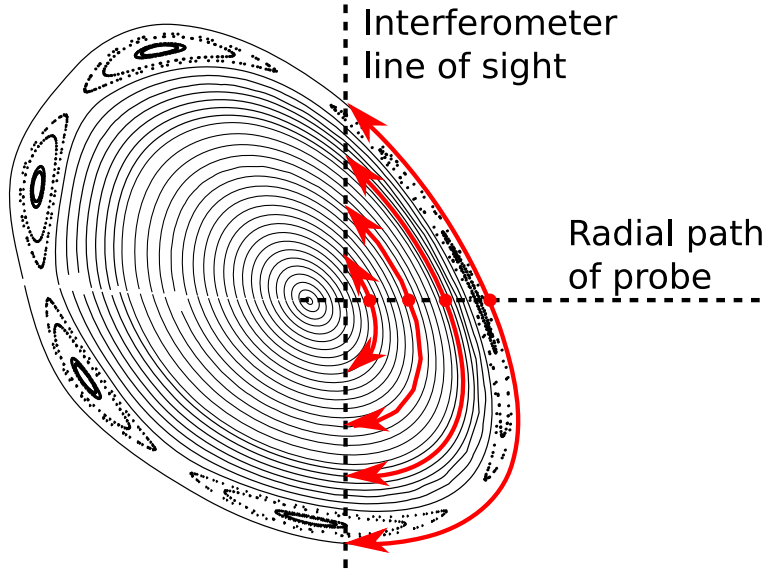
Figure 4.23: Simplified sketch of the mapping procedure used for comparing the probe data to the Mach- Zehnder- interferometer.
figure: courtesy to Dr. S. Marsen

Aside from the principle issues related to probe measurements in magnetized plasmas another thing has to be considered. The WEGA Langmuir probe is mounted on a fast moving manipulator. One has to consider a possible obscuring of the profile due to the manipulator movement. The typical sweep time is about 3 ms for a single characteristic, corresponding to a radial displacement of ≈ 5 mm in the edge region. The displacement in the plasma region is smaller than 3 mm per characteristic even for the fastest setting of the manipulator. The movement of the probe, in combination with the finite size of the probe, is limiting the number of supporting points to a parameter profile. Probe profiles presented within this thesis are spline interpolations to these supporting points.

4.4.2 Emissive Probe

As mentioned in [Mar08], the reconstruction of the plasma potential profiles from standard probe results is not reasonable for the low field operation of WEGA. In order to gain access to information about the radial potential distribution and its derivative, the radial electric field, a different approach to measuring the potential distribution has to be chosen. The potential distribution of the plasma can be obtained using emissive probes. The working principle will be explained in the following.

An electrostatic probe emitting electrons is called emissive probe. The most

simplistic realization is a wire heated to thermal emission [SS96]. More advanced
designs have been realized using self emitting probe tips [RLB$^+$97] or materials such
as lanthanium hexaboride (LaB$_6$) [Fin02] or even a combination of LaB$_6$ with lasers
as presented in [SIB$^+$08]. Common to all designs is that all probes have to provide
a sufficient emission current of thermally emitted electrons following Richardson's
law

$$j_{emi} = A_R T^2 \cdot e^{-\frac{e\Phi_W}{k_B T_H}}, \tag{4.13}$$

with Φ_W being the work function of the material (for W: 4.6 eV) and T_H being
the temperature of the emitting material. A_R is Richardson's constant, which is
dependent on the material and its surface (for W: 60 Acm^{-2}).

A typical current-voltage characteristic of an emissive probe is displayed in figure
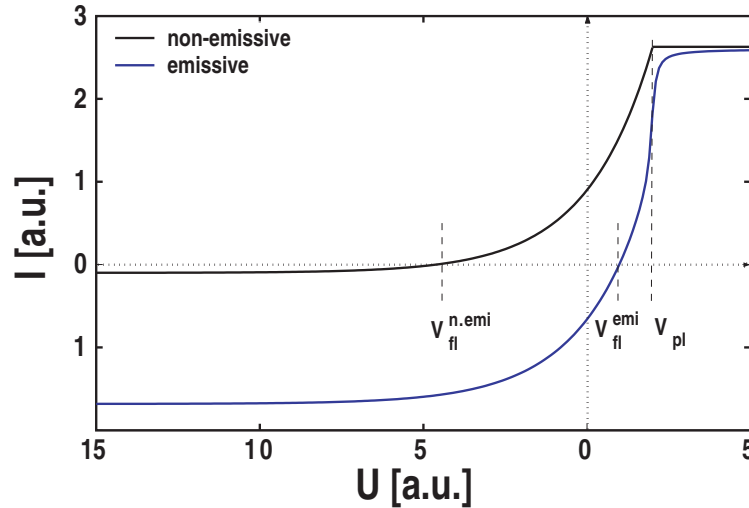4.24.

Figure 4.24: Calculated current-voltage characteristics of a planar emissive and a
planar non-emissive probe of equal dimensions.
figure: courtesy to Dr. M. Fink

The additionally emitted current of the emissive probe is added to the ion sat-
uration current. The electron saturation current remains unchanged. The floating
potential of the emissive probe is closer to the plasma potential than the one of the
conventional probe. The cause for this shift is the change in the sheath in front
of the probe. The electron sheath surrounding the probe prevents the collection of
electrons from the plasma. Hence, the floating probe will charge up less negatively
with respect to V_{pl} than in case of a cold probe. The emission of the probe leads
to a reduction of the sheath potential of the probe. In a crude approach emission
can fully destroy the sheath if as many electrons are emitted from the probe as are

collected from the plasma. According to [Rei98], the potential drop of the sheath to the probe, V_X, can be derived to be

$$V_X = V_{fl}^{emi} - V_{pl} = -0.6 \cdot \frac{k_B T_e}{e}. \tag{4.14}$$

Before the sheath potential can reach the plasma potential, the electric field surrounding the probe is reversed if the ratio of emitted (j_{emi}) to collected current ($j_{e,P}$) becomes larger than 0.86. A double sheath is formed. If the ratio of emitted current to collected current becomes larger than 1, the probe is called sufficiently emitting. In practical terms the current for a tungsten wire emissive probe is sufficiently emissive if the emission current $j_{emi} \gtrsim 1.0 \, \mathrm{Acm}^{-2}$ [Fin02]. The sufficient degree of emission of the probe is displayed in figure 4.25.
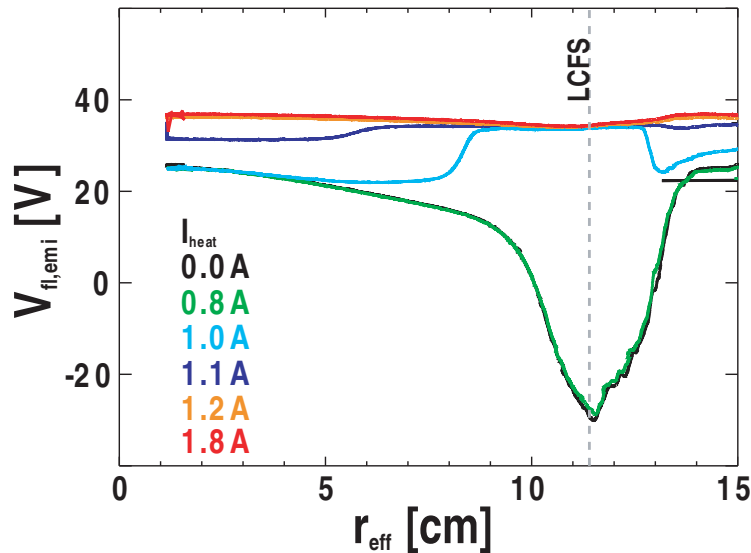

Figure 4.25: Floating potential profiles of a tungsten wire emissive probe at different heating currents; sufficient emission is achieved with heating currents larger than $I_{heat} \geq 1.2 \, \mathrm{A}$.

The gradual transition from a standard floating probe to an emissive one is visible. Also the difference in the plasma temperature leads to a stronger emission in the edge compared to the center if the probe is just not sufficiently emissive as is the case for the light and dark blue curves of figure 4.25. The emissive probe is operated at heating currents $I_{heat} > 2.0 \, \mathrm{A}$ at all times in order to ensure a proper degree of emissivity. As emissive probes suffer from short lifetimes, a simple flexible wire has been spliced to the tungsten filament as is suggested in [SS96]. The emissive probe consists of a $100 \, \mu\mathrm{m}$ diameter tungsten wire which is spliced into a $0.25 \, \mathrm{mm}^2$ flexible copper wire. This allows easy replacement of a broken tungsten filament.

More to designing an emissive biasing probe can be found in chapter 4.5.2. The emissive probe for profile measurements has been available in the last experimental campaign. Otherwise measurements of the radial electric field are conducted spectroscopically.

4.5   Biasing Probes

As mentioned in the introduction biasing probes will be used to alter plasma parameters, especially the radial electric field profile. Following the threshold power scaling given in formula 1.2, the access to improved confinement regimes requires a certain minimum heating power. This power threshold is well outside any operational window of WEGA giving $P_{thres} \geq 100\,\mathrm{kW}$ for low field operation even with a very small and dense plasma. Hence, biasing is not conducted to achieve H-mode plasmas, but to study more basic effects such as the impact of the probe onto the plasma parameters and to demonstrate the ability to modify the radial electric field.

The biasing probe setup for WEGA is located at a toroidal angle of $\varphi = 108\,°$. Two different classes of biasing probes are available for conducting biasing experiments on WEGA. One is a set of carbon probes of different sizes and shapes. The other is a large tungsten emissive probe. Both sets will be introduced in the following. As only one probe can be used, the probe in use will always be referred to as "the probe" or "the probe head", if not specified in more detail. The biasing probe is mounted on a stainless steel rod for the carbon probes and on a set of solid copper rods for the emissive tungsten probe. In both cases the conductor is covered by ceramic tubing to provide electrical as well as thermal shielding from the plasma. The probe system is radially movable by means of a slow mid-plane manipulator allowing precise (±0.3 mm) positioning of the probe head.

The biasing probes can be energized using two power supplies each providing up to ±600 V/25 A. Both power supplies are operated in parallel allowing a combined maximum current of 50 A at ±600 V with respect to the vacuum vessel in steady-state. The emissive probe will be heated by an auxiliary power supply capable of supplying 100 V and currents up to 500 A.

4.5.1   Carbon Probes

Carbon biasing probes are often used in biasing experiments due to the advantageous thermo-mechanical properties of carbon. The ability to take high thermal loads was

the main reason to use carbon as a candidate material for building WEGA's biasing probes. Initially, a small mushroom-shaped biasing probe was available. As it became obvious that the probe was not able to drawn significant current, two larger probes have been constructed.

As first candidate when a large and distinct surface was required, the block design has been used. This design incorporates a well-defined connection to the plasma as well as a rather large and mechanically stable body to take the heat load during biasing. A picture of the block probe is shown in figure 4.26.
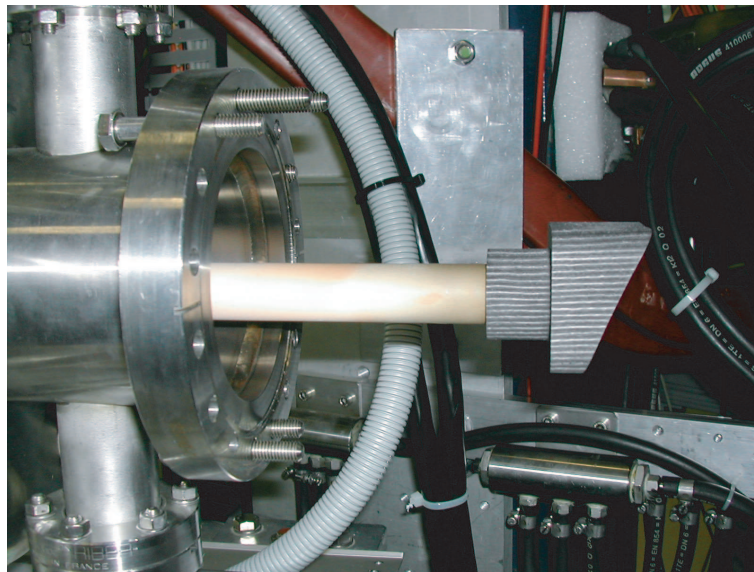

Figure 4.26: LCFS-shaped carbon block probe installed on the manipulator (in air)

The probe has a base width of 50 mm and a height of 50 mm. The front of the probe is a square with rounded edges. The front is cut to match the contour of the magnetic field geometry of the last closed flux surface. The probe proofed to be very robust against both large heat loads as well as mechanical vibrations. The main results presented in this thesis have been obtained using this probe.

A more sophisticated carbon probe tip matching the LCFS better has been used to check if the biasing scenario can be optimized by using a larger surface in contact to the plasma. The second design sacrifices the very stable body for a larger contact surface to the magnetic geometry. The results obtained when biasing do not differ significantly from the use of the block probe, although the general plasma parameters were slightly better. Results obtained with this probe will only be shown in section 6.4, as the general behavior was not much different. It is optimized for use with the $\iota = 0.2$- configuration, as is the block design. A picture of the LCFS-shaped disc probe is shown in figure 4.27.
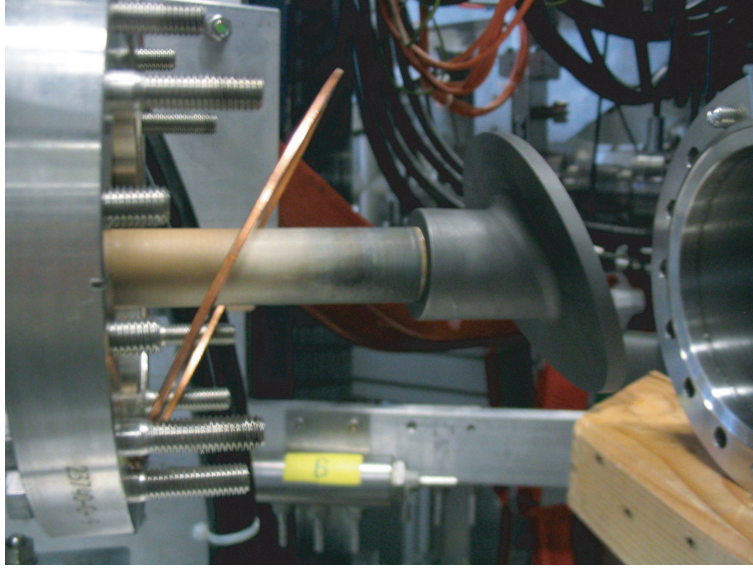
Figure 4.27: LCFS-shaped disc biasing probe installed on the manipulator.

The front of the probe has a rather complicated shape as it is matching the LCFS. It's front projection is a circle with a diameter of 80 mm. The probe tip has a thickness of 5 mm.

4.5.2 Tungsten Emissive Biasing Probe

Returning back to the roots of edge biasing, the idea is to draw large currents perpendicular to the magnetic field respectively across flux surfaces. Since the biasing probes are essentially large Langmuir probes, negative biasing has always been limited to the ion saturation current. This limitation can be avoided by using emissive probes. Here, one is able to draw significantly larger currents with negatively biased probes due to additionally produced free electrons from thermal emission from the heated surface. In a rather simple case one can think of an emissive probe as a loop of tungsten wire heated into emission. The emitted electron current I_e can be described according to the Richardson formula given in equation 4.13. In order to draw more current with such a probe, one can either increase the probe's surface or increase the temperature. A larger surface is not always wanted. Ideally, one wants to keep the probe small to minimize the perturbation caused by the probe body. An increase in temperature imposes a significant limitation on the lifetime of an emissive probe as has been reported in [Fin02]. Also the mechanical stability of the probe is reduced for higher temperature. This is important as significant forces due to $\vec{j} \times \vec{B}$ force act on the probe even with the comparable low magnetic field.

For the use in WEGA the biasing probe is to deliver between 3 and 30 A emissively. This can be achieved by a tungsten wire with a surface of $10\,\mathrm{cm}^2$ being heated to approximately 2600 K. The heating of the wire is done electrically. The amount of power needed can be estimated by Stefan-Boltzman law to

$$P = \sigma_{SB} \cdot S \cdot T^4, \tag{4.15}$$

here σ_{SB} is the Stefan-Boltzmann factor, S the probe surface and T is the temperature of the probe. Given a temperature of 2500 K, the loss due to black-body radiation is $\approx 2.5\,\mathrm{kW}$. This has to be compensated by the electric heating circuit. One has to keep in mind that the emissive probe is intrinsically a resistor and that the resistance is changing as the probe becomes hotter. This increase of the resistance can be described by

$$R(T) = R_{20} \cdot (1 + \alpha \Delta T). \tag{4.16}$$

with α being the linear resistance temperature coefficient and $\Delta T[K] = T[K] - 293.15\,\mathrm{K}$. The resistance changes from $R_{20} \approx 0.2\,\Omega$ to $R_{2700} \approx 2\,\Omega$. The change of the probe's internal resistivity can be used as a measure of the probe temperature according to the formula above. The emissive current of the probe can be cross-checked in such fashion. Both above mentioned relations are shown in graph 4.28.
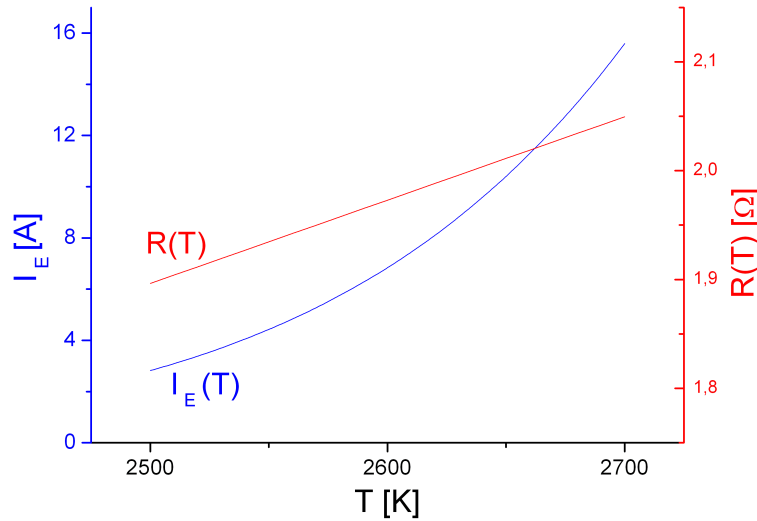

Figure 4.28: Emission current and resistivity of the WEGA's tungsten wire emissive biasing probe ($S = 10\,\mathrm{cm}^2$).

In order to decrease the required heating one could turn to a different material

having a lower work function. One could use thoriated tungsten instead of regular tungsten reducing the work function by about a factor of 2. Since thorium is evaporating when the probe is heated to emission, one observes an even shorter lifetime when compared to pure tungsten probes. In order to minimize the maintenance of the emissive probe setup in WEGA, this was not chosen. Also, a thoriated tungsten wire is mechanically not as robust as pure tungsten wire is. A different possible material would be lanthanium hexaboride (LaB_6). LaB_6 is similar to chalk in consistency. LaB_6 has a work function of $W_a = 2.6\,\mathrm{eV}$, similar to that of thoriated tungsten ($W_a = 2.7\,\mathrm{eV}$) and has been successfully used in many machines to construct emissive electrostatic probes. It was chosen not to use LaB_6 due to the fact that the exposure to plasma erodes the material quite fast and the probe head would be disintegrated rather quickly. This is accompanied by contaminating the vessel with lanthanium hexaboride dust, which is a health risk. As access to the vessel is very limited in terms of cleaning large surfaces and in order to avoid health risks, the material is not used.

In order to obtain the required surface area of 10 cm^2, the tungsten emissive probe was chosen to be essentially a small coil made of 1 mm diameter tungsten wire. The coil is mounted to the tip of two solid copper rods that are electrically isolated as well as thermally shielded from the plasma by aluminum oxide ceramic tubes. The system is mounted on the same slow mid-plane manipulator as the carbon probes, so also a well-known position can be obtained. A picture of the emissive probe in a test chamber is shown in figure 4.29.
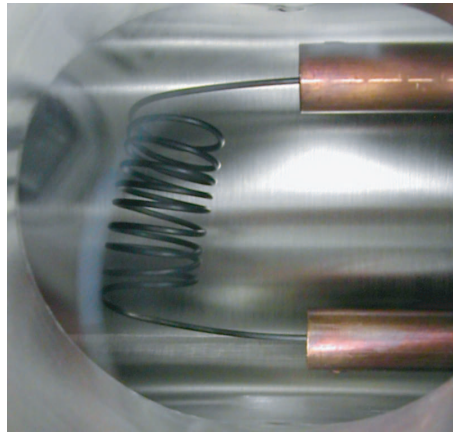

Figure 4.29: Emissive tungsten biasing probe in test chamber (without shielding ceramics).

As with the carbon probes, two power supplies in joint-operation mode allow biasing currents up to 50 A and a biasing potential of up to $\pm 600\,\mathrm{V}$. The ohmic

heating of the tungsten wire is supplied by additional power supplies floating at the potential of the biasing power supplies. Typical heating currents exceed 90 A.

4.6 Bolometry

In order to measure the radiated power onto a surface, bolometry is a well-suited and widely used tool. A bolometer measures the power flux onto the surface of the bolometer by a change in temperature of the detector. The principle of bolometry has been introduced 100 years ago by Langley [LA08]. The base for this temperature measurement is a Wheatstone bridge circuit. A WEGA bolometer is formed by two sets of two gold meanders of equal length on an insulator foil [MVA⁺91, ZOG05]. A basic sketch of a single bolometer is shown in figure 4.30.
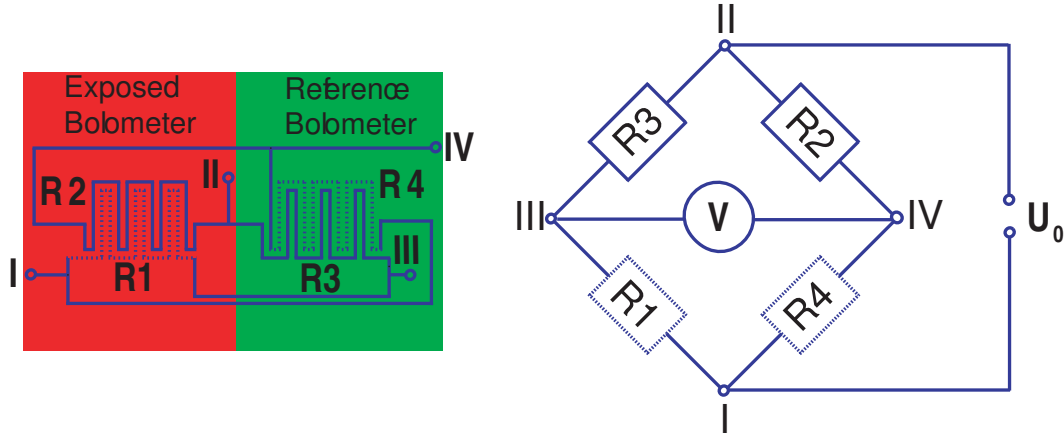

Figure 4.30: Basic draft the electric circuit of a bolometer and the corresponding Wheatstone bridge circuit; R1 & R2 are exposed to the radiation from the plasma.

The WEGA bolometer system of 12 channels placed inside the bolometer uptake. If not exposed to radiation the Wheatstone bridge is balanced as all resistors are equal:

$$R_1 = R_2 = R_3 = R_4 \quad \text{and} \quad V \equiv 0 \tag{4.17}$$

If the bolometer is exposed to radiation, the resistors R_1 & R_2 heat up changing their resistivity. In consequence, the Wheatstone bridge is unbalanced and a voltage V can be measured across the bridge according to

$$V = U_1 - U_4 = \frac{\alpha \Delta T}{2 + \alpha \Delta T} \cdot U_0. \tag{4.18}$$

Sorting for ΔT the temperature change in the resistors can be expressed as

$$\Delta T = \frac{2V}{\alpha \left(U_0 - V\right)},$$

where U_0 is the supply voltage to the bridge (applied between I & II in figure 4.30). The radiated power can be calculated from the bolometer equation

$$P_{rad} = c \left(\frac{dT\left(t\right)}{dt} + \frac{T\left(t\right) - T\left(t_0\right)}{\tau} \right). \tag{4.19}$$

The parameters c and τ correspond to the heat capacity and the characteristic cooling time of the bolometer. The WEGA bolometer is calibrated by ohmic heating after every WEGA discharge, which is described in detail in [Sch99].

The bolometer is installed at a toroidal angle of $\varphi = 27°$. The bolometer lines of sight cover most of the poloidal cross section, as can be seen in figure 4.31.
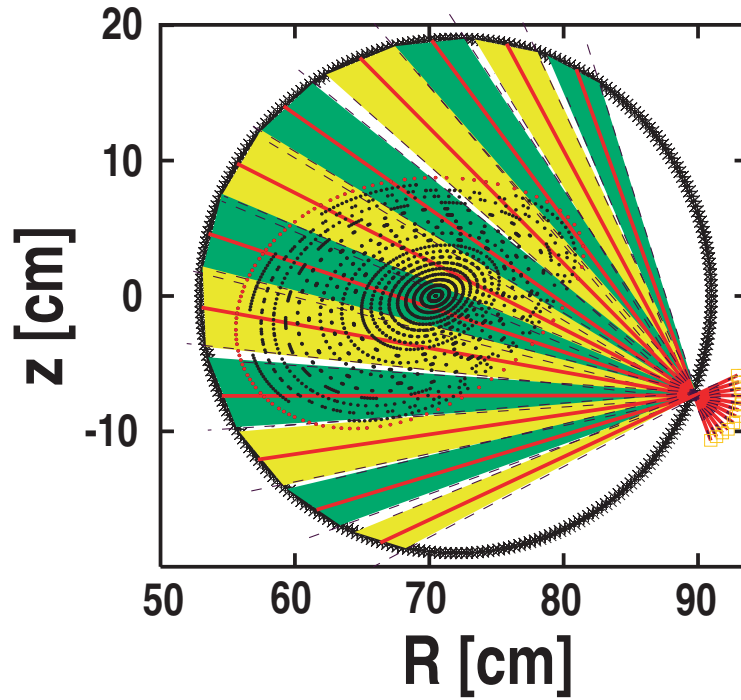

Figure 4.31: Lines of sight of the WEGA bolometer.
figure: courtesy to Dr. D. Zhang.

The bolometer will be used as reference measurement for the radiated power flux emitted from the WEGA plasma. This includes radiation from neutrals and radiation from not fully-ionized ions.

4.7 Limiter

WEGA features a calorimetric limiter at a toroidal position of $\varphi = 117°$. The distance between the limiter and the biasing probe is typically not larger than $\approx$ 10 cm, if installed. The limiter consists of stainless steel and can be actively cooled with water. Temperature sensors at the feed and the exit of the limiter allow using it as a calorimeter. The limiter is also referred to as calorimetric limiter for this purpose. Figure 4.32 shows the limiter installed in WEGA during plasma ignition.

Figure 4.32: Picture of the calorimetric limiter (top right structure) obtained during the ignition of a WEGA discharge acquired with a video camera looking into the WEGA vacuum vessel; also shown is the casing of the internal diamagnetic loop and a second video camera.

If present in the vessel, the limiter has been placed in the far SOL, not limiting the plasma. The size of the plasma has been limited by the presence of the heating antennas or the biasing probe for all cases in this thesis. Nevertheless, the presence of the limiter in the SOL has an impact on the plasma parameter profiles as will be shown in the next chapters.

Chapter 5

Characterization

After introducing the underlying mechanisms, the WEGA device and the diagnostics related to the work in this thesis, the following part of the thesis will present experimental results. The magnetic field is $B = 56\,\text{mT}$ with a rotational transform $\iota \approx 0.186$. The discharge is limited by the antennas of the ECR heating system at $r_{eff} = 11.4\,\text{cm}$. The standard operating scenario and its alteration due to the penetration of the biasing probe will later act as reference when assessing the impact of biasing.
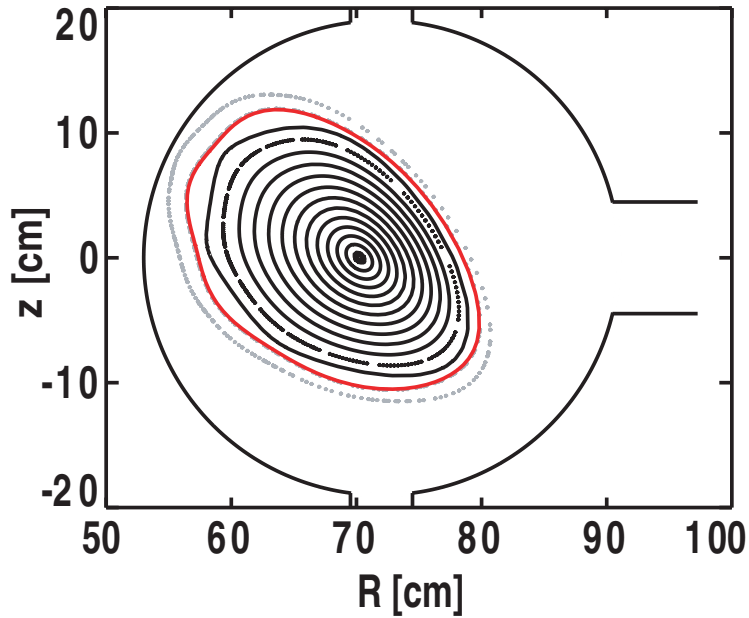

Figure 5.1: Poincaré plot of the magnetic field topology for the reference configuration at $\varphi = 144°$; LCFS is indicated red.

The shape of the magnetic field topology is shown in figure 5.1. This scenario has already been studied intensively, as the heating concept sketched in chapter 4.1.2

has been verified for this configuration. The impact of varying heating power and changing the residual gas pressure will be documented in this chapter, as well as the impact of the heating source on the plasma parameters. The parameter scans will be used to demonstrate the capability of the diagnostics to measure the parameters of interest.

5.1   Neutral Pressure Scan

The impact of a changed residual gas pressure inside the vacuum vessel is documented in the following section. Conducting measurements in stable plasma conditions requires small changes in the neutral gas flow rate, making the plasma state under observation more robust against the perturbation caused by (Langmuir) probes. The parameter scan presented here is much larger than the actual change in gas pressure required to stabilize a plasma with respect to the probe systems. It is presented here for the purpose of completeness. As there is no active neutral gas pressure control available, the gas flow rate has been varied in order to achieve a gas pressure scan. The pump rate was kept constant. The gas pressure depends linearly on the gas flow rate. The change in the residual gas pressure as a function of the gas flow rate is shown in figure 5.2.
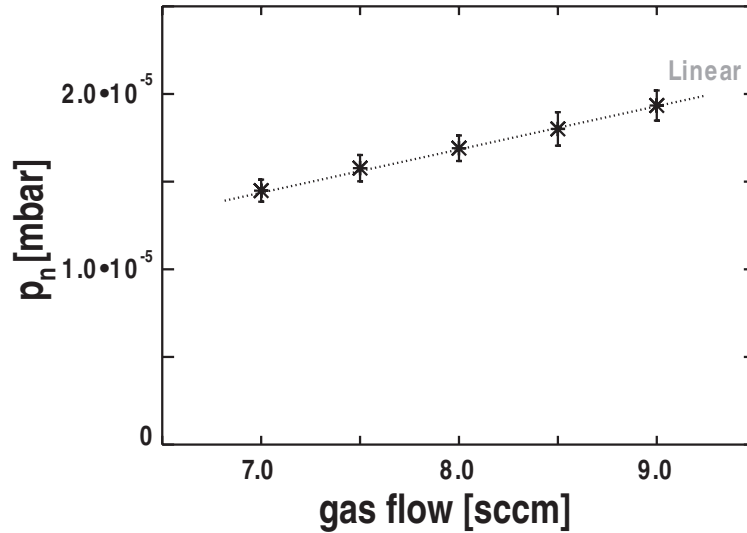

Figure 5.2: Dependence of residual gas pressure on the argon gas flow.

The impact of the gas flow rate change on the plasma parameters measured by Langmuir probes is displayed in figure 5.3. The error for the probe measurements is indicated only on the inside and the outside for purpose of better visibility.
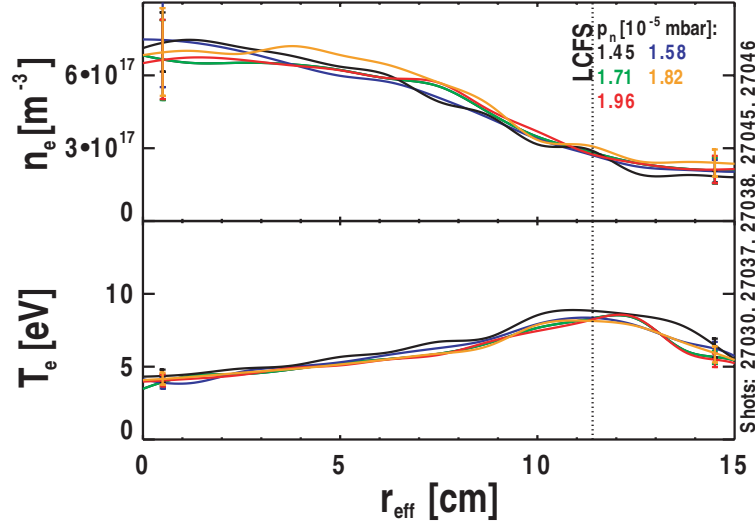
Figure 5.3: Influence of residual gas pressure variations on the plasma density and temperature.

The change of plasma parameters measured by probes is less than the typical error bars for the individual measurements. It can be concluded that a change in density and temperature induced by a change in gas pressure is small. The error bars represent a general uncertainty to the measurement. The scattering between identical discharges is typically smaller than the indicated error bars.

Measurements using the emissive probe show a decrease in the plasma potential and a small profile change in the region near the LCFS, as is shown in figure 5.4.
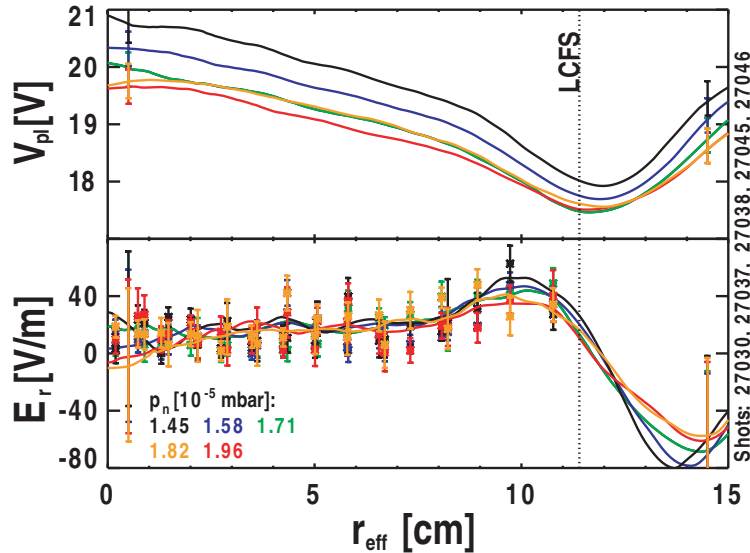

Figure 5.4: Plasma potential and radial electric field profiles from probe measurements (line) and spectroscopy (stars) for varied gas pressure; error for probe measurements is only indicated at 0.5 cm and 14.5 cm.

An increased gas pressure leads to a somewhat reduced radial electric field near the LCFS. The error for the spectroscopic measurement is mostly due to noise on the spectrum. The error of the emissive probe measurement is determined by the noise of the measurement system and does not represent the impact of the probe system to the plasma. As the temperature and density profiles are influenced only marginally by changing the gas pressure, so is the contained energy. The impact of the gas pressure scan on the confined energy is displayed in figure 5.5.
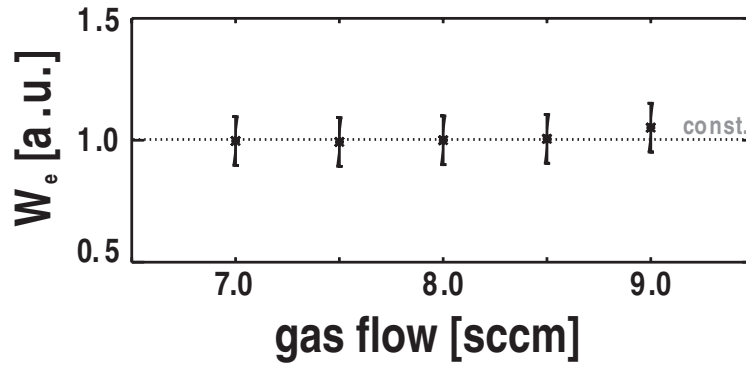

Figure 5.5:   Confined energy for varied gas flow (normalized to 8 sccm $(1.71 \cdot 10^{-5}\,\text{mbar})$ discharge; $W_e \left(1.71 \cdot 10^{-5}\,\text{mbar}\right) \approx 0.14\,\text{J})$.

Summarizing the gas scan, it can be concluded that a change in gas pressure induces small changes in the plasma profiles and the confined energy. This will be important later as a minor gas change will be required to stabilize the plasma against the perturbation caused by the probe system. That change is however small compared to the range covered here.

5.2   Microwave Power Scan

The following section will present the influence of the input heating power on the general plasma parameters. The microwave power input has been increased in steps of $\Delta P_{mw} = 1.2\,\text{kW}$ from 2.4 kW up to 6 kW for the 6 kW source and from 2.4 kW to 12 kW for the 20 kW source. For better comparison, the results obtained with the 20 kW source will be split into two sets: One containing data obtained with input power up to 6 kW and one set featuring results obtained with $P_{mw} > 6\,\text{kW}$ of input power.

5.2.1   6 kW Magnetron Source

In a first look, the line-integrated density measured by the interferometer increases with increased heating power as is shown in figure 5.6.
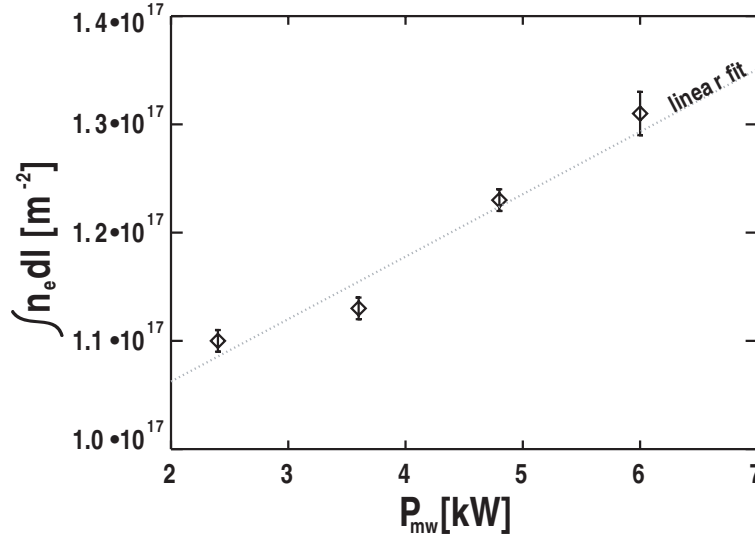

Figure 5.6: Line-integrated density for varied input ECRH power using the 6 kW cw magnetron source.

The general shape of the profiles remains similar with varied input ECRH power, but their peak values differ. Radial n_e, T_e profiles - measured with Langmuir probes - are shown in figure 5.7. The electron density profile is peaked in the center. With
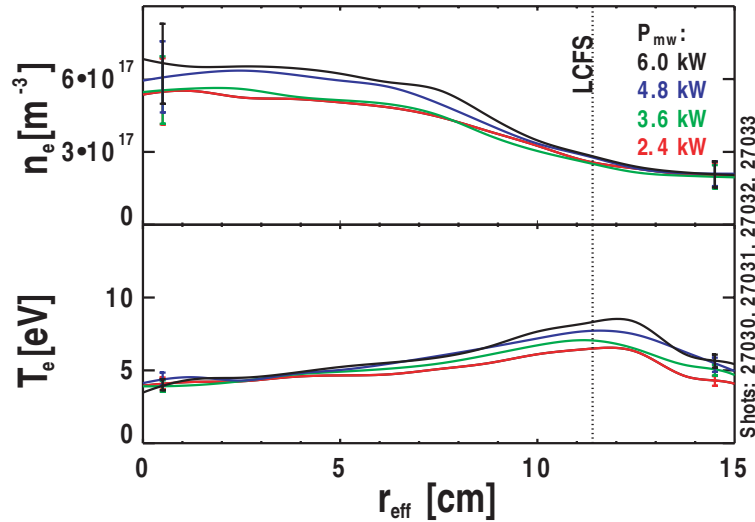

Figure 5.7: Density and temperature profiles for varied input power using the 6 kW cw magnetron source.

higher heating power, the peak density value increases slightly. Electron temperature

profiles in WEGA are typically hollow, having a maximum near the LCFS. The hollow temperature profiles originate of the hollow power deposition profile of the microwave heating explained in chapter 4.6.

An increase in heating power does not lead to a noticeable change in the spectroscopically observed poloidal rotation velocity, respectively the derived radial electric field. An impact of increasing heating power on the plasma potential profile shape has not been detectable with emissive probes, although the absolute plasma potential increases with increased heating power as can be seen in figure 5.8.
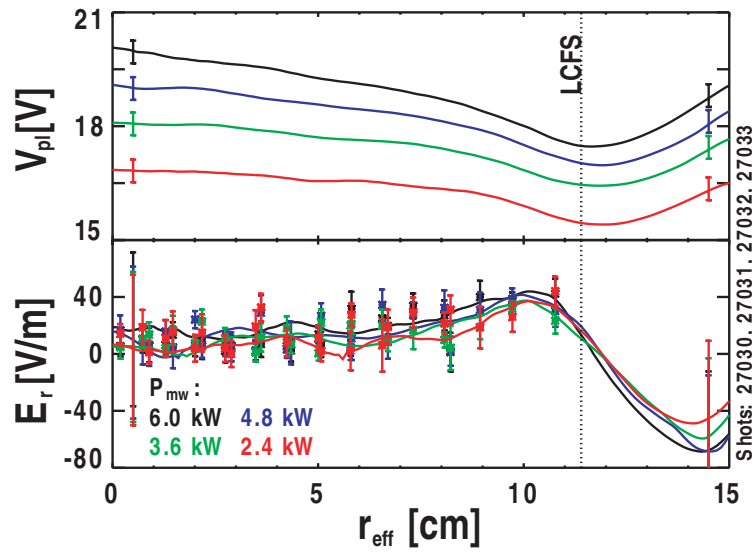

Figure 5.8: Dependence of plasma potential and radial electric field profiles on the input ECRH power using the 6 kW magnetron source from probe measurements (line) and spectroscopy (stars); error for probe measurements is only indicated at 0.5 & 14.5 cm.

The increase in the plasma potential is a consequence of the increasing electron flux to the wall, which is acting as the reference potential. The total confined energy increases linearly with the square root of the input microwave power. It is shown in figure 5.9. This phenomenon is commonly referred to as power degradation and is common to stellarators and tokamaks as has been reported in [SGH$^+$96] and references therein.

Summarizing the two scans, it can be stated that the radial electric field observed is rather small ($\approx 40\,\mathrm{V/m}$) in WEGA for low field operation up to 6 kW of input power. The radial electric field is largely independent of the neutral gas pressure as well as the used ECRH power.
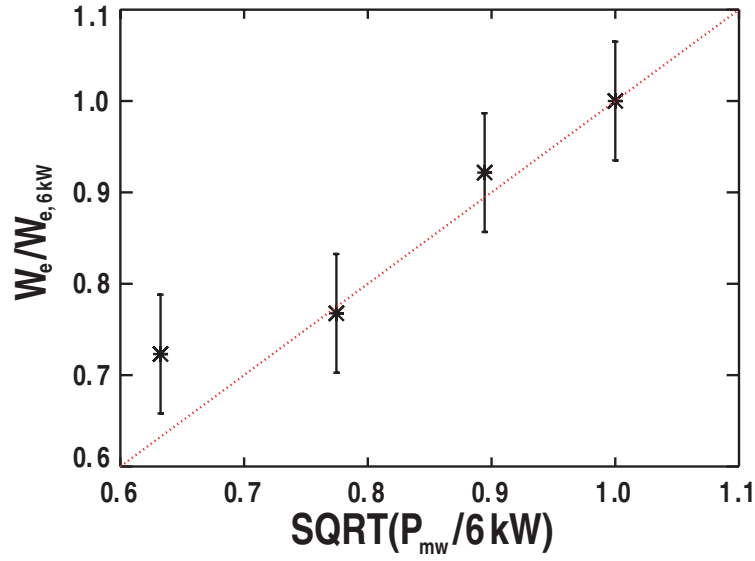
Figure 5.9: Confined plasma energy as a function of the input microwave power relative to the 6 kW discharge ($W_{e, 6\text{kW}} = 0.14$ J) using the 6 kW magnetron.

5.2.2 20 kW Magnetron Source

As the intensity of the 488 nm Ar-II line, chosen for the spectroscopic measurement, is increasing with higher plasma parameters, more microwave power improves the signal-to-noise ratio (SNR). Thus, experiments using the 20 kW magnetron have been conducted. The line-integrated density shows a linear behavior with increasing the microwave power as observed for the 6 kW source in figure 5.10.
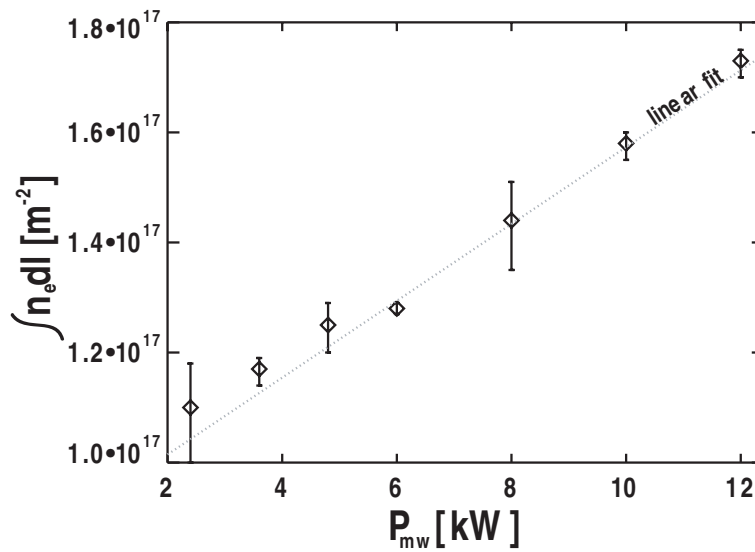

Figure 5.10: Line-integrated density for varied input ECRH power using the 20 kW cw magnetron source.

The plasma parameters increase with the applied heating power as can be seen in figure 5.11. Although the difference vanishes within the error bars, a tendency is visible. The plasma density increases with increasing heating power, as does the temperature in the edge. The plasma shows a similar behavior as with using the 6 kW source.
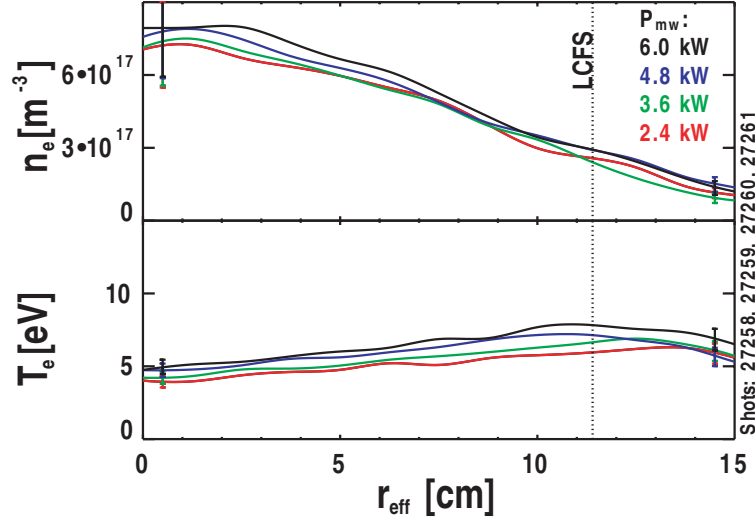

Figure 5.11: Langmuir probe measurements obtained with 20 kW magnetron source at various heating powers (2.4 - 6.0 kW).

The plasma potential profiles measured with the emissive probe are not useful for deriving the radial electric field as they are perturbed strongly as can be seen in figure 5.12.
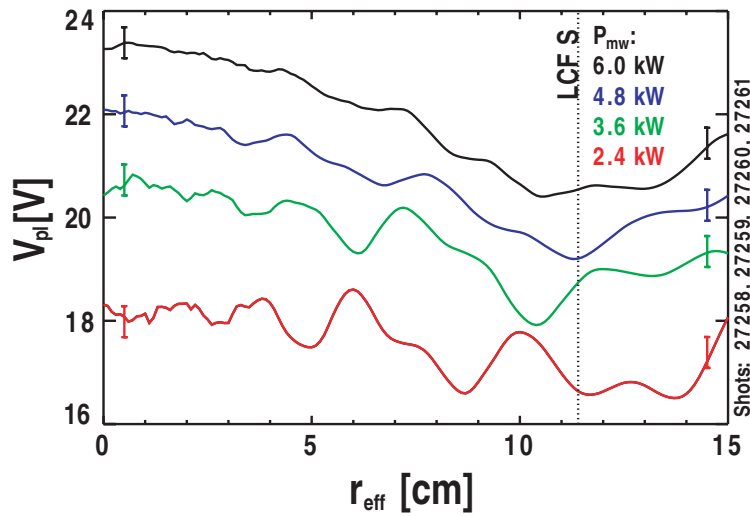

Figure 5.12: Plasma potential and derived radial electric field profiles obtained using the 20 kW magnetron source at 2.4 to 6 kW of ECR heating power.

The measurements obtained from spectroscopy suggest that the plasma is not stationary and strongly perturbed. As observed with the 6 kW source, the absolute plasma potential increases with the input power.

A further increase in heating power to obtain a better SNR for the spectroscopic measurements and also to ensure a more stable operation of the ECRH system, led to an increase of density to $n_e \approx 1.2 \cdot 10^{18}\,\mathrm{m}^{-3}$ and temperatures up to $T_e = 12\,\mathrm{eV}$. The profiles obtained for $P_{mw} \geq 6\,\mathrm{kW}$ are displayed in figure 5.13.
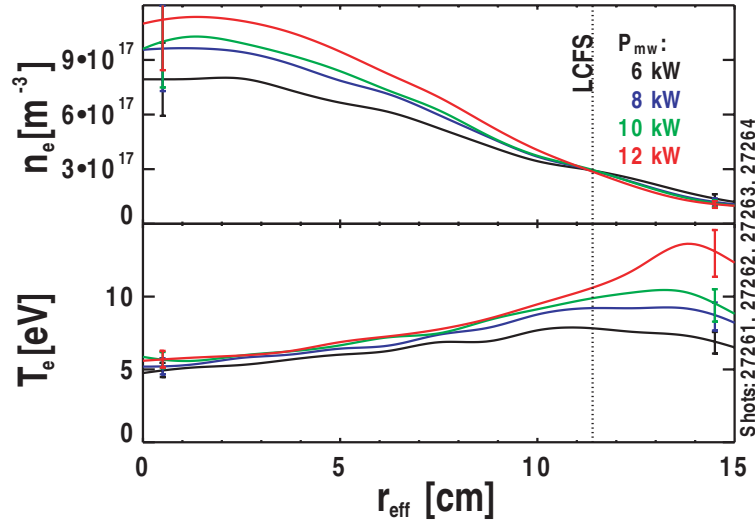

Figure 5.13: Density and temperature profiles for $P_{mw} \geq 6\,\mathrm{kW}$.

The plasma potential increases with higher heating power continuing the observed trend as is displayed in figure 5.14. The radial electric field does not change.
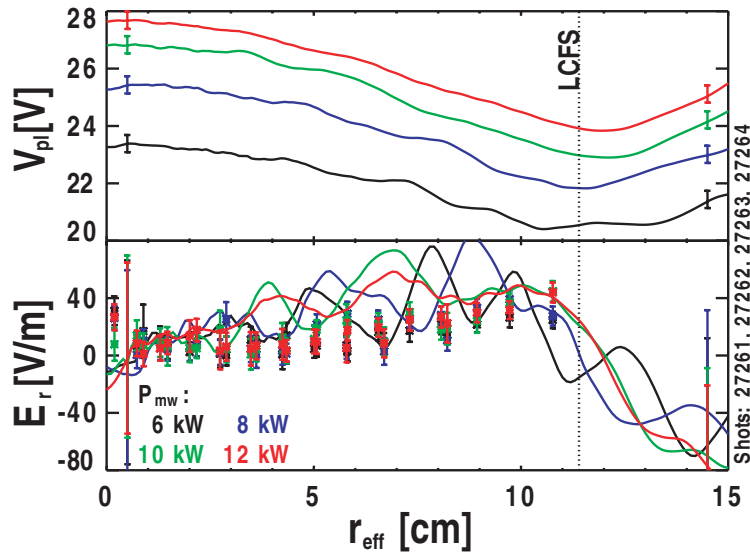

Figure 5.14: Plasma potential and radial electric field profiles for $P_{mw} \geq 6\,\mathrm{kW}$.

The plasma potential measurement becomes less perturbed with higher heating power. This behavior is typical for power microwave sources operating below the target maximum power [Laq]. The spectroscopic measurements also become reasonable for heating powers exceeding $P_{mw} = 6\,\text{kW}$, supporting this argument. The total confined energy increases with the square root of the input ECRH power as is displayed in figure 5.15.
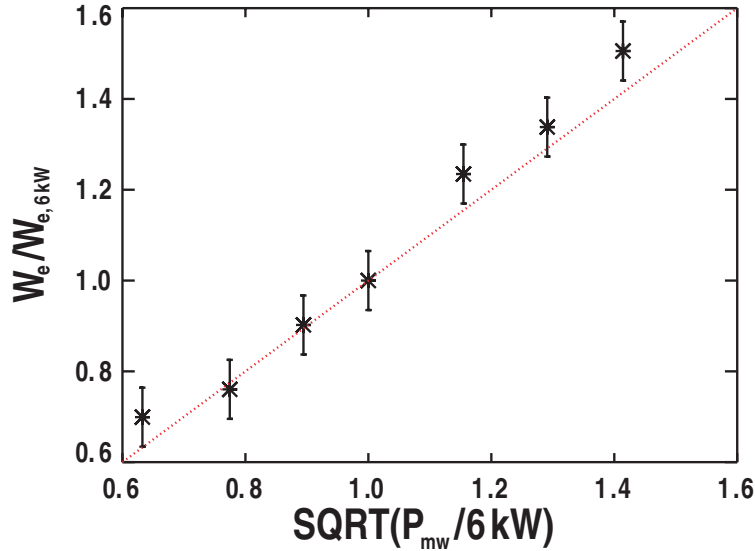

Figure 5.15: Confined plasma energy as a function of the input microwave power (20 kW magnetron) - relative to the discharge without biasing probe with 6 kW ECRH ($W_{e,6\text{kW}} = 0.14\,\text{J}$).

Due to the fact that the produced plasmas at heating powers $P_{mw} \leq 10\,\text{kW}$ are unstable, and the application with ECRH power exceeding 12 kW is very limited, the 6 kW source is chosen as heating system for further experiments. A direct comparison of the 6 kW discharge produced with the different magnetron sources can be found in appendix C.

5.3   Radial Position Scan

In order to assess the perturbation of the biasing probe its influence on the plasma has to be determined. The following section will be split into two parts describing the situation with and without the limiter installed in WEGA. The impact of the limiter needs to be discussed here, as an impact on the parameter profiles and on the behavior when biasing was found, although it is placed outside the LCFS.

5.3.1   With Limiter

First, the configuration involving the limiter will be presented. A reduction in the line-integrated density is observed when the biasing probe is inserted into the plasma. The drop of the line-integrated density with the position of the biasing probe is shown in figure 5.16.
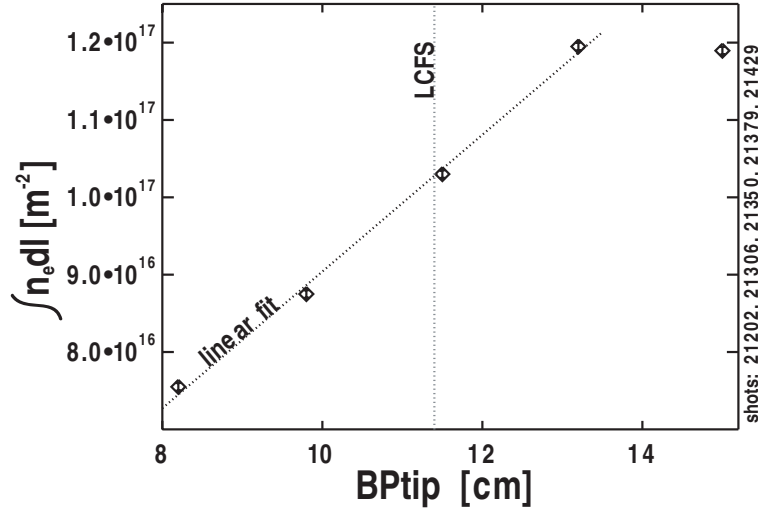
Figure 5.16: Line-integrated density obtained by interferometry for different radial biasing probe positions.

Looking at the probe profiles reveals the biasing probe affecting the electron density profile, but hardly perturbing the temperature profile (see figure 5.17).
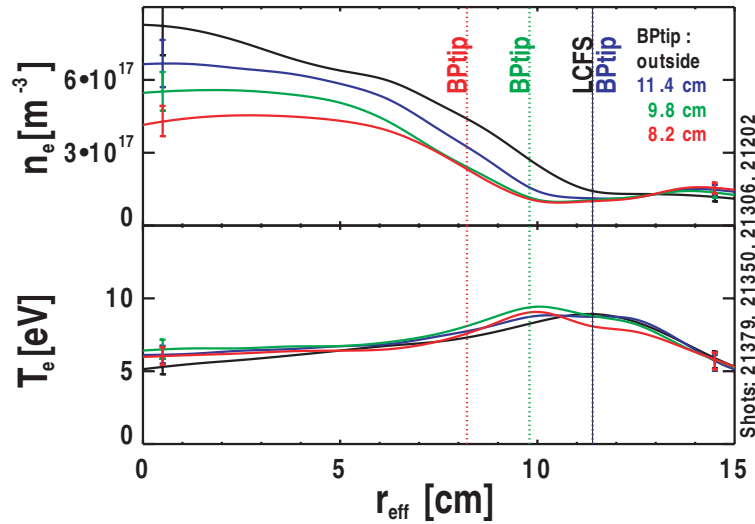
Figure 5.17: Electron density and temperature profile for different radial biasing probe positions (indicated by the dashed line) for 6 kW ECRH power.

The biasing probe shows some limiter properties as the density profile becomes

radially smaller with the introduction of the probe and its peak value is reduced. On
the other hand, the electron temperature profile remains almost unaffected. This is
attributed to the calorimetric limiter governing the properties of the SOL.

Lacking an emissive probe in the measurement campaign, the radial electric field
is derived from spectroscopic data only. The derived electric field is displayed in
figure 5.18. It can be seen that the insertion of the biasing probe to the plasma
reduces the existing radial electric field near the LCFS.
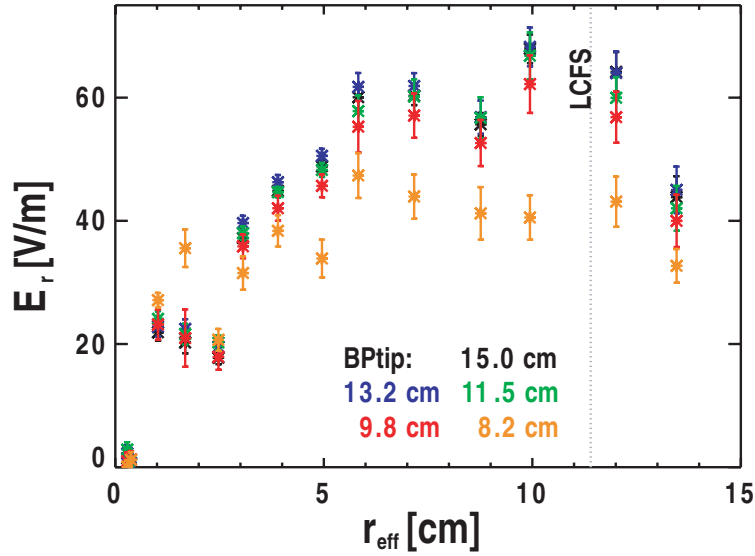
Figure 5.18: Radial electric field profile derived from UHRS for different radial
biasing probe positions.

The confined plasma energy is reduced due to the impact on the density profile.
Figure 5.19 shows the dependence of the confined plasma energy of the biasing probe
position.
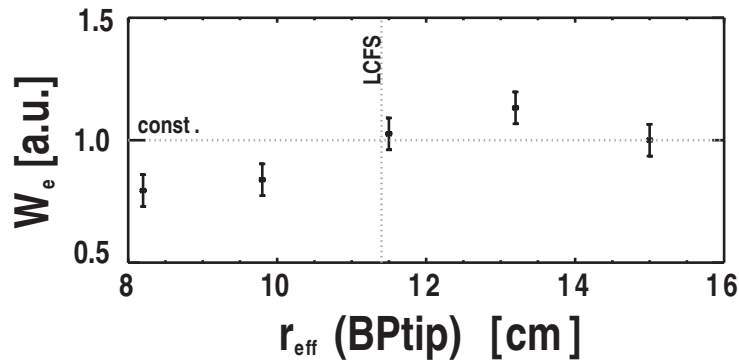
Figure 5.19: Confined plasma energy as function of radial position of the tip of the
biasing probe (BPtip) - relative to the discharge without biasing probe ($W_{e,6\mathrm{kW}} =
0.14\,\mathrm{J}$).

5.3.2 Without Limiter

In order to assess the impact of the presence of the limiter when biasing an experimental campaign, in which the limiter was removed from the vessel, has been conducted. First, the impact of the penetration of the probe is to be assessed. In a first look, the behavior of the plasma in the absence of the limiter seems similar. One notices a reduction in the line-integrated density measured by the interferometer, similar to the case with the limiter installed. The line-integrated density as a function of the biasing probe position is shown in figure 5.20.
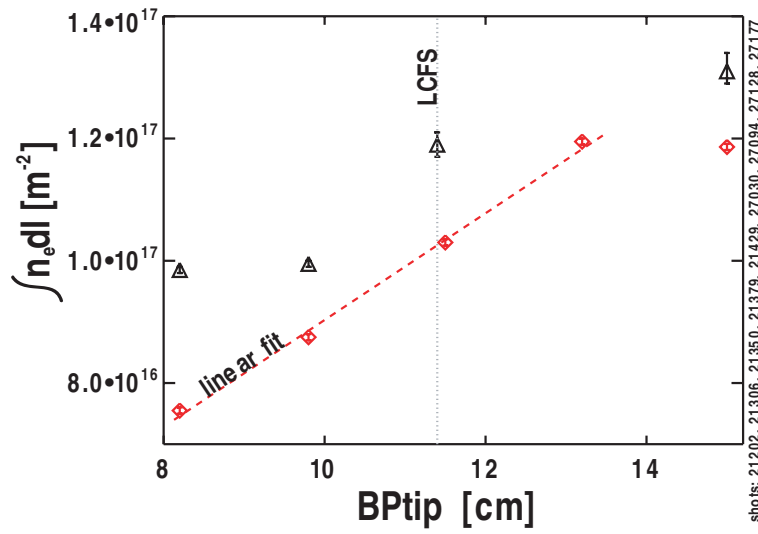
Figure 5.20: Line-integrated density for varied biasing probe position with (red) and without (black) the limiter being installed.

The tendency of acting as a limiter, concerning density profiles, can also be observed in density and temperature profiles. The impact on the profiles is not as clear as it is on the interferometer signal. The profiles nevertheless exhibit features similar to those observed with the limiter installed. The plasma density first decreases inside the LCFS (as with the limiter installed). Not observed with the limiter installed has been an increase of the peak density when the probe is inserted up to $r_{eff} = 8.2$ cm. As observed with the limiter installed, one can observe the foot of the electron density profile moving towards the center of the plasma following the movement of the biasing probe. Moving the biasing probe inwards slightly impacts the electron temperature profile as the temperature maximum moves inward, following the foot of the density profile. However, the case of the unbiased probe placed at the LCFS falls out of the pattern. This is displayed in figure 5.21.
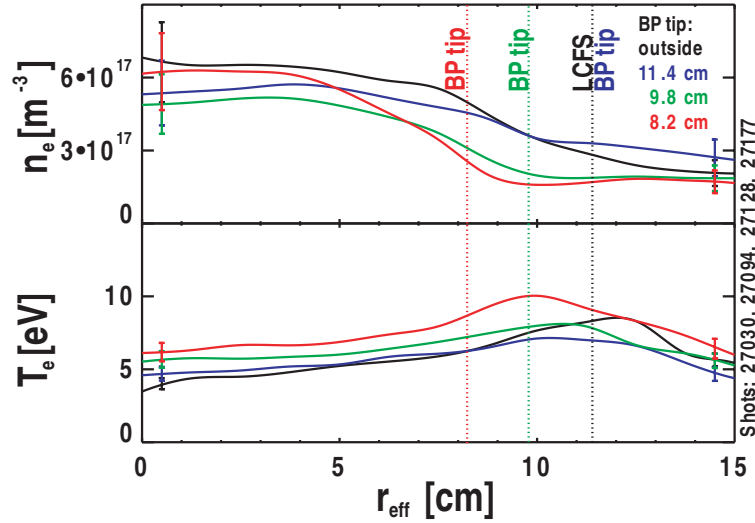
Figure 5.21: Langmuir probe results for different radial positions of the biasing probe (position is indicated by colored dashed line).

Moving the probe further into the plasma, one can see the plasma potential minimum moving outward. One can see a small plateau in front of the biasing probe tip moving with the movement of the biasing probe. The introduction of the biasing probe causes the plasma potential to increase as can be taken from figure 5.22.
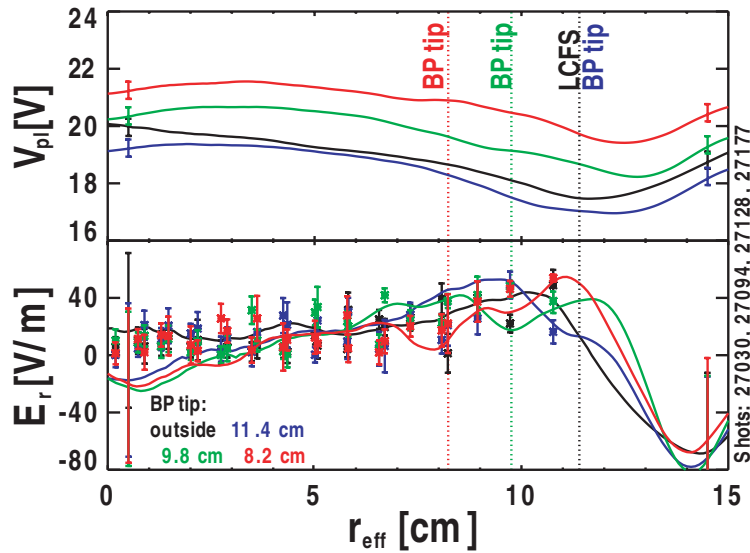
Figure 5.22: Plasma potential and radial electric field profiles obtained at different biasing probe locations from emissive probe (line) and spectroscopy (stars); biasing probe position is indicated by accordingly-colored vertical dotted line.

The potential drop from the position of the biasing probe up to the LCFS remains constant for all positions. The introduction of the unbiased probe leads to a decrease

of the radial electric field observed in front of the probe. Close to the last closed flux surface an increase of the radial electric field can be observed.

The impact of the calorimetric limiter can be summarized as follows. The calorimetric limiter dominates the SOL properties compared to the biasing probe. This is taken from the unchanged temperature profile when the limiter is installed compared to the case of a removed limiter.

Chapter 6

Biasing

This chapter will introduce results obtained with biasing argon discharges. First, the path of the biasing current will be traced for the case with and without limiter. Then, results using negative biasing with respect to the vacuum vessel will be presented. Here, negative biasing using the carbon biasing probe, as well as a large tungsten emissive biasing probe, will be presented. Finally, results obtained when biasing the carbon probe positively will be presented.

6.1   Biasing Current and Current Path

When the probe is energized inside or near the plasma, a current is drawn. The current rises exponentially with the applied voltage and then saturates as shown in figure 6.1.
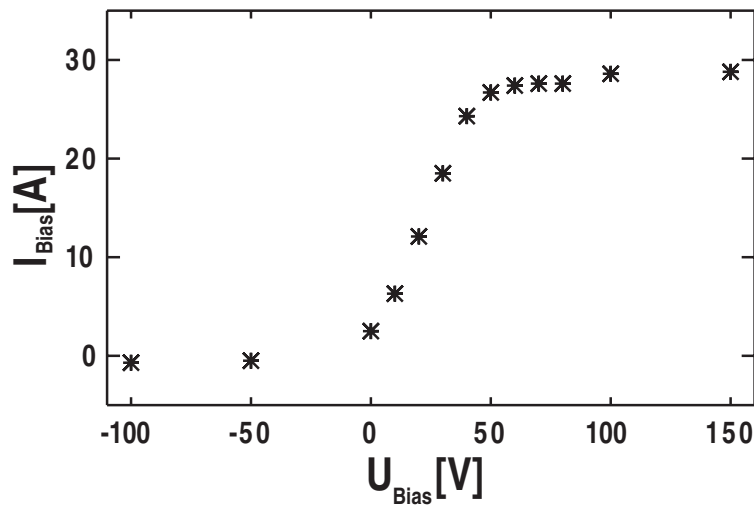
Figure 6.1: Probe characteristic of the biasing probe placed at $r_{eff} = 9.8\,\text{cm}$.

Despite the probe behaving similar to an over-sized Langmuir probe, a determination of plasma parameters from the above probe characteristic is not done as the probe is a massive perturbation to the surrounding plasma.

As introduced in chapter 4.2.3, shunt resistors can be used to trace the biasing current path. When biasing, the current distributes over both vessel modules, as can be taken from figure 6.2, for the limiter placed at $r_{eff} \sim 15\,\mathrm{cm}$.

Indicator	Current [A]
1	26.1
2	26.3
3	8.9
4	11.3
5	2.0
6	2.0
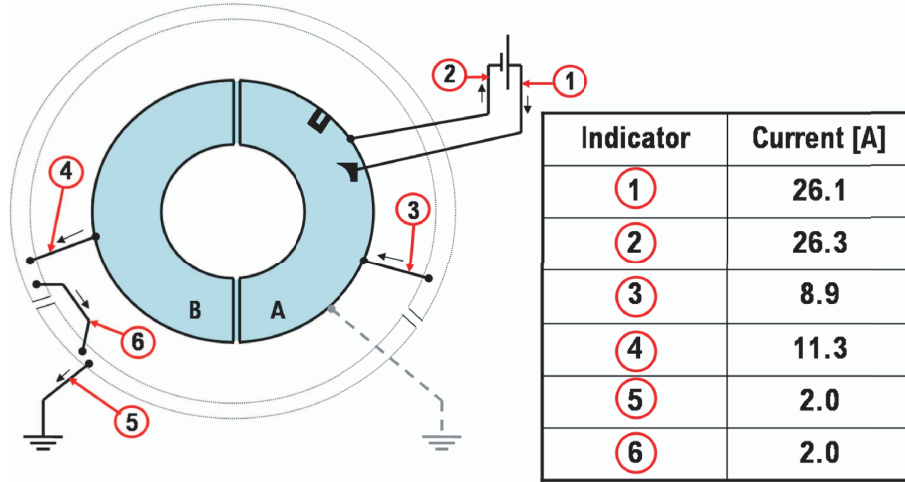
Figure 6.2: Biasing current path measured by current clamps at the shunt position with calorimetric limiter in the far SOL (for $U_{Bias} = +70\,\mathrm{V}$).

Using current clamps for the measurement, the current flowing from the plasma on vessel half A can be calculated to $I_{pl \to A} \sim 14.9 \pm 0.15\,\mathrm{A}$.

Indicator	Current [A]
1	26.2
2	26.4
3	13.1
4	13.3
5	0.2
6	0.2
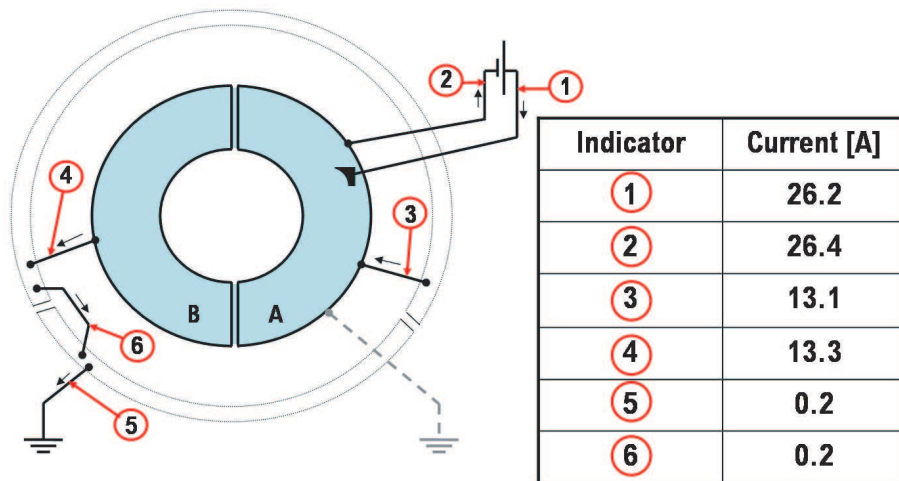
Figure 6.3: Current path during biasing without the calorimetric limiter being installed (for $U_{bias} = +70\,\mathrm{V}$); measurement has been conducted with current clamps at the position of the shunt resistors.

The current on the half torus A is about 30 % larger than the current on vessel module B with the limiter installed. This changes when the limiter is removed as can be taken from figure 6.3.

The biasing current now distributes almost evenly over both halves of the vacuum vessel. It is concluded that the limiter has a partial connection to the biasing probe. Also, the amount of current flowing via parasitic ground connections has been minimized in the mean time.

6.2 Negative Biasing

In order to keep the power load to the probe small, negative biasing has been performed. Negative biasing has been conducted in two different approaches: Negative biasing of the carbon probe and emissive biasing using a large tungsten emissive probe. The results obtained will be presented in the following.

6.2.1 Carbon Probe

With negatively biasing the carbon probe, the current is limited to the ion saturation current flowing to the probe. Figure 6.4 shows the temporal evolution of a negatively biased discharge in low field operation.
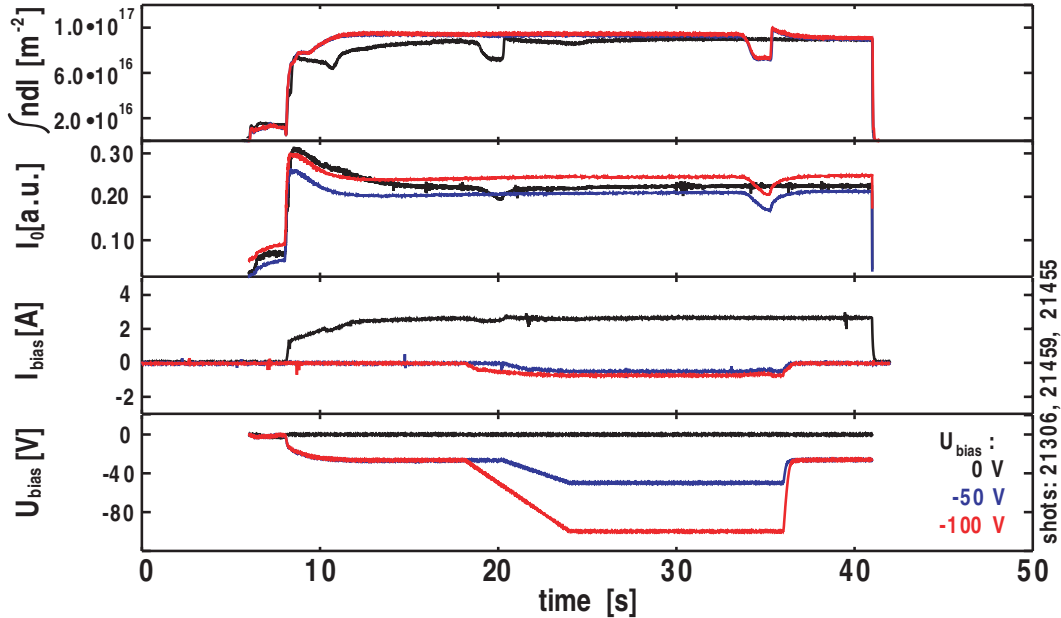
Figure 6.4: Time traces of negatively biased discharges and the reference discharge; biasing probe is placed at $r_{eff} = 9.8$ cm; dips in curves after $t = 18$ s (black) and after $t = 33$ s (red & blue) correspond to probe measurements.

As the current is small, the impact on the plasma parameter profiles is expected to be small as well. As shown in figure 6.5, the central density increases slightly. The change is of similar size as the error bars. An impact on the temperature profile is not noticeable at all.
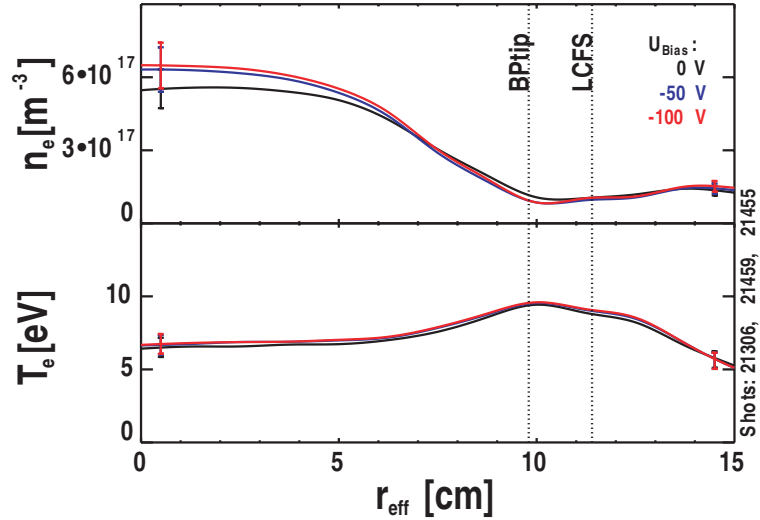
Figure 6.5: Density and temperature profiles of negatively biased discharges using the carbon biasing probe placed at $r_{eff} = 9.8\,\text{cm}$.

The spectroscopic measurements also do not indicate a change in the radial electric field, as is shown in figure 6.6.
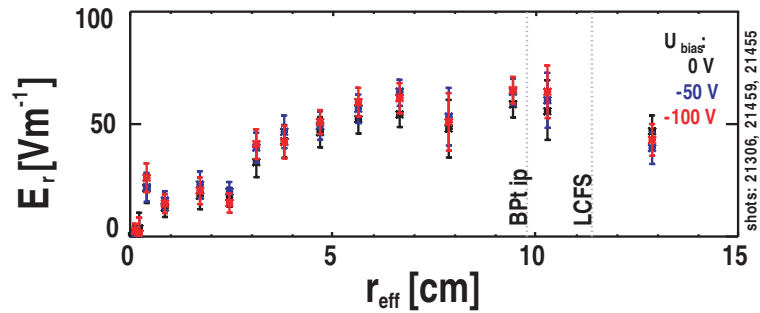
Figure 6.6: Radial electric field profile of negatively biased discharges using the carbon biasing probe placed at $r_{eff} = 9.8\,\text{cm}$.

Negative biasing using carbon probes does not have a measurable impact on the radial electric field or on other plasma parameter profiles. This is attributed to the small biasing current which is not able to significantly change the particle and energy fluxes.

6.2.2 Tungsten Emissive Probe

In order to overcome the absolute current limit of the carbon probes with negative biasing, a large emissive probe has been constructed as explained in chapter 4.4.2. Due to the high wear of the emissive biasing probe, when heated and exposed to the magnetic field, its lifetime is very limited. The discharge is slightly modified compared to the standard biasing discharges as the emissive probe needs time to heat up. This has to be done in the constant magnetic field as the stress which is otherwise applied, leads to the destruction of the probe. Especially, the ignition of the plasma leads to a destruction of the probe when already heated. The probe is very fragile compared to abrupt plasma termination as has often been encountered during biasing experiments.The evolution of a typical negatively biased discharge using the large emissive biasing probe is displayed in figure 6.7.
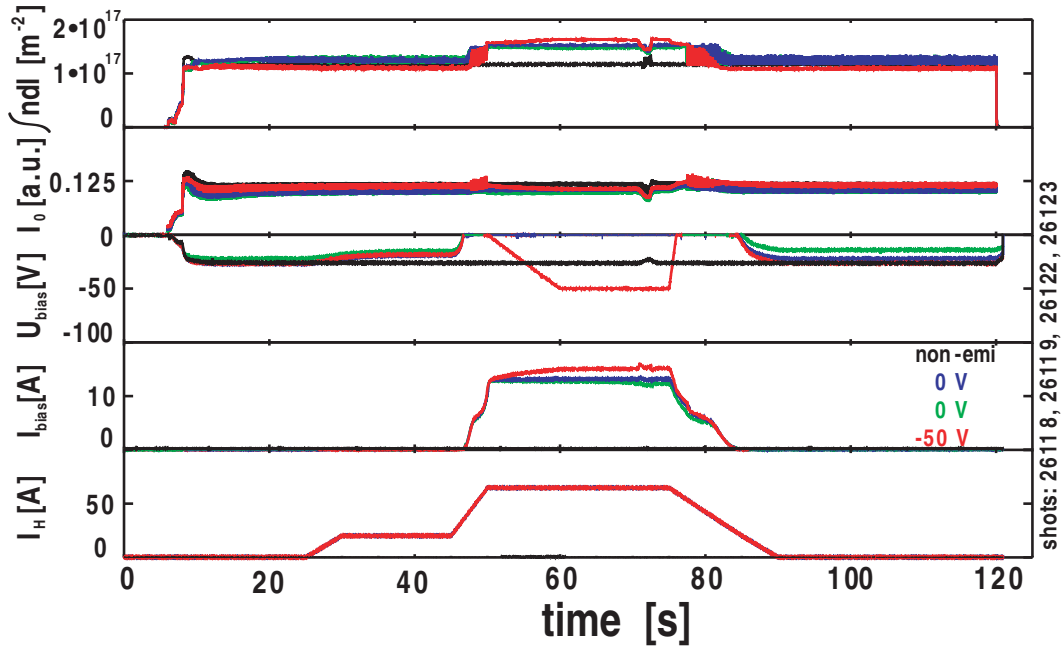
Figure 6.7: Time traces of different quantities of discharges employing the non-emissive (black), unbiased emissive (blue, green) and negatively biased emissive (red) tungsten biasing probe placed at $r_{eff} = 10.6$ cm; dips in curves after $t = 70$ s correspond to probe measurements.

The line-integrated density increases when employing the biasing probe in emissive fashion compared to non-emissive use. A change involving biasing is hardly noticeable. Aside from the aspect of emission impacting the density and temperature profiles, biasing negatively with significant current does not have much impact on the density and temperature profiles, as is shown in figure 6.8.
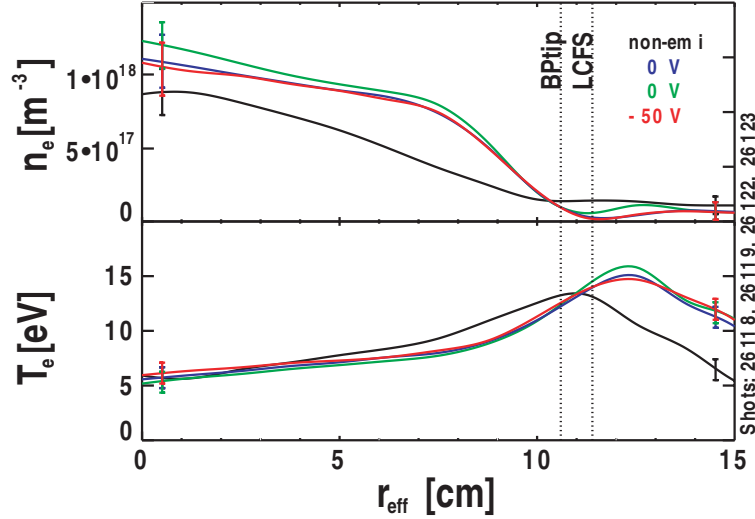
Figure 6.8: Density and temperature profiles of non-emissive (black), emissive, but unbiased (blue, green) and emissive and negatively biased (red) discharges using the tungsten emissive biasing probe placed at $r_{eff} = 10.6$ cm.

Spectroscopic measurements between the probe tip and the LCFS show that operating the tungsten probe in emission changes the radial electric field from less than $40 \frac{V}{m}$ to about $50 \frac{V}{m}$. Additional biasing of the emissive probe does not lead to significant changes in the radial electric field as can be seen in figure 6.9.
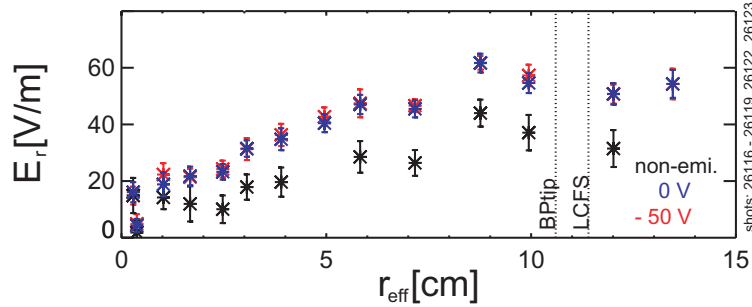
Figure 6.9: Poloidal velocity and derived radial electric field of negatively biased discharges using the emissive biasing probe placed at $r_{eff} = 10.6$ cm.

In conclusion, also negative emissive biasing does not allow controlling the radial electric field. With negative biasing not being able to produce effects that can be related to biasing, positive biasing is the only option to draw significant current to the biasing probe. As the emissive tungsten biasing probe is too fragile positive biasing is conducted using the carbon biasing probes only.

6.3 Positive Biasing

After not invoking noticeable changes by negative biasing, results obtained with positive biasing, with respect to the vacuum vessel, will now be presented. As the limiter is crucial in biasing, this section is divided into two parts: One dealing with biasing the plasma in the presence of the limiter in the SOL and one without the limiter installed on WEGA.

6.3.1 Limiter Installed

First, results from biasing the reference discharge in the presence of the limiter placed in the SOL will be presented. The emissive probe for plasma potential profile measurements was not available during this campaign. The radial electric field is derived from spectroscopy. As chapter 5 has shown, measurements with emissive probes and spectroscopic measurements yield equivalent results.

Time traces of biased discharges in combination with the biasing current and voltage are displayed in figure 6.10.
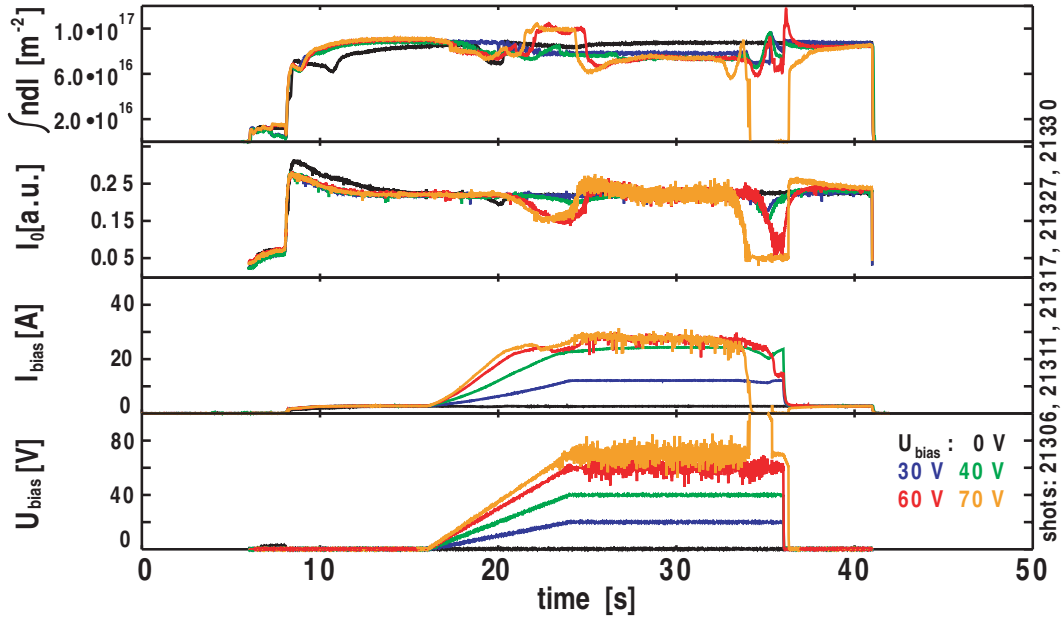
Figure 6.10: Time traces of line-integrated density, neutral line emission and biasing parameters for varied biasing voltage for a discharge with limiter in the SOL; dips in curves after $t = 34\,\mathrm{s}$ (all, but orange) and after $t = 32\,\mathrm{s}$ (orange) correspond to probe measurements.

Figure 6.11 shows the dependence of the interferometer signal and biasing current for the respective biased phases. When biasing the plasma the line-integrated density

drops with the biasing voltage and the effect saturates as the biasing current does. The biasing current increases with an increase in the biasing voltage and saturates above $U_{Bias} > +50\,\text{V}$.
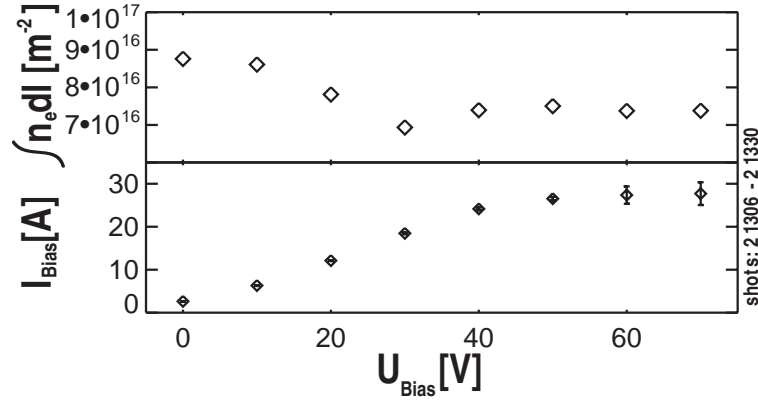
Figure 6.11: Line-integrated density and biasing current during the biased part of the discharges versus biasing voltage.

The density profile shows a decrease in the edge density with the foot of the density profile moving inwards. The peak temperature increases with biasing, but the effect saturates above $U_{Bias} > +50\,\text{V}$, as can be seen in figure 6.12.
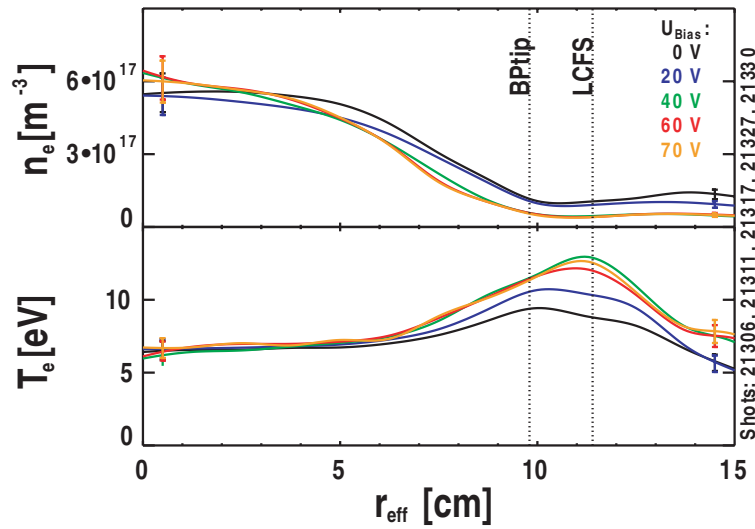
Figure 6.12: Electron density and temperature for biasing voltages $U_{Bias} < +70\,\text{V}$, biasing probe tip is indicated by dashed line for 6 kW ECRH power.

The functional dependence of the central plasma density and temperature on biasing parameters is shown in figure 6.13. The drawn current remains almost constant for biasing voltages $U_{Bias} > +50\,\text{V}$.
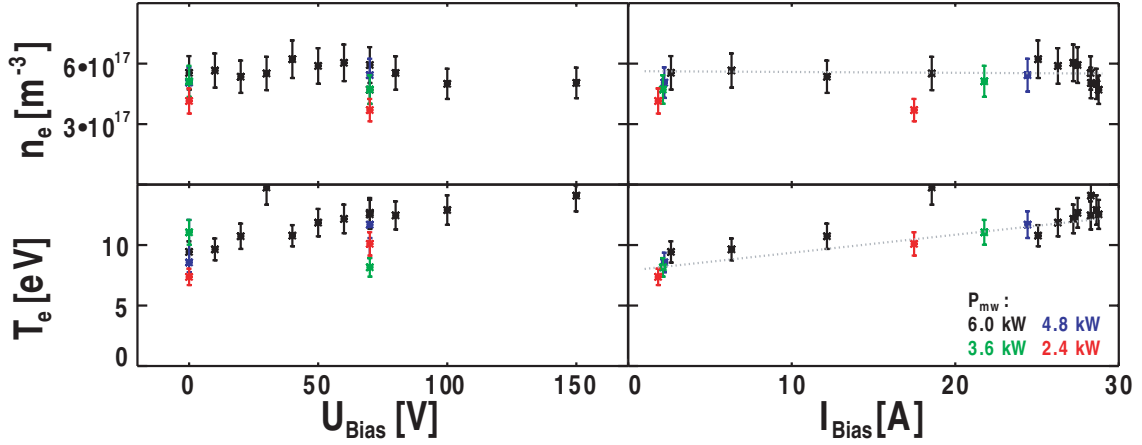
Figure 6.13: Dependence of the central plasma density and temperature maximum on biasing voltage and current.

The electric field increases with biasing as long as the drawn current is increasing as well. The values shown in figure 6.15 represent the radial electric field in front of the biasing probe. Radial electric field profiles, derived from spectroscopy, are displayed in figure 6.14 for the voltage range between $0\,\text{V} \leq U_{Bias} \leq +60\,\text{V}$.
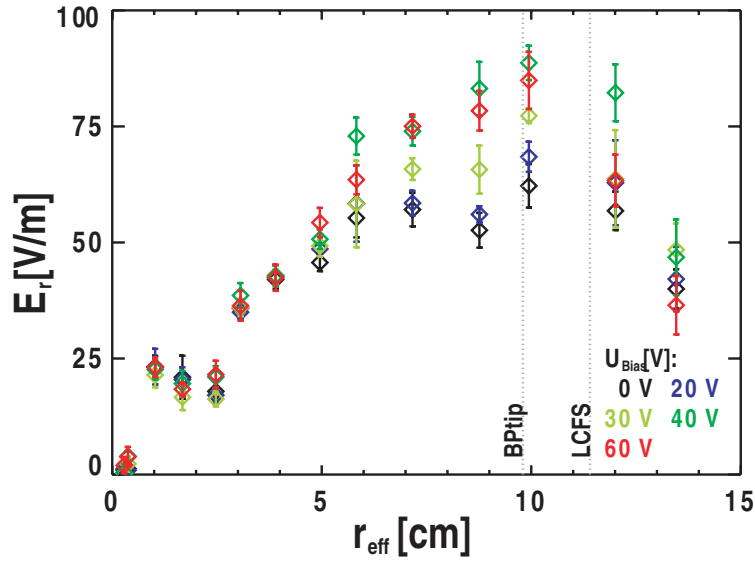
Figure 6.14: Radial electric field profiles, derived from poloidal rotation, for biasing voltages between 0 and +60 V.

In order to give a better view of the data, the points are reduced to the value near the biasing probe tip. As can be seen in figure 6.15, the radial electric field is proportional to the drawn biasing current.
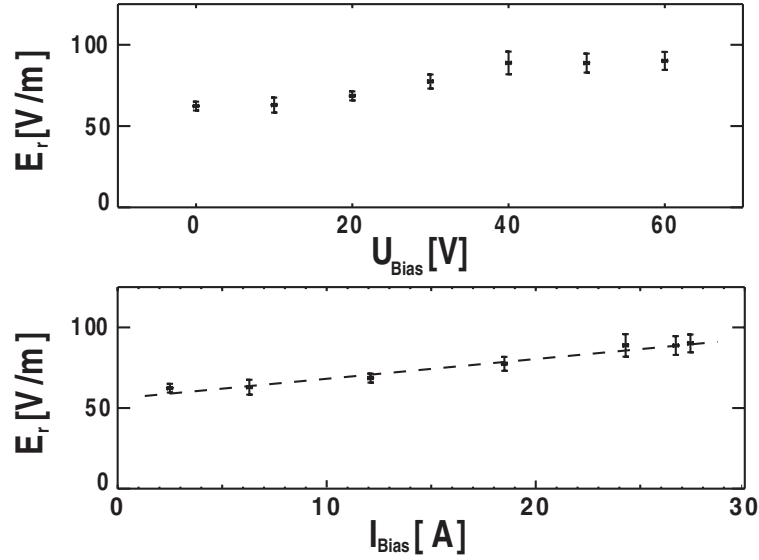
Figure 6.15: Radial electric field in front of the biasing probe as a function of the biasing voltage (current), biasing probe placed at $r_{eff} = 9.8\,\text{cm}$ (shots: 21200+).

Employing biasing with voltages exceeding $U_{Bias} = +60\,\text{V}$, the plasma in the biased phase exhibited transitional behavior. Figure 6.16 shows time traces of discharges biased with $U_{Bias} = +70\,\text{V}$ and $U_{Bias} = +80\,\text{V}$.
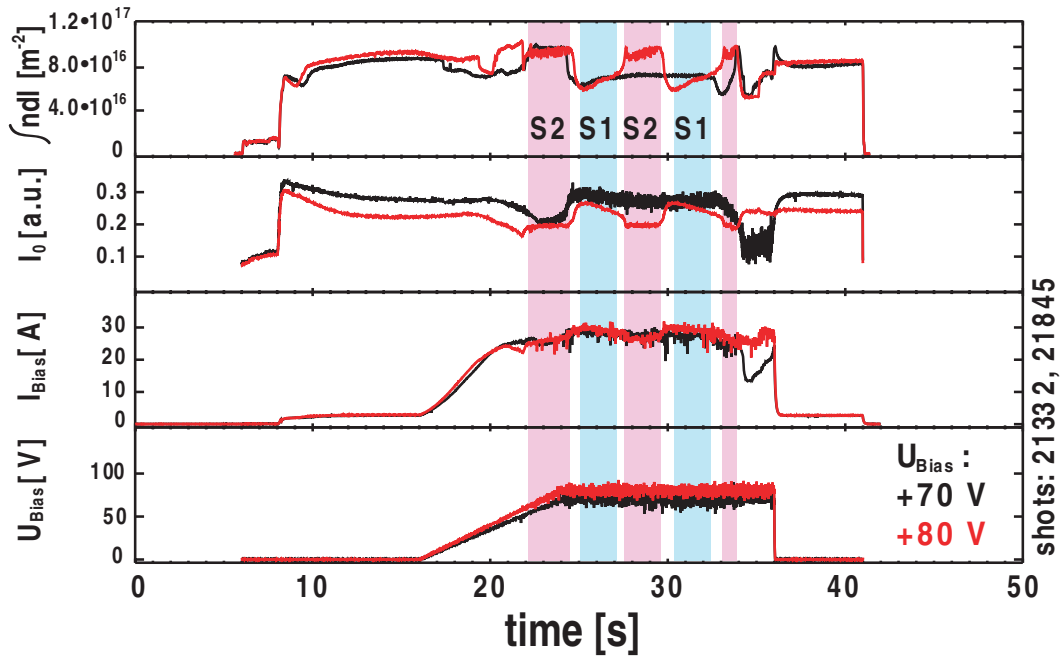
Figure 6.16: Time traces for a 6 kW discharge biased with $U_{Bias} = +70\,\text{V}$ (black) and $U_{Bias} = +80\,\text{V}$ (red) with biasing probe is placed at $r_{eff} = 9.8\,\text{cm}$; dips in curves after $t = 34\,\text{s}$ correspond to probe measurements; the different plasma states obtained with $U_{Bias} = +80\,\text{V}$ are highlighted blue (low-n_e-T_e state) and magenta (high-n_e-T_e state)

Here, the plasma starts to undergo spontaneous transitions between the known state (low-n_e-T_e state) and one exhibiting a higher line-integrated density on the interferometer (high-n_e-T_e state) living longer than the particle confinement time of $\tau_P \approx 1\,\text{ms}$ [Pod].
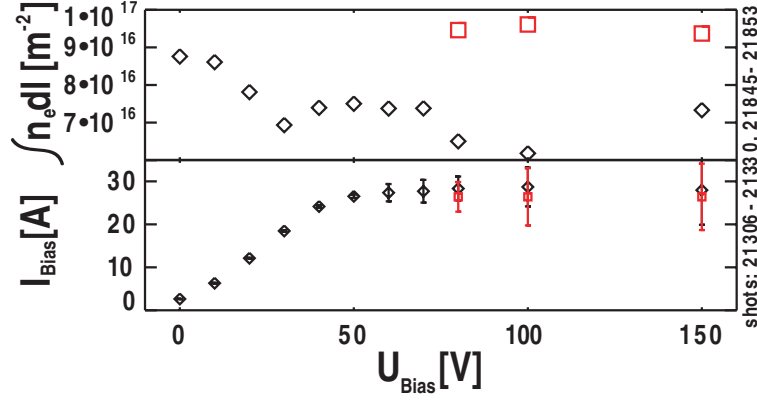
Figure 6.17: Line-integrated density and biasing current versus biasing voltage for $0\,\text{V} < U_{Bias} < +150\,\text{V}$ (black - low-n_e-T_e state, red - high-n_e-T_e state).

The transition between the two states can be seen during the stationary biasing phase. It has been found, that the current is reduced while the line-integrated density is increased in the high-n_e-T_e state, as can be seen in figure 6.17, during the constant biasing phase of discharges in which transitions to the high-n_e-T_e state occurred.
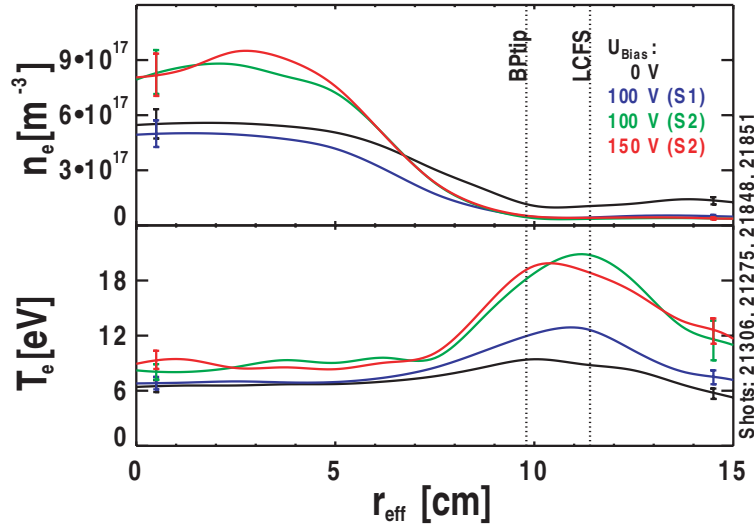
Figure 6.18: Electron density and temperature profiles for biasing voltage exceeding $U_{Bias} > +70\,\text{V}$ for both states, biasing probe tip and LCFS are indicated by dashed line for 6 kW ECRH power.

The results of Langmuir probe measurements are shown in figure 6.18. The difference in the density profiles in the center is well outside the error bars. The density in the high n_e-T_e state remains constant within the error bars with further increasing the biasing power. This is also supported by the interferometer. As the probe system is presently the only density profile diagnostic, it is not guaranteed that the density profiles really turn hollow in the center as is suggested by the probe measurements. The hollow profile could also result from the perturbation of the plasma due to the probe system. This should be verified by additional density profile diagnostics. The electron temperature increases significantly with the transition to the high-n_e-T_e state. Here, it remains unaffected by a further increase in biasing voltage. Electron temperatures exceeding $T_e = 20\,\mathrm{eV}$ have been achieved for the first time with argon in low field operation. A difference in the two states was also observed in the radial electric field as is shown in figure 6.19.
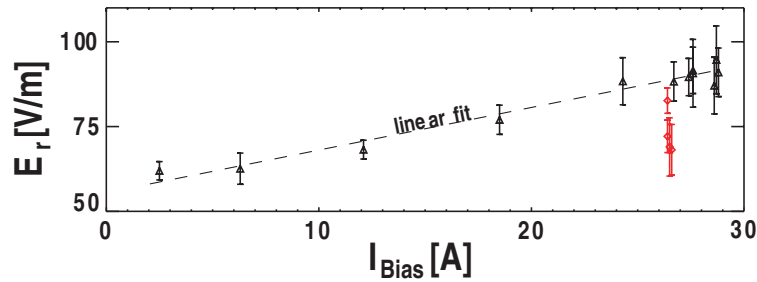
Figure 6.19: Radial electric field in front of the biasing probe for $I_{Bias} < +30\,\mathrm{A}$; first state (black), second state (red).

The high-n_e-T_e state shows a lower radial electric field than the low-n_e-T_e state. As the radial electric field was found to depend linear on the biasing current, it is reasonable that the plasma in the high-n_e-T_e state shows a smaller radial electric field, as the current is also reduced compared to the low-n_e-T_e state. The radial electric field in the high-n_e-T_e state is much less than the radial electric field of a plasma in the low-n_e-T_e state with equivalent current though. This can be seen in figure 6.19. The points for the high-n_e-T_e state are systematically underneath the linear regression curve of the radial electric field for the low-n_e-T_e state.

The stored energy in the second state is significantly higher than in the first state, as can be seen in figure 6.20. This is due to the fact that the plasma density in the center is larger, as is the electron temperature in the edge. The improvement of the high-n_e-T_e state is about a factor of 2 compared to the low-n_e-T_e state with the same biasing voltage. Compared to the unbiased case the increase is about 40 %.
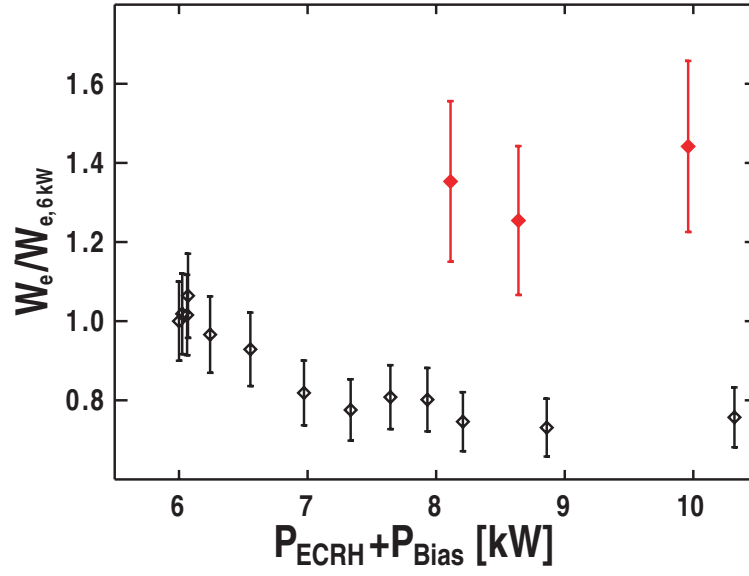
Figure 6.20: Stored energy for both plasma states as function of the total input power; low-n_e-T_e state (black), high-n_e-T_e state (red); $W_{e,6\mathrm{kW}} = 0.14\,\mathrm{J}$.

6.3.2 Limiter Removed

In this section results obtained with biasing the plasma without the presence of the limiter will be presented. Time traces of typical biased discharges are shown in figure 6.21.
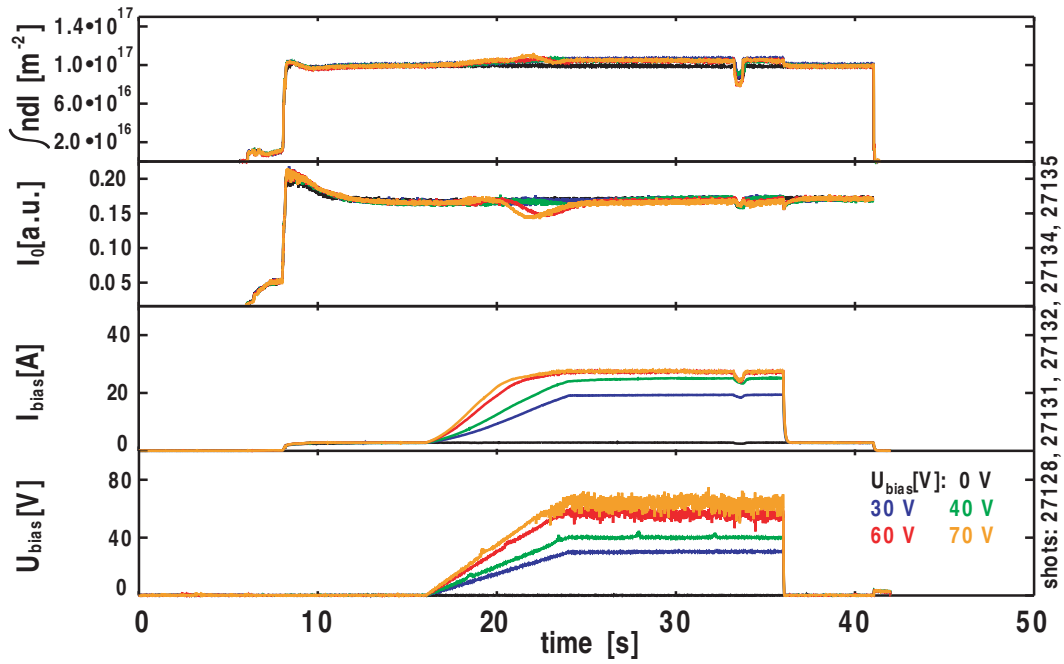
Figure 6.21: Time traces of 6 kW argon discharges without limiter installed on WEGA biased for varied biasing voltages; biasing probe at $r_{eff} = 9.8$ cm; dips after $t = 32$ s correspond to probe measurements.

When biasing the plasma without the presence of the limiter, an increase of the line-integrated density when biasing is observed. The change is small looking at the interferometer data and compared to the discharges with the limiter in the opposite direction, as the line-integrated density increases slightly. The effect becomes more vivid when looking at the plasma parameter profiles in figure 6.22.

Comparing the results to those obtained with limiter installed, the density in the center is increasing with biasing with respect to the reference discharge. The density in the edge does not decrease as much as is the case with limiter installed. Common to both scenarios is the increase of the temperature maximum in the edge. Figure 6.23 shows the functional dependence of the electron temperature maximum and center density versus the biasing parameters.
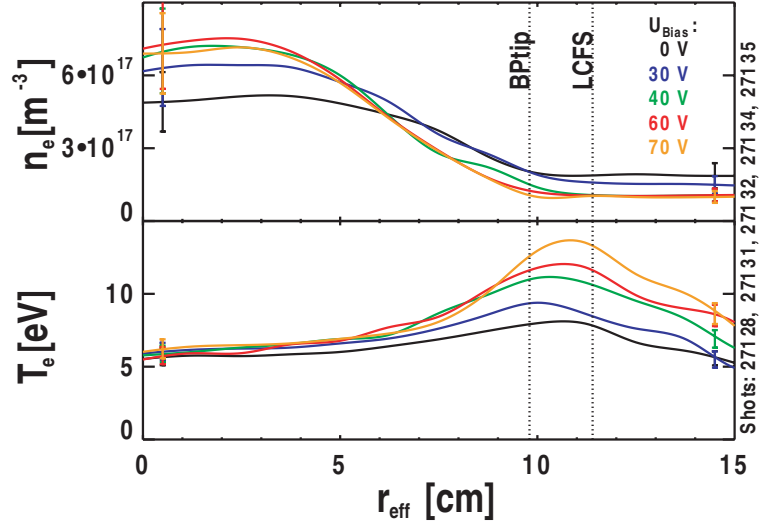
Figure 6.22: Density and temperature profiles of discharges without the limiter for different biasing voltages (Biasing probe placed at $r_{eff} = 9.8\,\text{cm}$).

The observed maximum temperature increases with the biasing current, as does the density. Comparing the density behavior with biasing current for both limiter cases the difference can easily be seen.
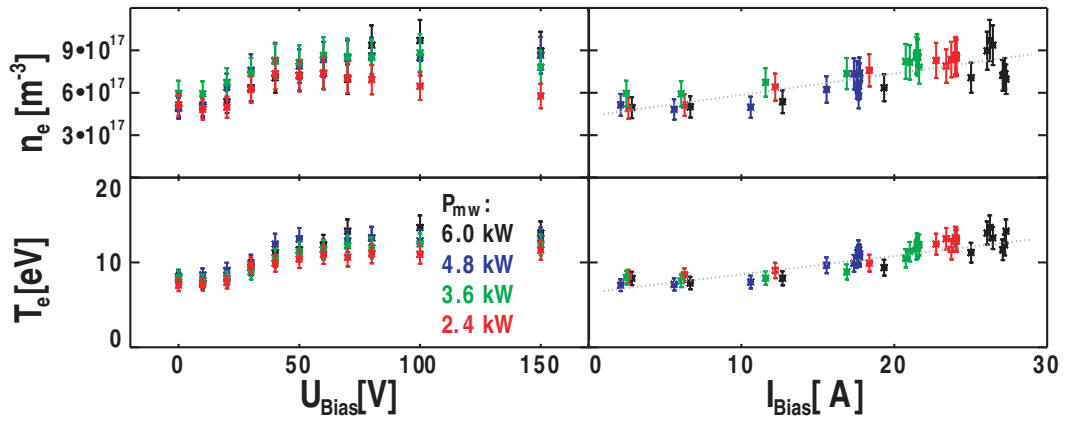
Figure 6.23: Functional dependence of electron temperature maximum and central density on biasing voltage and biasing current (biasing probe placed at $r_{eff} = 9.8\,\text{cm}$; shots 27000+).

The plasma potential increases as observed with in the other cases. An increase of the radial electric field with biasing has been observed as well, as can be seen in figure 6.24. The radial electric field can be increased from $E_r \approx 40\,\frac{\text{V}}{\text{m}}$ to $\approx 120\,\frac{\text{V}}{\text{m}}$ in between the biasing probe tip and the last closed flux surface.
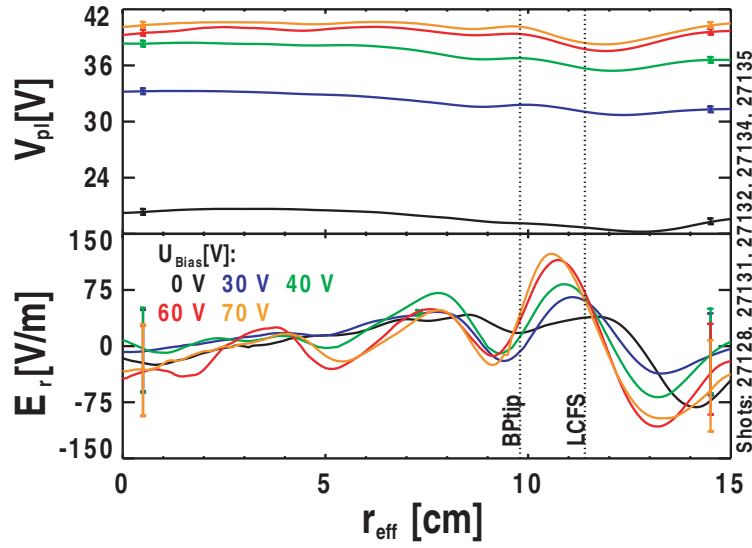
Figure 6.24: Plasma potential and derived radial electric field profiles for biasing voltages $U_{Bias} < +70\,\mathrm{V}$ without the limiter being installed.

The plasma when biasing without the limiter installed is in the second state from the beginning. This can be shown by destabilizing the biased plasma state, for instance by reducing heating power as is shown in figure 6.25.
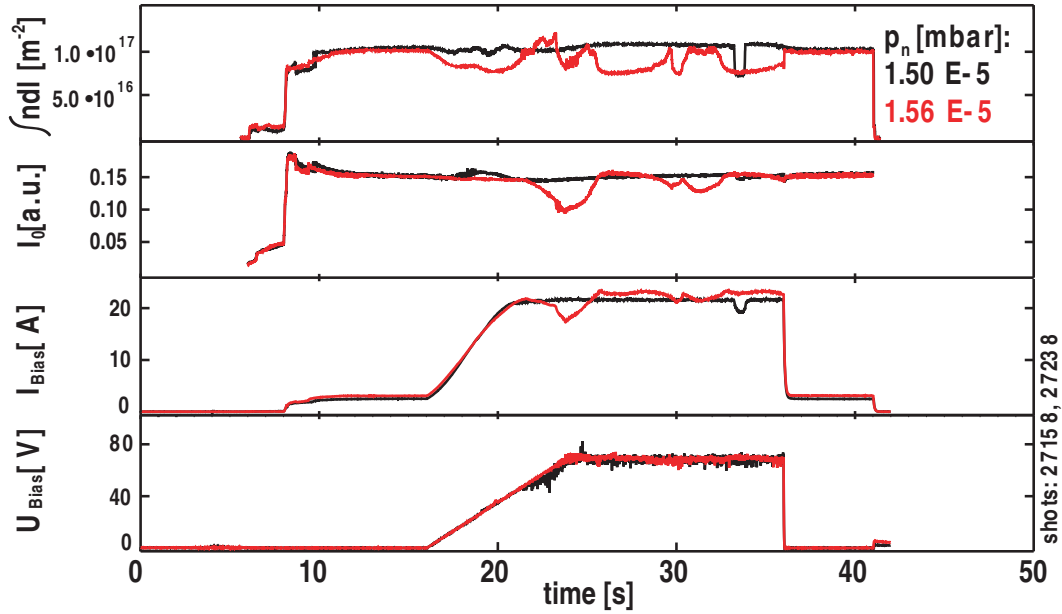
Figure 6.25: Time traces of 3.6 kW argon discharges without limiter installed on WEGA biased with $U_{Bias} = +70\,\mathrm{V}$ with biasing probe placed at $r_{eff} = 9.8\,\mathrm{cm}$; dips in curves after $t = 32\,\mathrm{s}$ (black) and after $t = 30\,\mathrm{s}$ (red) correspond to probe measurements.

Figure 6.25 shows time traces of two discharges heated with 3.6 kW ECRH power and biased to $U_{Bias} = +70\,\mathrm{V}$ in the absence of the calorimetric limiter. As can be

seen, it is possible for producing plasmas remaining in the high-n_e-T_e state only and - with slightly increased gas pressure - to produce discharges in which both states occur.

It has not been possible to destabilize the plasma in case of the 6 kW discharge, while maintaining safe machine operation, by other means. Either the plasma terminated or turned unstable, causing large mechanical oscillations of the biasing probe.

6.4   Overview

Combining the above results with measurements at intermediate biasing voltages, the biasing campaign involving 6 kW of ECRH input power can be summarized. As the first goal, the demonstration of the modification of the radial electric has been demonstrated. Combining the results from different biasing probe geometries, as well as different biasing campaigns, in figure 6.26 shows that using biasing one is able to control the radial electric field at the LCFS in WEGA argon discharges. It has been found that the presence of the limiter, placed in the far SOL, is not critical for determining the radial electric field near the LCFS, although its presence in the machine has an impact on the plasma parameter profiles.
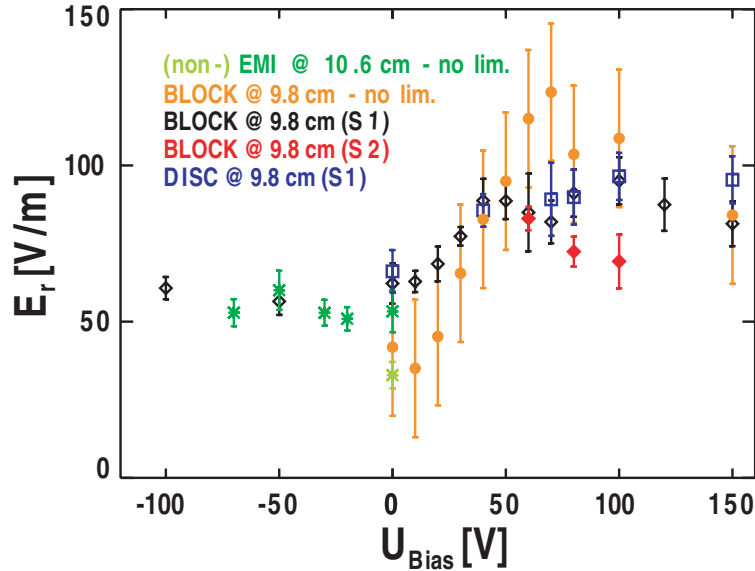
Figure 6.26: Overview of radial electric field near the biasing probe tip for different biasing voltages of carbon biasing probes at $r_{eff} = 9.8\,\mathrm{cm}$ and tungsten emissive biasing probe (stars) at $r_{eff} = 10.6\,\mathrm{cm}$; light green star refers to non-emissive operation of tungsten probe.

Negative biasing of the biasing probe with respect to the vacuum vessel has not produced observable changes to the radial electric field. The use of a large emissive biasing probe allowing to draw larger negative currents has shown not to impact the radial electric field. With positive biasing it has been possible to modify the radial electric field. As long as the biasing current can be increased the radial electric field could be increased. This is independent of the presence of the limiter. With biasing voltages exceeding $U_{Bias} > +60\,\mathrm{V}$, a second plasma state has been found in case of the limiter installed. Both plasma states live much longer than the confinement time of 1 ms. In plasma in the high-n_e-T_e state a reduced radial electric field compared to a plasma in the low-n_e-T_e state has been observed near the biasing probe.
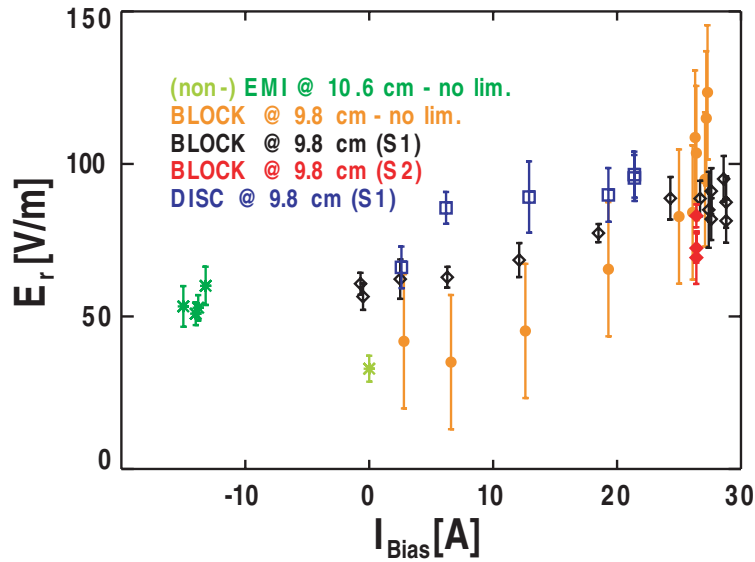
Figure 6.27: Overview of radial electric field near the biasing probe tip for the data presented in figure 6.26 as function of the biasing current.

As the plasma with limiter removed is in the high-n_e-T_e state from the beginning on the characteristics are a bit different. The radial electric field near the biasing probe is found to be smaller for smaller and no biasing if the limiter is removed. With increasing the bias of the biasing probe and drawing more current, the radial electric field increased. The increase is stronger if the limiter is removed. The saturated value is also larger if no limiter is present as can be seen in figures 6.26 and 6.27.

Looking at the biasing current (figure 6.29) and voltage (figure 6.28) dependencies of the confined energy relative to the unbiased case, a reduction of the confined energy with biasing was found with the limiter installed (black open diamonds in figures 6.28 & 6.29).
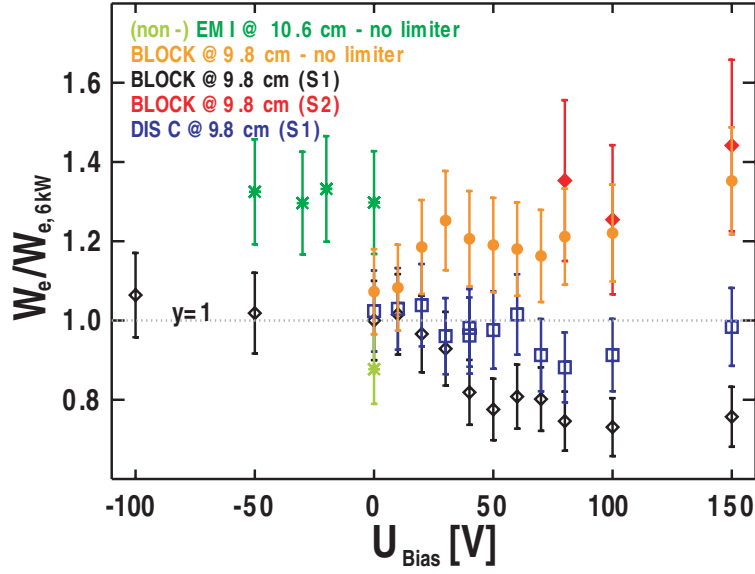
Figure 6.28: Dependency of the confined energy relative to the unbiased discharge on biasing voltage for the biasing campaign using 6 kW ECRH power with the carbon biasing probe placed at $r_{eff} = 9.8$ cm and the emissive probe placed at $r_{eff} = 10.6$ cm; $W_{e,6\mathrm{kW}} = 0.1$ J.

This reduction could be reduced by the use of a more optimized biasing probe (blue open squares). The high-n_e-T_e state (red filled diamonds) shows a significant increase in confined energy of $\approx 20 - 50\,\%$ compared to the first state with the same biasing voltage applied.
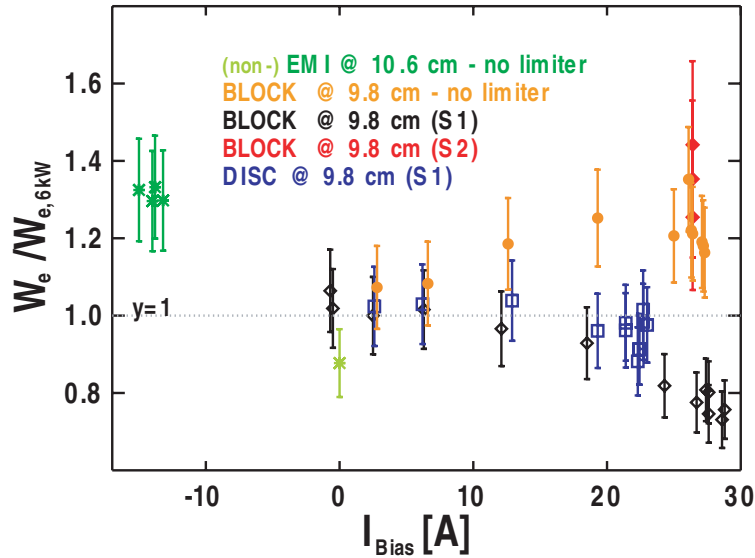
Figure 6.29: Dependency of the data presented in figure 6.28 on biasing current; $W_{e,6\mathrm{kW}} = 0.1$ J.

Using the emissive probe (green stars) allowed obtaining levels of confined energy

otherwise only accessible with large positive bias in the second state.

Looking at the confined energy versus the biasing power shows that the second found state appears to be the extension of the tendency observed when increasing the available heating power, as can be seen in figure 6.30.
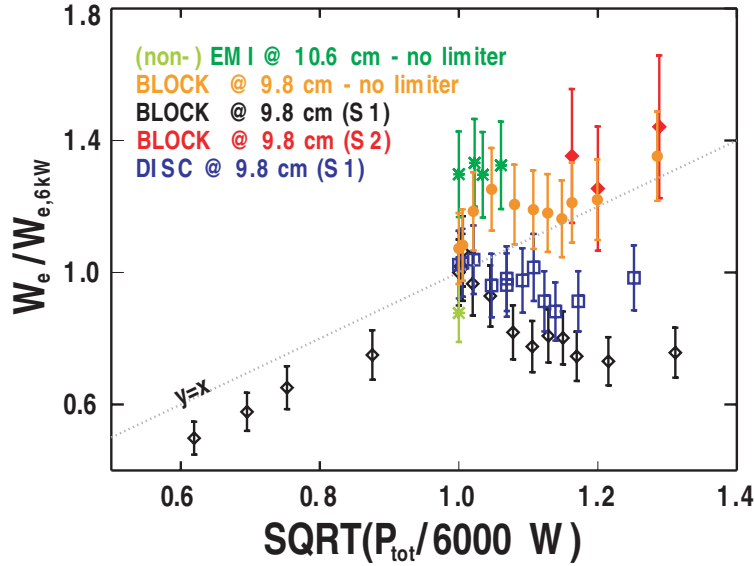
Figure 6.30: Confined energy versus the total input power $(P_{Bias} + P_{ECRH})$ for the campaign involving an ECRH power of 6 kW; $W_{e,6\mathrm{kW}} = 0.1\,\mathrm{J}$.

The low-n_e-T_e state shows a deviation from the power scaling for higher biasing power. The use of a different carbon probe allowed to change the initial discrepancy, but for higher biasing power a deviation from the line is observed as well.

Chapter 7

Cross-checking Results

The following section will present a comparison of particle and energy balances of an atomic model involving the relevant atomic processes in WEGA as presented in [Hor04] with the results of the neoclassical Hinton- Hazeltine (HH) model as presented in [HH76]. In both models the fraction of fast particles known to exist near the LCFS is not included, as its contribution to the atomic processes is small as has been shown by [Hor04]. The models will be used to interpret the observed changes occurring when biasing. The models are verified by comparison against each other and by comparing the obtained results to bolometry and the ECRH power deposition profile. Using the models it is possible to obtain an assessment of the absorbed ECRH power - a quantity hard to assess otherwise due to the complex heating mechanism. The models include only singly charged argon ions and neutrals. This is already included in the corresponding equations by setting $n_i = n_e$, respectively $Z_{eff} = 1$.

7.1 Basic Atomic Model

Knowing the underlying atomic mechanisms from [Hor04], the particle balance in steady state can be written as a balance between ionization and recombination:

$$\mathrm{div}\Gamma_e = n_e \cdot n_0 \cdot S_{ion} - n_e \cdot n_e \cdot S_{rec}, \tag{7.1}$$

with $S_{ion,rec}$ being the ionization and recombination rate coefficients taken from references [LSS02, Vor97] (shown in figure D.1 in appendix D), n_e, n_0 are electron and neutral particle density and Γ_e is the electron particle flux. As the recombination rate coefficient is small compared to the ionization rate coefficient, the particle

balance is dominated by ionization. Recombination is only taking place at the wall.

$$\text{div}\Gamma_e \approx n_e \cdot n_0 \cdot S_{ion} \tag{7.2}$$

The neutral particle density n_0 is assumed constant. It is calculated from the ideal gas law,

$$p_0 = n_0 \cdot k_B \cdot T_0. \tag{7.3}$$

The gas temperature has been determined from spectroscopy [RFB04] to be $T_0 = 500\,\text{K}$.

Concerning the energy balance, the microwave input power has to compensate all loss processes. The power balance taking the relevant processes into account can be written as:

$$\text{div}Q_E = p_{mw} + p_{Bias} + p_{ion} + p_{rec} + p_{rad}^{neutr.} + p_{rad}^{ions} + p_{calori} + p_W^{el.,ions} - e\Gamma_e E_r \tag{7.4}$$

with $p_{mw,Bias}$ being the input power density by microwave and biasing, p_{ion}, p_{rec}, $p_{rad}^{neutr.}$, p_{rad}^{ions} are energy losses due to ionization, recombination, neutral and ion excitation radiation. p_{calori} refers to the energy used to heat the electrons to their thermal energy. $p_W^{el.,ions}$ refers to energy transfer from electrons to ions. $-e\Gamma_e E_r$ is the energy picked up (or lost) by electrons in the electric field. As convention the sign of the power densities is chosen such, that outward bound energy fluxes are positive, whereas inbound fluxes are negative. The individual contributions from equation 7.12 can be calculated according to:

$$
\begin{aligned}
p_{ion} &= n_e n_0 E_{ion} S_{ion} \\
p_{rec} &= \tfrac{3}{2} T_e n_e^2 S_{rec} \\
p_{rad}^{neutr.} &= n_e n_0 < E >^{neutr.} < S_{rad} >^{neutr.} \\
p_{rad}^{ions} &= n_e^2 < E >^{ion} < S_{rad} >^{ion} \\
p_{calori} &= \tfrac{3}{2} T_e n_e n_0 S_{ion} \\
p_W^{el.,ions} &= \frac{\tfrac{3}{2} n_e\, k_B\,(T_e - T_i)\,\sqrt{2\pi}\,n_e\, e^4\, \ln\Lambda}{6\pi^2 \varepsilon_0^2 \sqrt{m_e}(k_B T_e)^{\frac{3}{2}}}.
\end{aligned}
\tag{7.5}
$$

with $E_{ion} = 11.5\,\text{eV}$, $S_{ion,rec}$ as above and $< E >^{neutr.,ion} < S_{rad} >^{neutr.,ion}$ are energy rate coefficients for excitation of argon neutrals and ions. The energy rate coefficients for the first 4 processes are taken from [LSS02] (as displayed in figure D.2 of appendix D). $\ln\Lambda$ is the Coulomb logarithm. The transfer of energy from electrons to ions is small compared to the rest of the energy loss processes and can

be neglected.

All the above terms can be calculated from measured data presented in chapters 5 & 6. The results can be compared to the microwave power deposition profile.

7.2 Hinton- Hazeltine Model

The Hinton- Hazeltine model has originally been used to describe particle and energy flux of large aspect ratio ($\frac{R}{a} > 5$; WEGA≈ 6) tokamak with circular flux surface cross sections operating in the Pfirsch-Schlüter and plateau collisionality regimes [HH76]. The collisionality of typical WEGA discharges is in the appropriate collisionality regime as is shown in figure E.3 of appendix E. As WEGA is not a tokamak, but a stellarator several input values to the HH model are set $\equiv 0$ in order to represent the stellarator nature (e.g. $U_{loop} \equiv 0\,\text{V}$). Also the conditions of the low field operation of WEGA are included by assuming constant parameters over the whole radius (e.g. $T_i = const. = 2\,\text{eV}$ or $p_n = const.$). The Hinton- Hazeltine model does not account for transport caused by fluctuations. As the level of fluctuations in WEGA's ECR-heated low field argon discharges is low, except for the edge of the confined region (see Appendix E), this approximation is considered to be acceptable. The HH model is used primarily to verify the atomic model. A second important aspect to the HH model is that it is used to verify that the neoclassical energy flux is small. The model is widely accepted as a basic reference for modeling tokamaks meeting the above requirements and as bottom estimate for more advanced ones. As for the atomic model, it is assumed that only singly charged ions exist ($Z_{eff} \equiv 1$), respectively $n_e = n_i$.

The HH model is used to calculate the electron transport coefficient matrix $\hat{D} = \begin{pmatrix} D_{11} & D_{12} \\ D_{21} & D_{22} \end{pmatrix}$. The matrix is then used to calculate the particle flux according to

$$\Gamma_e = n_e \left[D_{11} \left(\frac{n_e'}{n_e} + \frac{eE_r}{T_e} \right) + D_{12} \frac{T_e'}{T_e} \right], \qquad (7.6)$$

with $'$ denoting the radial derivative, and the energy flux

$$Q_E = n_e T_e \left[D_{21} \left(\frac{n_e'}{n_e} + \frac{eE_r}{T_e} \right) + D_{22} \frac{T_e'}{T_e} \right] \qquad (7.7)$$

based on the experimental data in order to compare them with the atomic model. The novel of this approach to the one presented by Horvath in [Hor04] is that not effective diffusion coefficients, depending only on the density gradient, are calculated,

but particle and energy flux are directly related to the driving thermodynamic forces $\frac{n_e'}{n_e}$, $\frac{eE_r}{T_e}$ and $\frac{T_e'}{T_e}$.

The obtained particle flux will be compared to the particle flux obtained with the atomic model. For the power balance the HH model will be used to verify that the neoclassic energy transport is small in all cases.

7.3   Results of Modeling

In the following the two models are applied to selected discharges. The modeling results will be qualitatively interpreted based on the heating power deposition profile introduced in chapter 4.1.2 and the location of the biasing probe.

7.3.1   Reference Discharge

As a first test, both models will be applied to the reference discharge without the biasing probe inside the vessel.

Looking at the particle balance first, the atomic model is dominated by ionization as mentioned earlier. The direct comparison of the particle fluxes derived from the atomic model with the results obtained using the HH model is shown in figure 7.1.
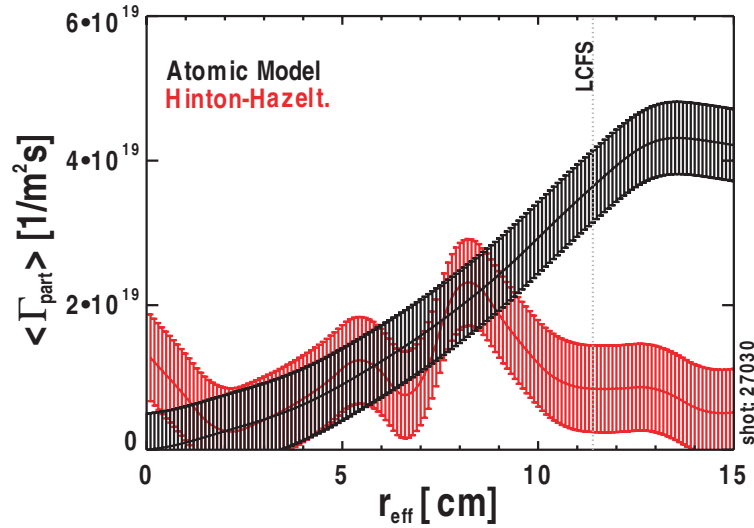
Figure 7.1: Particle fluxes derived from the atomic model (black) and the Hinton-Hazeltine model (red) for the reference discharge.

As can be seen the models agree well in the region inside $r_{eff} \approx 8$ cm. The region beyond $r_{eff} \approx 8$ cm is not as well represented. Also, the qualitative behavior is not quite reproduced, but given that all calculations use the measured data as input,

the agreement of the profiles is satisfactory, especially in the region where no level of turbulence has been detected (see top figure of figure E.1 of appendix E). The non-zero value of the flux at $r_{eff} = 0$ cm is due to the density profile showing a maximum at $r_{eff} \approx 2$ cm. Also the radial electric field derived from probes does not converge to 0, but to a finite value, giving a non-zero contribution. The reduction of the flux beyond $r_{eff} \approx 13$ cm is an effect of the increase in volume of the effective cylindrical flux surface.

Looking at the power balance equation in case of the reference discharge the input power terms are reduced to the microwave power. Figure 7.2 shows the contributions of the individual atomic processes to the power balance for the reference discharge.
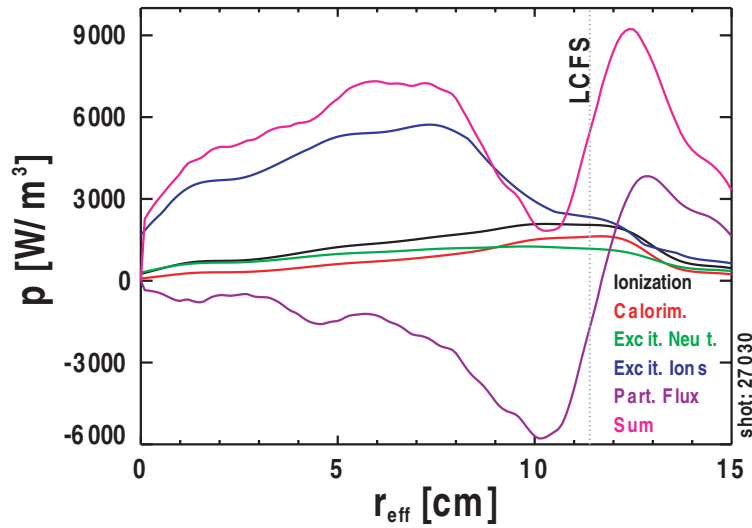
Figure 7.2: Contributions of relevant atomic processes to the power density of the reference discharge.

The particle flux in the electric field leads to a transport of energy inwards as the electrons gain energy in the radial electric field - an inward heat pinch. All other mechanisms lead to a loss of power. The net direction of energy flux is outward at any point in the confined region, as the pink curve always remains positive. Energy is lost from the plasma. The leading loss term, in the case of the reference discharge, is the loss due to line radiation of ions. Other important loss channels are ionization, the calorimetric contribution and line radiation of neutrals. The contribution of recombination as well as direct energy transfer from electrons to ions is small and not shown in figure 7.2. The results can be compared to the bolometer as is done in figure 7.3 by integrating the radiated power along the line of sight of the bolometer. As the bolometer is able to detect only losses due to radiation, only excitation of neutrals and ions leading to emission of radiation, have to be taken into account.

The bolometer conducts a line-integrated measurement, so the model results are mapped to the bolometer position and the line-integral value for every bolometer channel is calculated separately. r_{imp} gives the minimum distance of the center of the bolometer line-of-sight to the center of the vacuum vessel.
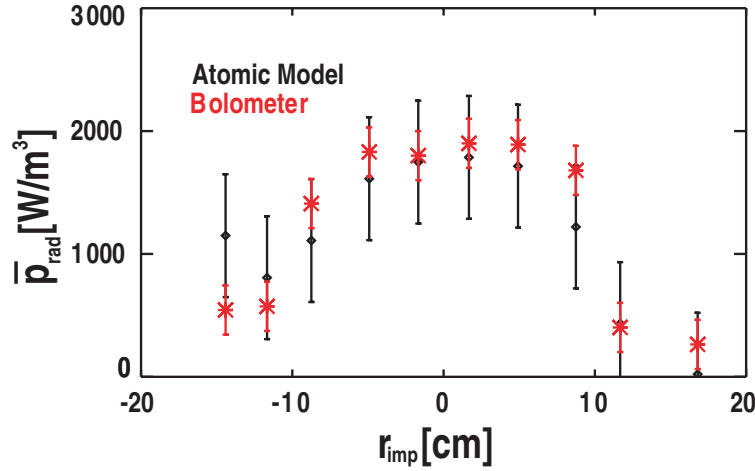
Figure 7.3: Bolometer measurements (red) and model results (black) for the reference discharge.

The model results correspond well to the bolometer measurements. The radiation part of the model is thus considered to represent the conditions of the reference discharge well. Comparing the total radiation loss of the plasma, the bolometer gives a total radiated power of $P_{Bolo} = 480 \pm 50\,\text{W}$ and the atomic model a radiated power from neutrals and ions of $P_{atomic} \approx 510 \pm 100\,\text{W}$.

As a second check and as the bolometer is only covering two processes, the total power flux will be compared to the ECRH power flux. Starting from equation 7.4 and integrating once the balance between loss power flux and input power flux can be written as

$$Q_E = \tilde{P}_{mw} + \tilde{P}_{atomic}. \tag{7.8}$$

Here, Q_E is calculated by the HH model according to equation 7.7. $\tilde{P}_{atomic}$ is calculated from the power density of the atomic model and $\tilde{P}_{mw}$ is the power flux from the microwave. The result is shown in figure 7.4.

Neoclassical transport does not play a significant role as it is much smaller than the contributions of the atomic processes. It is, hence, neglected. According to equation 7.8, all loss processes have to be balanced by the input microwave power. Integrating the profile one obtained a total loss power loss of $P_{atomic} \approx 1840 \pm 350\,\text{W}$.
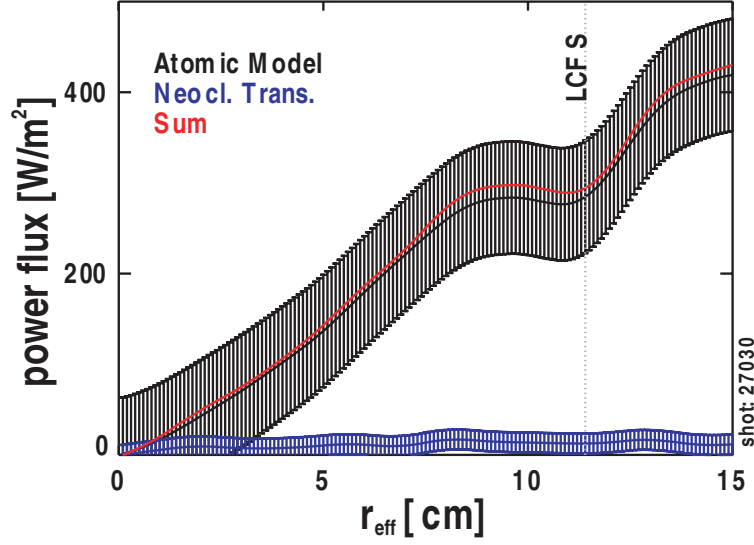
Figure 7.4: Power fluxes derived from the atomic model (black) and Hinton-Hazeltine (blue) for the reference discharge.

The power deposition profile has been determined for the same discharge by Podoba [PLW+07]. For comparing to the model, the profile introduced in section 4.1.2 has been scaled to the loss power from the modeling. As neoclassical energy transport can be neglected, equation 7.8 can be written as $\tilde{P}_{atomic} = -\tilde{P}_{mw}$ (remember: $\tilde{P}_{mw} < 0$!). The ECRH flux and and the flux from the modeling are shown in figure 7.5.

Figure 7.5: Power fluxes resulting of the atomic model (black) and based on the scaled power deposition profile for the reference discharge (red); dotted lines represent uncertainties.

Both profiles agree well. The ECRH conversion efficiency for the reference dis-

charge is $\eta_{mw} = \frac{P_{atomic}}{P_{mw,\,out} - P_{mw,\,refl}} = \frac{1840}{5530} \approx 33\,\%$. According to [Pod06] a conversion factor in the order of 20 - 40 % can be expected. This agrees well with the result of the model.

It can be concluded that the model represents the conditions in WEGA in case of the low field argon discharge well. Even close to the LCFS, where its applicability is limited, the difference between the model and the scaled ECRH power is not too large.

7.3.2   Non-energized Biasing Probe

The penetration of the biasing probe led to a reduction in plasma density as shown in chapter 5.3.2. As for the reference discharge, the particle balance is governed by ionization. The particle fluxes derived with the atomic model and HH are shown in figure 7.6.
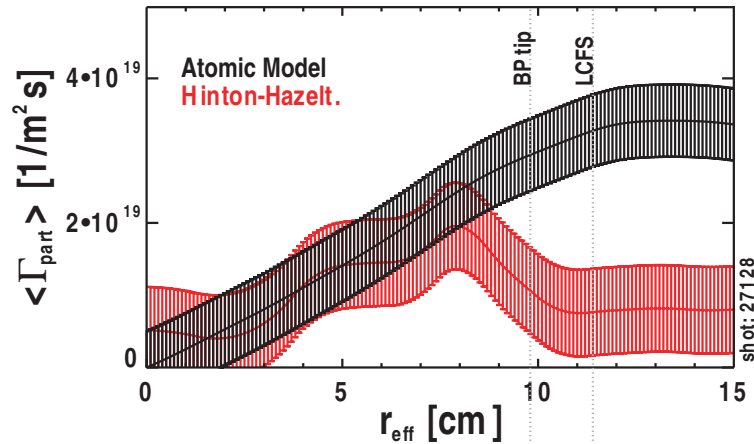
Figure 7.6: Particle fluxes derived from the atomic model (black) and the Hinton-Hazeltine model (red) for the biasing probe placed at $r_{eff} = 9.8\,\mathrm{cm}$.

Both profiles agree well within the confined region. An interesting feature which can be seen for the reference discharge, as well as in the case of the unbiased probe, is the HH model underestimating the flux outside the first PFC compared to the atomic model. This can be interpreted as follows: The atomic model assumes flux surfaces even beyond the limiting objects (biasing probe & antennas) up to $r_{eff} = 20\,\mathrm{cm}$. As the atomic model is also 1-dimensional, the existence of limiting objects, such as the antennas or the biasing probe shaft are not included. Limiting structures as the antennas or the biasing probe allow particles to escape towards the wall parallel to the magnetic field as a magnetic separatrix does not exist within the vessel. These losses parallel to the field are significantly higher than losses perpendicular to the

magnetic field. The atomic model requires hence a higher radial flux than the HH model.

The energy losses contributing to the power balance, in the case of the unbiased probe, are displayed in figure 7.7. The major loss channel is line radiation of ions, followed by ionization. The presence of the biasing probe reduces the power losses in its vicinity due to the reduced density.
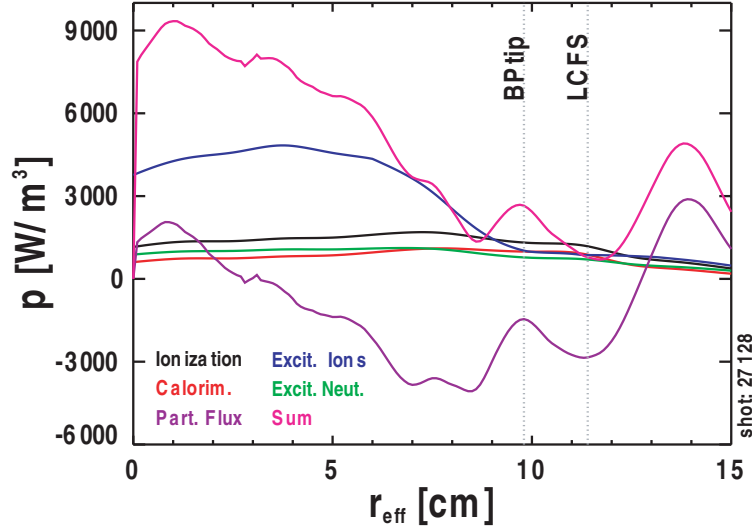
Figure 7.7: Contributions of relevant atomic processes to the power density for the unbiased discharge with biasing probe placed at $r_{eff} = 9.8\,\mathrm{cm}$.

Again, the power flux can be cross-checked with the bolometer. The result of simulating the bolometer results is displayed in figure 7.8.
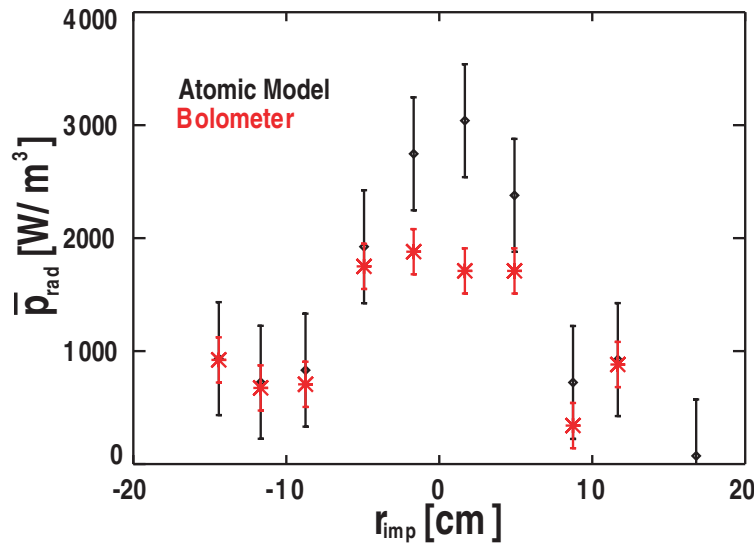
Figure 7.8: Bolometer measurements (red) and model results (black) for the unbiased probe placed at $r_{eff} = 9.8\,\mathrm{cm}$.

The total lost power derived from bolometric measurements is $P_{Bolo} = 450 \pm 50\,\text{W}$. The total power loss according to the mapped model for the bolometer is $P_{model} \approx 470 \pm 140\,\text{W}$. This agrees well. The modeling of the bolometer results can be considered to include the relevant processes and reproduce the conditions met in WEGA. The power derived from the model will overestimate the contribution of the plasma outside the LCFS, as it assumes circular cross sections centered in the vacuum vessel. The bolometer will, on the other hand, underestimate the contribution as its lines of sight do not cover the whole poloidal cross section.

Again, the comparison to the neoclassic transport derived from the HH model can be made. The results for the unbiased probe are shown in figure 7.9.
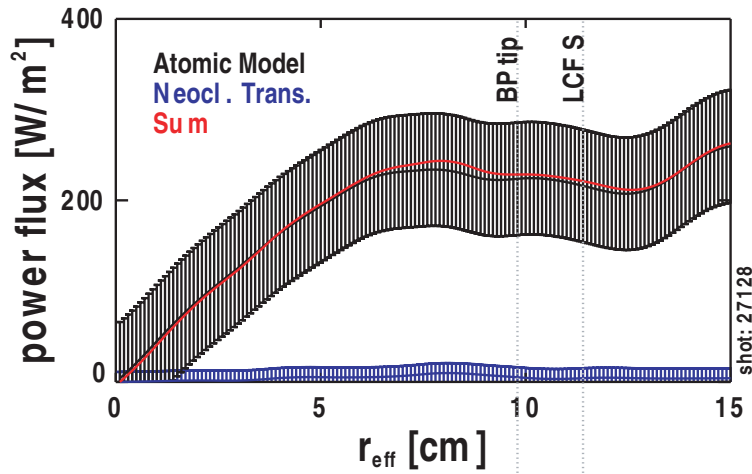
Figure 7.9: Power fluxes derived from the atomic model (black) and the Hinton-Hazeltine model (blue) for the biasing probe placed at $r_{eff} = 9.8\,\text{cm}$.

As for the reference discharge, the neoclassical contribution to the energy flux can be neglected. With the probe not being energized, but only placed at the LCFS the biasing power is small ($P_{Bias} \approx 25\,\text{W}$) and indeed calculating the total power losses in the region between the biasing probe tip and the LCFS from the atomic model, the loss power is small, $P_{model} \approx 35 \pm 20\,\text{W}$. The loss processes, again, have to be compensated by the input ECRH power.

As detailed measurements of the power deposition profile are lacking for this discharge, but the gradient length and plasma shape are somewhat comparable to the reference discharge, the power deposition profile is assumed to be unchanged in shape. A comparison between the energy flux calculated with the atomic model and the ECRH system is shown in figure 7.10.

The profiles do not match quite as well as for the reference discharge, which indicates that the assumption of the unchanged ECRH power deposition profile is

limited. For this case the microwave efficiency can be calculated to $\eta_{mw} \approx 21\%$.
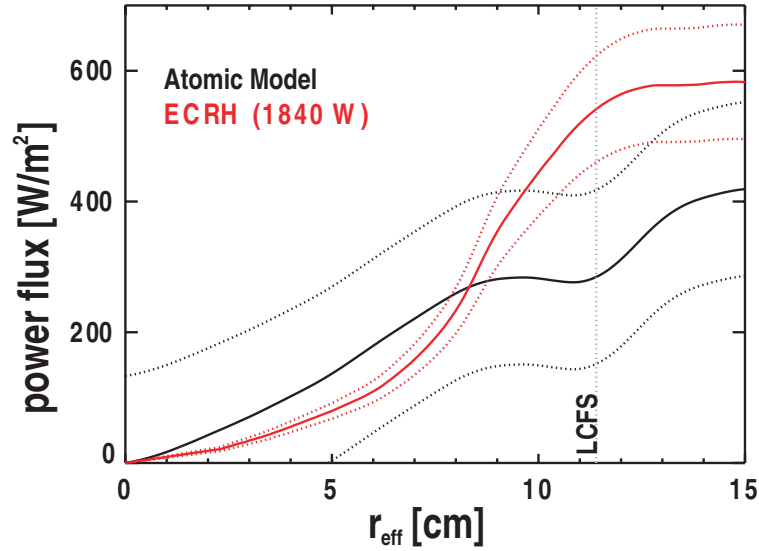

Figure 7.10: Power fluxes resulting of the atomic model (black) and based on the scaled power deposition profile (red) for unbiased biasing probe placed at $r_{eff} = 9.8\,\mathrm{cm}$ cm; dotted red lines represent uncertainties.

7.3.3 Probe Biased at $U_{Bias} = +70\,\mathrm{V}$ (low n_e-T_e state)

The same procedure employed before can also be used to look at the biased plasma in the low n_e-T_e state (reduced density). The particle balance for the low n_e-T_e state based on the models is displayed in figure 7.11.
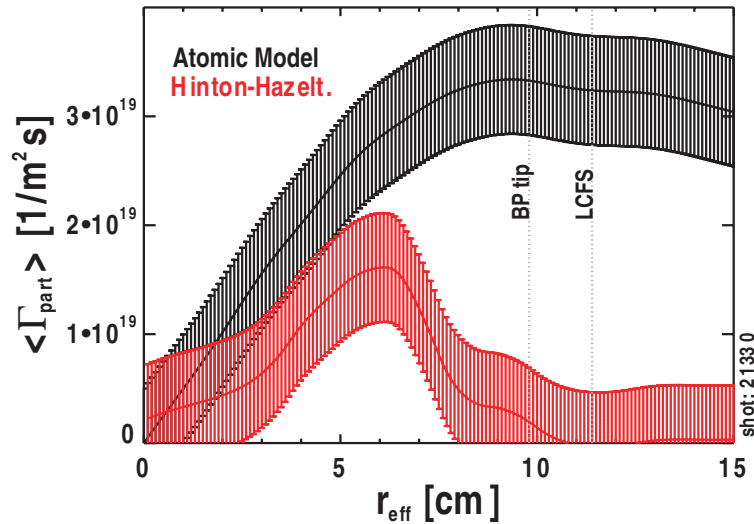
Figure 7.11: Particle fluxes derived from the atomic model (black) and the Hinton-Hazeltine model (red) for the energized biasing probe ($U_{Bias} = +70\,\mathrm{V}$) placed at $r_{eff} = 9.8\,\mathrm{cm}$.

As can be seen, the particle balance is as well fulfilled beyond $r_{eff} \approx 5$ cm and the atomic model shows a larger flux than the HH model, again. The particle flux near the plasma edge as well as outside the LCFS shows the same characteristic deviation as before. It has been observed when biasing the plasma that the level of turbulence increases (see bottom figure of figure E.1).

The major power loss channel, line radiation of ions, even exceeds the contribution of convection in the low n_e-T_e state. The contribution is about three times as large as in the unbiased case as is shown in figure 7.12.
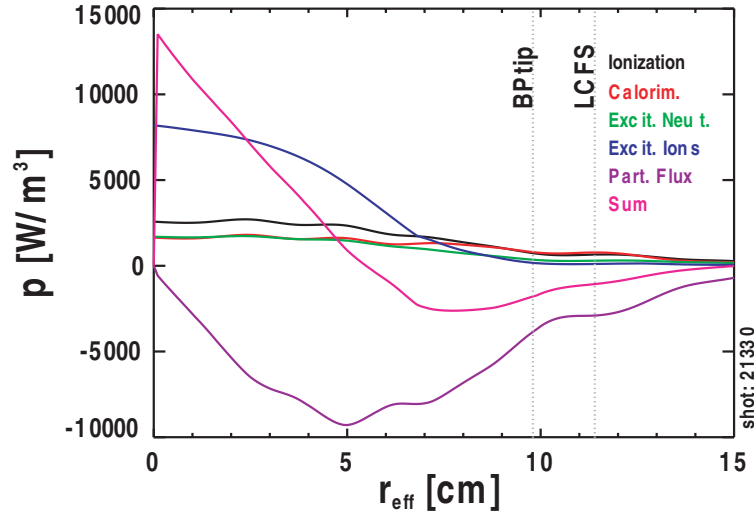
Figure 7.12: Contributions of relevant atomic processes to the power lost for the biasing probe biased at U_{Bias}=+70 V and placed at $r_{eff} = 9.8$ cm (first state).

Using this model to simulate the bolometer measurements under the biased conditions yields the results presented in figure 7.13.
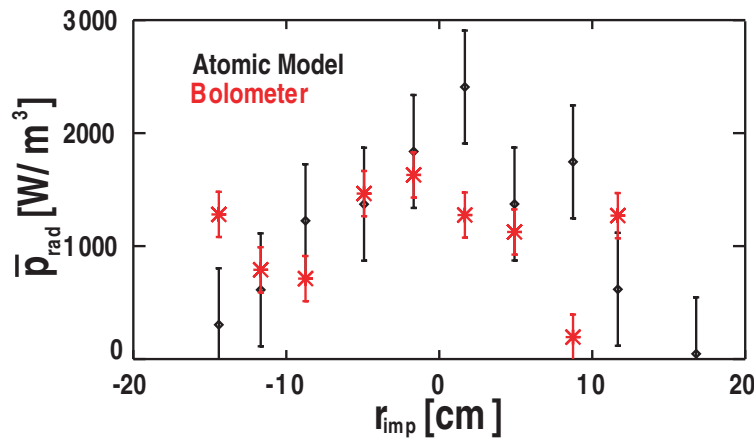
Figure 7.13: Measured (red) and simulated (black) bolometer for the discharge biased at $U_{Bias} = +70$ V with the biasing probe placed at $r_{eff} = 9.8$ cm.

The results of the model agree reasonably well with the bolometer measurements. The total power loss due to atomic processes can be calculated to $P_{model} \approx 440 \pm 130\,\text{W}$. The bolometer result of $P_{Bolo} = 570 \pm 60\,\text{W}$. The integration of the results shown in 7.12 can be carried out and the resulting power flux can be compared to the contribution of the neoclassic energy flux as is done in figure 7.14.
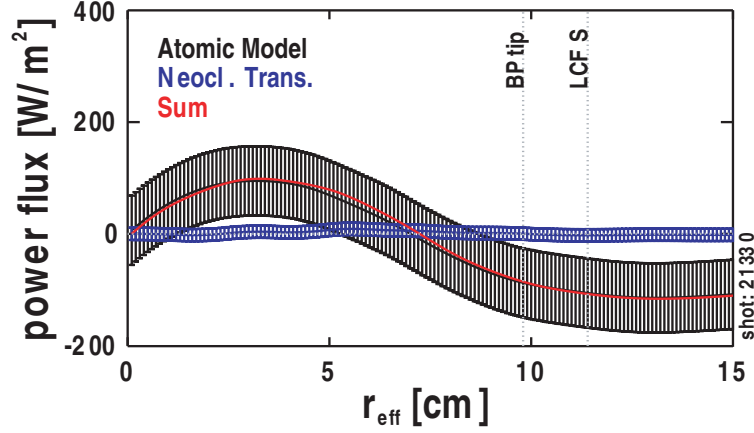
Figure 7.14: Power fluxes derived from the atomic model and Hinton-Hazeltine for the biasing probe biased at $U_{Bias} = +70\,\text{V}$ and placed at $r_{eff} = 9.8\,\text{cm}$ (first state).

The contribution of the neoclassical energy flux is small as in the previous cases. It can also be seen that the atomic model yields a negative contribution beyond $r_{eff} \approx 7.5\,\text{cm}$. This shows that the power balance cannot be fulfilled by balancing the atomic model with the input ECRH alone. The model has to be extended. As this state is biased, the impact of the biasing probe has to be modeled in order to obtain reasonable results for absorbed power and correctly interpret the power fluxes. In the following, a basic model for the biasing probe will be introduced and applied. The power lost from the plasma due to atomic processes has to be balanced by the input power, now consisting of the ECRH power $\tilde{P}_{mw}$ and the biasing probe $\tilde{P}_{Bias}$:

$$Q_E = \tilde{P}_{mw} + \tilde{P}_{Bias} + \tilde{P}_{atomic}. \tag{7.9}$$

As the probe has a rather large radial extent and is placed in different parts of the magnetic geometry the following three regions will be considered:

1. Area between biasing probe tip and LCFS
2. Area in front of the probe
3. Area beyond the LCFS

In the area between the probe tip and the LCFS the probe is an electrical short

circuit as the biasing probe including its uptake is located here. The assumed power deposition profile is assumed to be homogeneous in this region as there is no useful criterion for discrimination. In front of the biasing probe the plasma will shield the effect of the probe. An exponential drop of the power deposition with the distance to the probe is thus assumed. In the region behind the probe a linear drop of the power deposition with the distance to the wall is assumed. The total power is set equal to the electric power fed to the probe:

$$P_{Bias} = U_{Bias} \cdot I_{Bias} = 4\pi^2 \cdot R \int\limits_{0}^{wall} \tilde{P}_{Bias} dr'_{eff}. \tag{7.10}$$

The biasing power deposition profile according to the above criteria is expressed by

$$\tilde{P}_{Bias}\left(r_{eff}\right) = \begin{cases} c_1 \cdot \exp\left(\frac{r_{eff}-c_3}{c_2}\right) & r_{eff} < c_3 \\ c_1 & c_3 \le r_{eff} \le r_{eff,LCFS} \\ c_1 \cdot \left(1 - \frac{r_{eff}-r_{eff,LCFS}}{20\,\mathrm{cm}-r_{eff,LCFS}}\right) & r_{eff,LCFS} < r_{eff} < 20\,\mathrm{cm} \end{cases} , \tag{7.11}$$

where the parameters c_3 & c_2 have been determined from different experiment scenarios with varied microwave power, biasing power and biasing probe position to be $c_3 = \mathrm{BPtip} - 1.0 \pm 0.3\,\mathrm{cm}$ and $c_2 = 1.4\,\mathrm{cm} \pm 0.1\,\mathrm{cm}$. This leaves only one free parameter, c_1, which is determined by the normalization given in equation 7.10.

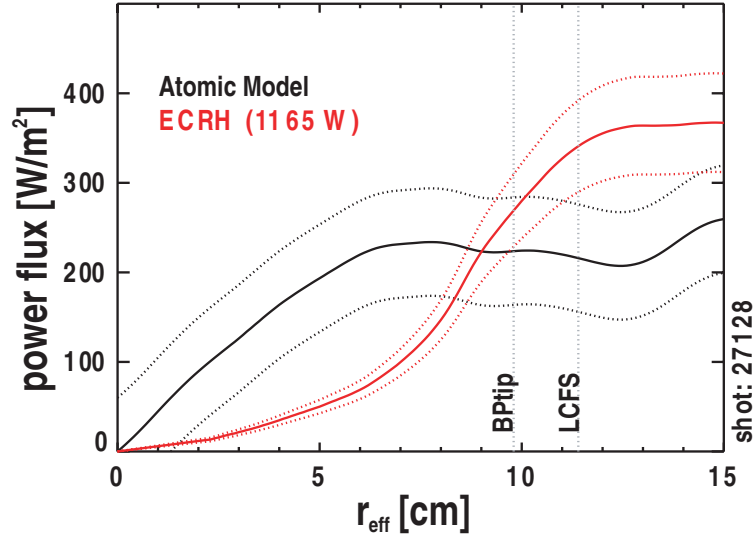Figure 7.15: Power fluxes resulting of the atomic model (black) and ECRH based on the measured power deposition profile (red) for biasing probe biased at $U_{Bias} = +70$ V (green) placed at $r_{eff} = 9.8$ cm; dotted lines represent uncertainties.

The result from combining the atomic model and biasing power is indicated by the blue line in figure 7.10 and matches the ECRH flux quite well. As can be seen, biasing is an outward bound power flux - an energy sink. This is reasonable as the current is drawn from the plasma onto the probe. The presented assumption fits well to the measured data for the given biasing power deposition. The total input power can be calculated by adding the contribution of the biasing probe to the atomic model. This yields a total power contribution of $P_{atomic} + P_{Bias} \approx 2080 \pm 520\,\mathrm{W}$. Assuming both processes need to be compensated by the input ECRH power, the comparison to the scaled the power deposition profile can be made. The resulting profiles are compared in figure 7.16.
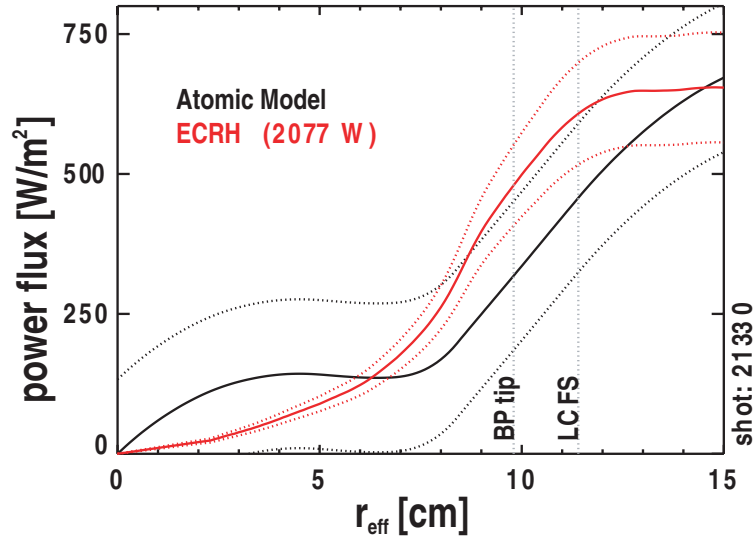
Figure 7.16: Comparison of total energy fluxes of the atomic processes and the biasing probe (black) and the scaled input ECRH (red) for the discharge biased at $U_{Bias} = +70\,\mathrm{V}$ with biasing probe placed at $r_{eff} = 9.8\,\mathrm{cm}$; uncertainties are marked by dotted lines.

As can be seen the profiles match well. The estimated microwave efficiency in the biased case is $\eta_{mw} \approx 35\,\%$. This fits well to the estimated efficiency range for the OXB-mode conversion process.

7.3.4   Probe Biased at $U_{Bias} = +70\,\mathrm{V}$ (High n_e-T_e state)

Energizing the probe impacts the plasma parameters significantly, as is shown in chapter 6, especially, if the biasing voltage exceeds $U_{Bias} = +70\,\mathrm{V}$. In order to attempt a basic understanding of the observed plasma state, the introduced model will be applied to it. As this state is more stably observed with the limiter removed data from the final campaign (with emissive probe) will be used. When looking at the particle balance the result is similar to a plasma in the low n_e-T_e state although the particle flux is higher by about 30 %. The results for the particle balance using both models is displayed in figure 7.17.
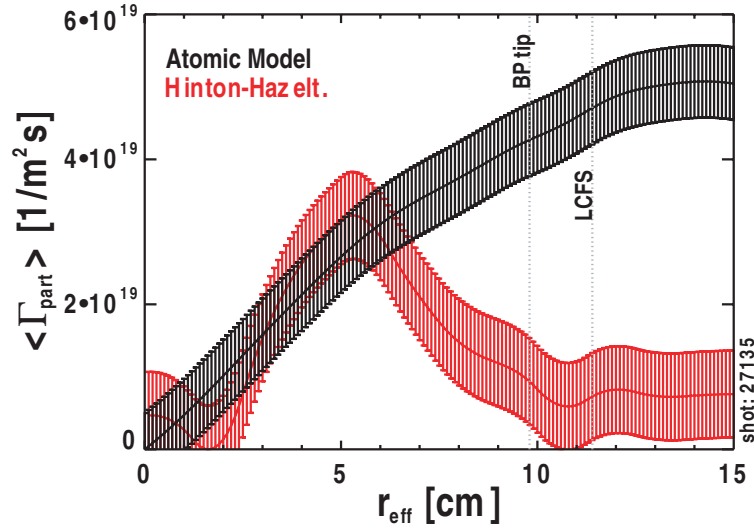
Figure 7.17: Particle fluxes derived from the atomic model (black) and Hinton-Hazeltine (red) for the biasing probe biased at $U_{Bias} = +70\,\mathrm{V}$ and placed at $r_{eff} = 9.8\,\mathrm{cm}$.

The discrepancy in both profiles can, again, be related to the level of turbulence. As for the low n_e-T_e state, the biasing power has to be taken into account in the power balance,

$$Q_E = \tilde{P}_{atomic} + \tilde{P}_{Bias} + \tilde{P}_{mw}. \tag{7.12}$$

with $\tilde{P}_{Bias}$ referring to the input biasing power flux.

When biasing the plasma, the power density profile, displayed in figure 7.18, shows a large contribution to the energy flux pointing inward in between the biasing probe and the LCFS. The contribution of the losses due to ion radiation is even larger than in the low n_e-T_e state.
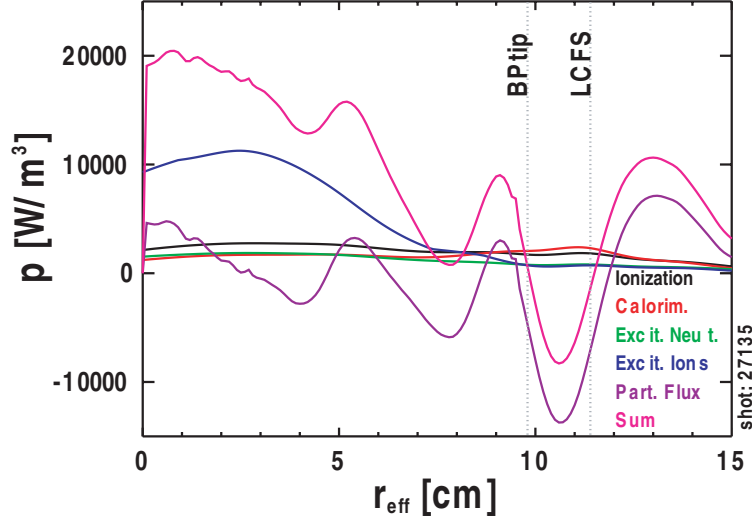
Figure 7.18: Contributions of atomic processes to the power density lost for the biasing probe biased at $U_{Bias} = +70\,\mathrm{V}$ and placed at $r_{eff} = 9.8\,\mathrm{cm}$.

Mapping these results to simulate the bolometer gives a good match to the bolometer data, as is shown in figure 7.19. The losses due to atomic processes add to a total of $P_{atomic} \approx 350 \pm 80\,\mathrm{W}$. The bolometer yields a power loss of $P_{Bolo} = 460 \pm 50\,\mathrm{W}$. Both values agree reasonably well.
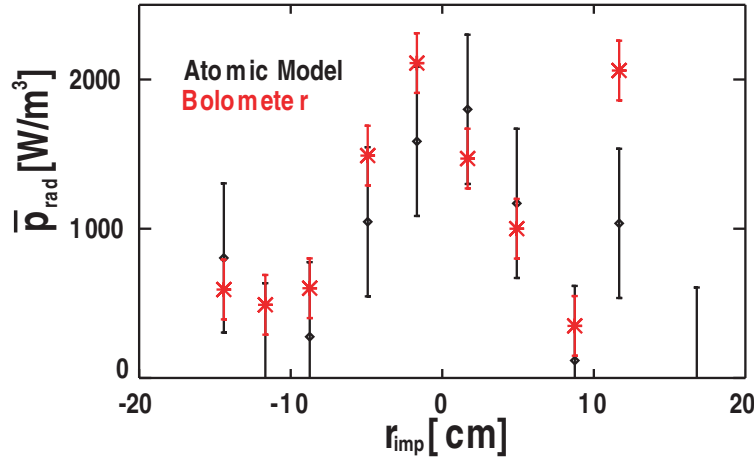
Figure 7.19: Measured (red) and simulated (black) bolometer results for a discharge in the second state with biasing probe placed at $r_{eff} = 9.8\,\mathrm{cm}$.

As before the neoclassical contribution to the energy flux is negligible, as is can be seen in figure 7.20. The power balance can again be considered by comparing biasing and atomic processes and the microwave heating, as $\tilde{P}_{atomic} + \tilde{P}_{Bias} = -\tilde{P}_{mw}$. The drawn biasing power is $P_{Bias} \approx 1850\,\mathrm{W}$. The total loss power accumulates to $P_{atomic} + P_{Bias} \approx 3820 \pm 1020\,\mathrm{W}$.
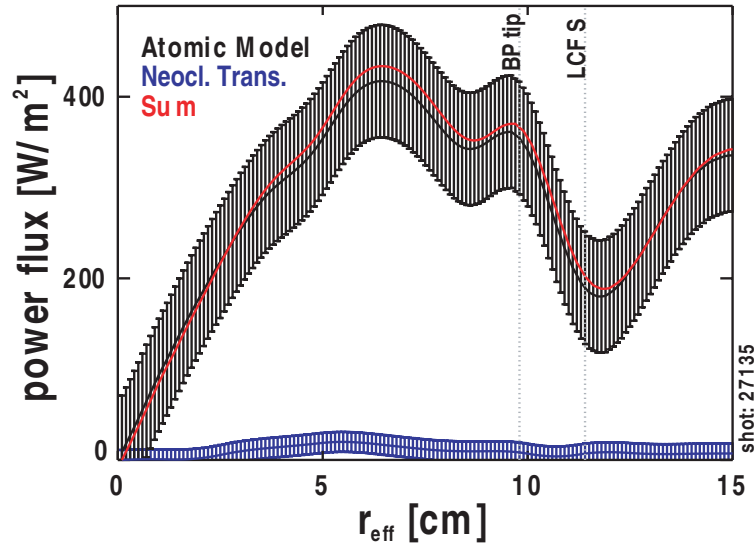
Figure 7.20: Power fluxes derived from the atomic model and Hinton-Hazeltine for the biasing probe biased at $U_{Bias} = +70\,\text{V}$ and placed at $r_{eff} = 9.8\,\text{cm}$.

Assuming a total absorbed power with the same power deposition as before, the flux contributions can be compared to the input ECRH flux as shown in figure 7.21.
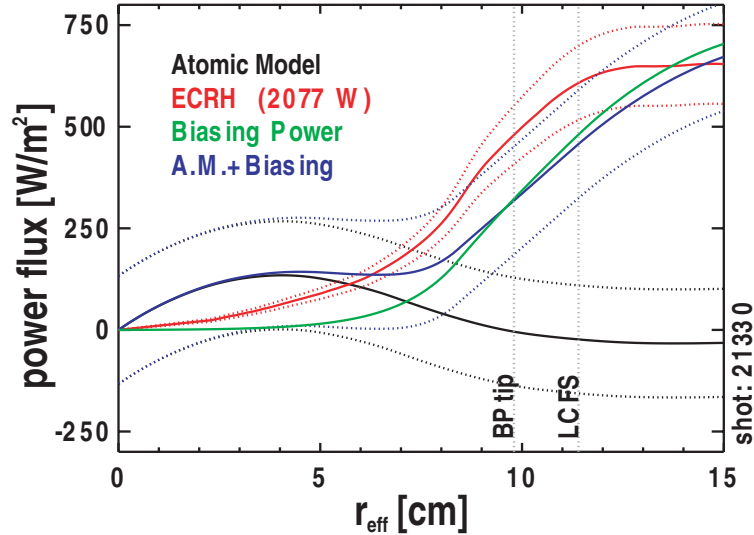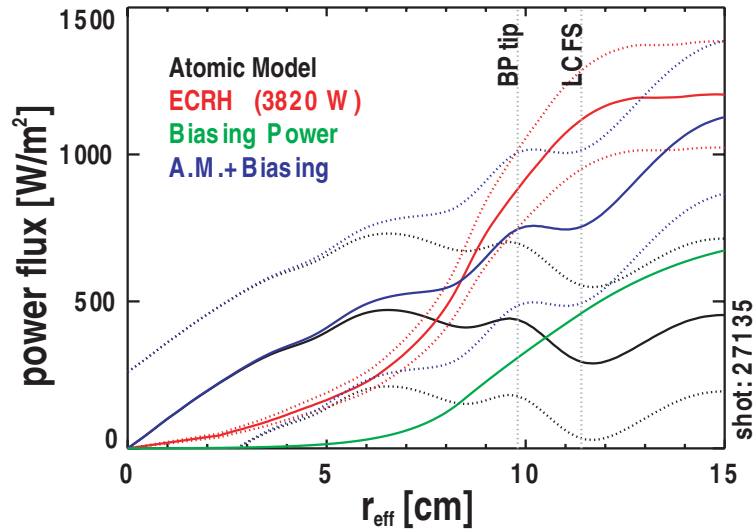

Figure 7.21: Power fluxes resulting of the atomic model (black) and based on the scaled power deposition profile (red) for biasing probe biased at $U_{Bias} = +70\,\text{V}$ (green) and placed at $r_{eff} = 9.8\,\text{cm}$; dotted lines represent uncertainties.

Reducing the plot to the input (ECRH) and lost power (atomic processes + biasing) fluxes eases comparing in figure 7.22. As the total flux profiles of input power and losses match reasonably well, the power balance is considered fulfilled for the high n_e-T_e state. The model assumptions still seem justified.
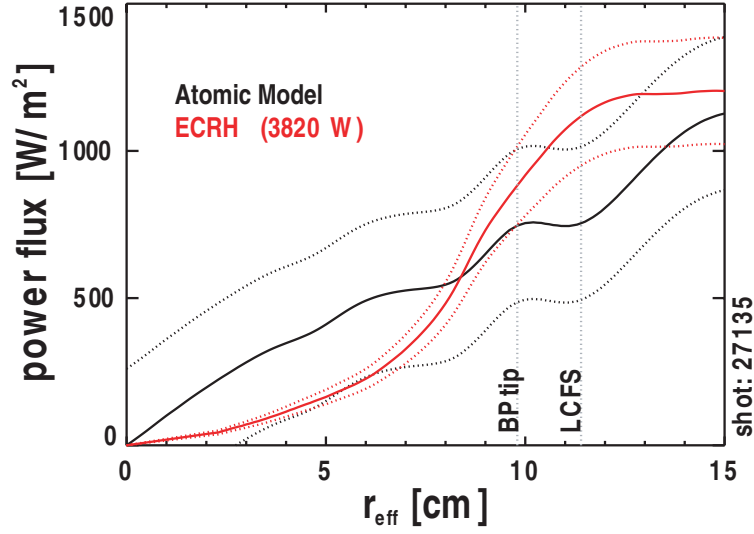
Figure 7.22: Power loss flux due to atomic processes and biasing (black) compared to the scaled input ECRH power (red).

When considering the efficiency of the microwave, the reflected power into the magnetron has to be subtracted from the launched 6 kW. As about 1.3 kW of the launched 6 kW is reflected back into the waveguide, only 4.7 kW remain for plasma heating. Together with the lost 3820 W, this give a conversion efficiency of the ECRH system of $\eta_{mw} \approx 81\,\%$ for the high n_e-T_e state. This is a very high value, much higher than originally expected. It has to mentioned that the estimated efficiency of 20 - 40 % for the OXB-mode conversion as reported by Podoba refer to single pass absorption. In reality, a large part of the wave is not converted. Instead, it is reflected towards the wall where it is then reflected back towards the plasma and available for another conversion attempt. The change in the plasma density profile and the plasma shape lead to changes in the complex microwave resonator which is formed by the plasma and the vacuum vessel. Assessing the conversion efficiency by modeling the complex resonator geometry consisting of the toroidal vacuum vessel and the 3-dimensional plasma is difficult and would require an extensive amount of modeling. Nevertheless, the found efficiency is much higher than in the low n_e-T_e state. It can in summary be concluded that the high n_e-T_e state does not only show a power scaling similar to the standard discharges, but it can be explained by an increase in the microwave heating efficiency.

Chapter 8

Summary

Biasing experiments are reported to improve the performance of tokamaks and stellarators alike [FIS$^+$98, KTT$^+$06b, VGM$^+$01]. It has been shown that biased divertors perform more efficient and achieve a better control over the divertor plasma [Boi92, RTH$^+$97, SLM$^+$91]. Moreover, biasing is applied in plasma fusion research in order to reduce the power threshold required to reach the H-mode operational regime [JOWB98, KGK$^+$01, WOB$^+$92].

Within the frame of this work, conducted at the WEGA stellarator at IPP Greifswald, fundamental experiments concerning biasing have been conducted to demonstrate the option of altering the radial electric field in a plasma by means of an externally biased probe. Due to the low available heating power of 26 kW at maximum in WEGA compared to the H-mode threshold, requiring a minimum of at least 100 kW, WEGA cannot be operated in the H-mode or near the H-mode threshold.

WEGA is used to magnetically confine low temperature, overdense plasmas in the regime of high collisionality and in toroidal geometry. The plasma is heated using the OXB-mode conversion process with 2.45 GHz magnetron sources [Pod06]. The produced plasmas are diagnosed using Langmuir and emissive probes, spectroscopy, interferometry and bolometry [Mar08, Lis05, ZOG05]. Starting with studying a well-known discharge, the ability of the used diagnostics to measure the radial electric field, as well as general plasma parameters, is shown.

The shape of the radial electric field profile is known to be important for the magnitude of the turbulent transport [HPD$^+$04, HDH$^+$99, II88, Ram05, VGM$^+$01]. Within the frame of this work the focus is on the impact of biasing on the radial electric field and other plasma parameters. Biasing in the WEGA stellarator is conducted in discharges, in which only little turbulence is found. This is done in order to investigate the effect of the biasing without the considerations on the effects

on the turbulence, which might obscure the results.

By comparing the results obtained from emissive probe measurements and high resolution Doppler spectroscopy, it is shown, that the ion motion in poloidal direction is governed by $\vec{E} \times \vec{B}$-drift. Heating power and neutral gas pressure scans are conducted to gain confidence in the results from these diagnostics.

When moving the biasing probe into the region of the confined plasma, the line-integrated density measured by the interferometer drops. In case of a limiter placed in the far SOL the density profile changes gradually with the probe position. In the case without limiter, the effect is not as clearly structured. In both cases of the limiter the shoulder of the density profile is found to be moving with the biasing probe position. The electron temperature profile is found to be sensitive to the probe position only in the case of a removed limiter. Comparing discharges with and without limiter in the scrape-off layer, the conclusion is drawn that the installed limiter dominates the SOL properties, which in turn largely determines the quality of the heating mechanism. The radial electric field decreases when the biasing probe is moved into the plasma. The effect is stronger when the probe is inserted deeper into the plasma. This behavior is also observed with normal limiter structures in other experiments.

Negative biasing of carbon probes as well as negative biasing using a large emissive tungsten biasing probe does not produce significant changes in the radial electric field, density or temperature profiles. This has been expected since the drawn current is small in case of the carbon probe. In case of the emissive probe the massive injection of thermally emitted electrons induces changes on the radial electric field and the plasma parameters. These changes are identified to originate of the emissive operation of the probe and are not caused by the applied bias. Other similar-sized experiments with more available heating power have reported to access the H-mode regime using an emissive biasing probe with even less current [KTT+06b]. This is interpreted that the used 14 kW of ECRH power are not nearly close to the H-mode power threshold. The poor conversion efficiency of the OXB-mode conversion process adds to this.

Biasing the carbon probes positively, it could be shown that using small biasing voltages ($U_{Bias} < +60$ V) the peak temperature at the edge of the plasma increases linearly with the biasing current. The plasma density in the edge decreases with biasing. An increase in the plasma potential is observed with biasing. The radial electric field increases proportional to the biasing current from the original value of $E_r \approx 40 \frac{V}{m}$ to about the threefold value of $E_{r,biased} \approx 120 \frac{V}{m}$. Similar observations

have been reported from other biasing experiments as well [WOB$^+$92, VGM$^+$01].

With biasing voltages exceeding $U_{Bias} = +60$ V, a transition to a hotter and more dense plasma state is observed. Depending on the discharge conditions, the plasma remains stationary or is alternating between two states on time scales exceeding than the confinement time by orders of magnitude. The plasma density of the newly found state is higher in the center and the electron temperature in the edge region increased significantly. The dense and warmer plasma state is thus referred to as high n_e-T_e state. For the first time temperatures higher than 20 eV have been established in low-field operation in WEGA. The biasing current is less in the high n_e-T_e state compared to the low n_e-T_e state.

The stored plasma energy in the high n_e-T_e state is larger by a factor of ≈ 2 compared to the low n_e-T_e state at the same biasing voltage. Compared to the unbiased plasma the increase in confined energy is $\approx 40\,\%$ for the high n_e-T_e state. This is comparable to the achievement of devices in which biasing has been used to reduce turbulence and where improved confinement regimes have been obtained. Looking at the power scaling of the biased plasma states reveals that the high n_e-T_e state scales with the heating power as the standard discharges do. This indicates that no significant improvement in confinement is achieved, but the mechanism is different. This is supported by the fact that a further reduction of turbulence is not observed. In contrast even an increase in the level of turbulence is found during biasing.

As the observed power scaling suggests a similar behavior as for the unbiased discharges with additional heating power, the heating mechanism is targeted as a possible candidate for the cause of the transition. The used OXB-mode conversion heating scheme in WEGA is rather complicated. Its efficiency depends on the edge parameters which are in turn depending on the absorbed heating power. With the help of two models the total absorbed microwave power can be determined and the conversion efficiency of the complex heating mechanism - a quantity otherwise hard to assess - can be estimated.

The models evaluate the particle and power balance based on the measured data. The particle balance is calculated using two different approaches, one based on the relevant atomic processes and a second one based on neoclassic theory. It is shown that both models give satisfactory agreement for the particle balance for large parts of the plasma. As far as the power balance is concerned, the microwave power is the single input power source, its power flux has to be balanced by the loss processes. The atomic model includes relevant atomic processes such as ionization,

recombination, calorimetric electrons, line radiation of neutrals and ions and energy transfer from electrons to ions [Hor04]. In addition also convection is treated now as the convective term is not to be neglected. The contribution of neutral and ionic line emission can be validated with bolometric measurements. The neoclassic model according to Hinton and Hazeltine [HH76] is used to verify that neoclassic energy flux is not contributing to the energy balance. Both models do not account for anomalous transport and are limited to rather low density and low temperature. Combining both models allows to balance the loss processes with the ECRH power deposition profile. This comparison yields the total power loss which can be related to the used ECRH power.

When describing biased discharges the inclusion of the biasing probe is required to fulfill the energy balance. A simple model for the biasing power deposition is motivated and introduced in this thesis. The resulting energy flux profile completes the power balance in case of biasing.

Comparing the biased plasma states, it is found that the change in the plasma parameters can be explained by an increased heating efficiency from $\eta_{mw} \approx 30\,\%$ - for the unbiased discharge and the low n_e-T_e state - to $\eta_{mw} \geq 80\,\%$.

Chapter 9

Outlook

The developed model allows the determination of a heating power conversion efficiency as shown in this thesis. This allows more detailed analysis of the complex OXB-mode conversion mechanism used for heating in the low magnetic field operation of WEGA with 2.45 GHz magnetrons. Parameter studies related to the conversion efficiency can be undertaken now and critical parameters can now be identified.

As the present model is limited to not to high temperatures and densities, the model needs to be extended in order to be applicable to the newly available high field operation using the existing magnetrons or the new 28 GHz gyrotron. Here much higher temperatures and densities are obtained. Extending the model to the high field case will likely require to include higher ionized ions and also charge exchange will become a more important process with higher temperature and density.

The model, the underlying mapping and validation routines will be beneficial in building up confidence in newly developed diagnostics for the high field operation. Here especially the ability to relate the probe data to the bolometer data will be useful.

Based on the work presented, work on a detailed model of the transition can be started. As the interaction of the magnetically confined electrons with the non-confined ions most likely needs to be taken into account for modeling the radial electric field. This will most likely require a fully three-dimensional treatment of the ions as well as the connection to the well-confined electrons in the three-dimensional magnetic field of the WEGA stellarator. This modeling is required in order to explain the formation of the observed radial electric field, coupling the electron and ion profiles. The advantage of WEGA is that most of the properties of both species

can be measured and the magnetic field is well known.

It will be interesting to see how the individual existing diagnostics will be pushed for fitting operation on Wendelstein 7-X. With the UHRS system being the first not-machine-operation-relevant diagnostic integrated into the Wendelstein 7-X prototype control system installed on WEGA, the future qualification for use on W7-X is only logical.

The CIS system, sharing its lines of sight with the UHRS system, is yet lacking detailed plans for future use. First of all, it will be transferred back to a finite DOF system to use its better time resolution and sensitivity, compared to the UHRS system, for measurements on WEGA. Possible future options include the operation in devices featuring relevant ion temperature range (10 - 100 eV) such as present day mid-size tokamaks. Testing the CIS system as an optical coherence tomography system is an interesting option for realization in the near future. The qualification of the CIS as Wendelstein 7-X divertor diagnostic is also possible.

That's all, folks!

Words of Gratitude

I would like to thank Prof. Wagner for taking me as PhD student and supervising my PhD work. I also want to thank Prof. John Howard for giving me the opportunity to work with the CIS and providing me with a lot of support, great components, foolproof software and tons of good ideas when dealing with the idea of the WEGA's CIS system. Sad enough no plasma data recorded with the system is shown in this thesis. I also want to thank Dr. Matthias Otte for allowing me to be a part of the WEGA team, for supervising my work, for proof reading the thesis and for taking up with all the administrative stuff. I want to thank Dr. Martin Schubert, Dr. George Warr and Dr. Daniel Andruczyk for encouraging me at times when things did not go as smooth as they where supposed to. I want to thank Dr. Daihong Zhang for processing the raw bolometer data and making it available to me. My gratitude also to Dr. Yuriy Podoba and Dr. H. Laqua for spending time discussing the impact of components, biasing and plasma profiles on the microwave heating scenario.

I want to thank my fellow PhD student Dr. Stefan Marsen for keeping the Langmuir probe system in operation and doing the major part of the Langmuir probe construction work. Thank you for showing me how to build decent probes and also thanks for helping me getting used to Linux. Thanks for the tons of good ideas, twists in electronics, proof reading this thesis and all other things I forgot to mention here.

My gratitude goes to Dieter Aßmus for spending days and days operating WEGA - almost missing the bus for his vacation trip - and dealing with a lot of the electrical engineering and remote sensing of various designs. I don't want to forget to thank Norbert Paschkowski, who did an outstanding job in designing, manufacturing and assembling all the components of various systems and vacuum adapters I so desperately needed. I want to thank Torsten Stange for all his support in the final part of this thesis, for providing a nice working atmosphere and an endless supply of cappuccino.

I want to thank Dr. Ralf König for his contribution to the spectroscopic work

125

Appendix A

Motion of Charged Particles

As a plasma consists of charged as well as uncharged particles due to its nature of being a very hot gas, it is useful to review the motion of single as well as ensembles of charged particles in external electro-magnetic fields. Here, time independent electro-magnetic fields will be covered. Neutrals are not influenced by electro-magnetic fields used for confining plasmas and can propagate freely except for collisions. Charged particles in a plasma exist, because the electron's thermal energy becomes large enough to leave the attracting potential of the positively charged nucleus of the neutral atom. The term *plasma* has been introduced by Langmuir and Tonks in the 1920ies.

If no additional fields are imposed onto the plasma, the charges are distributed in such fashion that the electric field in equilibrium is equal to zero. The plasma shields any local excess charge by a cloud of oppositely charged particles. The typical scale length for this cloud is called the Debye length λ_D and can be calculated from the plasma density n and temperature T to be

$$\lambda_D = \frac{\varepsilon_0 k_B T}{e^2 n}. \tag{A.1}$$

One can express the density of electrons and ions in a sufficiently large $(r > \lambda_D)$ sphere to be equal

$$\sum_{j=0}^{k} j \cdot n_{i,j} = n_e, \tag{A.2}$$

where k refers to the highest charge state of the appropriate species and j is the charge state of the ion. n_e and n_i represent electron and ion density. One refers plasmas as quasi-neutral if the characteristic length is larger than the Debye length.

A.1 Cyclotron Motion

Cyclotron motion, often also called gyration or gyro motion, describes the motion of electrons and ions perpendicular to the magnetic field. The Lorentz force presses charged particles into performing circular motion perpendicular to the magnetic field. Corresponding to the gyrating particle, it is called electron or ion cyclotron motion. The characteristic frequency of the cyclotron motion is called the electron or ion cyclotron frequency $\omega_{ce,ci}$. It can be expressed according to Larmor [Lar95]:

$$\omega_{ce,ci} = \frac{|q|\,B}{m_{e,i}}. \tag{A.3}$$

The characteristic scale of the gyration is called the electron or ion Larmor radius or gyro radius. It is defined as the ratio of velocity perpendicular to the magnetic field $v_\perp$ and the cyclotron frequency ω_c:

$$r_{Le,Li} = \frac{v_\perp}{\omega_{ce,ci}} = \frac{m_{e,i} \cdot v_\perp}{|q|\,B}. \tag{A.4}$$

The direction of movement of the particles parallel to the magnetic field can be parallel as well as anti-parallel to the magnetic field. Figure A.1 shows the motion with both particles having velocity parallel to the magnetic field. The direction of rotation with respect to the field line is different for ions and electrons due the sign of the charge. In the case displayed in figure A.1 the electrons rotate clockwise if looking into the direction of the field while the ions rotate counterclockwise.
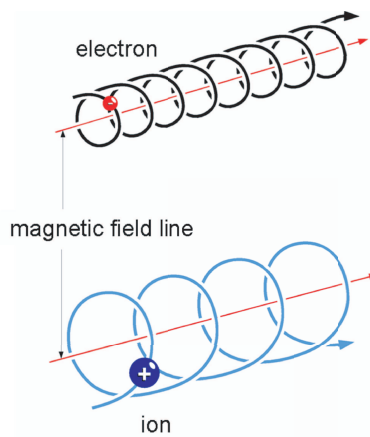
Figure A.1: Cyclotron motion of charged particles in an applied magnetic field.

A.2 Guiding Center Motion

In magnetized plasmas the detailed motion of a particle is often reduced to the trajectory of the so-called guiding center. This is reasonable for phenomena having characteristic mean free paths larger than the gyro radius. The guiding center's trajectory is obtained by averaging over the cyclotron movement

$$\frac{d\overrightarrow{R}}{dt} = \frac{\omega}{2\pi} \int\limits_{0}^{\frac{2\pi}{\omega}} \overrightarrow{v} \cdot dt. \tag{A.5}$$

This work always refers to the guiding center unless explicitly noted.

A.3 $\overrightarrow{E} \times \overrightarrow{B}$-Drift

When a charged particle is moving in a surrounding electric as well as an underlying magnetic field, the Lorentz force is implied on the particle. It can be represented as follows

$$\overrightarrow{F} = q \cdot \left(\overrightarrow{E} + \overrightarrow{v} \times \overrightarrow{B} \right). \tag{A.6}$$

This force results in a drift of the guiding center perpendicular to the magnetic and perpendicular to the electric field can be calculated to

$$\overrightarrow{v}_{\overrightarrow{E} \times \overrightarrow{B}} = \frac{\overrightarrow{E} \times \overrightarrow{B}}{B^2}. \tag{A.7}$$

In toroidal geometry the poloidal component of the velocity can be written as

$$v_\theta = \frac{E_r}{B_\varphi} + \frac{E_\varphi}{B_r}. \tag{A.8}$$

For use in WEGA the second term can be neglected as WEGA plasmas are produced using ECRH systems, which do not introduce momentum to the plasma.

A.4 Diamagnetic Drift

Treating single particles is not sufficient for explaining all motions of charged particles in a magnetic field. Instead, it is necessary to treat ensemble effects as well. In the following not only a single charged particle in a magnetic field is treated, but

an ensemble of equally charged particles is considered. The similarity of the plasma to the behavior of a fluid is the reason for the name of this method, magneto-hydrodynamics. The radial force balance equation for a charged fluid element, consisting of equally charged particles, in an underlying electric and magnetic field neglecting friction and collisions between the different species of particles of a plasma, can be derived from kinetic theory. A more detailed deduction of the equation is given in [Che77].

$$q_j n_j m_j \left(\frac{\partial \overrightarrow{v_j}}{\partial t} + (\overrightarrow{v_j} \nabla) \, \overrightarrow{v_j} \right) = q_j n_j \left(\overrightarrow{E} + \overrightarrow{v_j} \times \overrightarrow{B} \right) - \nabla p_j, \qquad (A.9)$$

where j refers to the species (electrons or ions). In the following the species will be treated independently and the species index is dropped as equation A.9 refers to any charged species. When considering events on time scales larger than that given by the electron cyclotron frequency the ratio

$$\frac{\frac{\partial \overrightarrow{v}}{\partial t}}{\left(\overrightarrow{E} + \overrightarrow{v} \times \overrightarrow{B} \right)} \approx \frac{\omega}{\omega_c} \approx 0 \qquad (A.10)$$

is close to 0 and the $\frac{\partial \overrightarrow{v}}{\partial t}$-term can be neglected for any species. This approximation is valid for all observations presented in this thesis. A similar approximation can also be made for the $(\overrightarrow{v} \nabla) \, \overrightarrow{v}$ term:

$$\frac{(\overrightarrow{v}_j \nabla) \, \overrightarrow{v}_j}{\left(\overrightarrow{E} + \overrightarrow{v}_j \times \overrightarrow{B} \right)} \approx \frac{r_{L,j}}{L} \approx 0, \qquad (A.11)$$

with L being a characteristic length of the plasma as for instance plasma size a. This is a good approximation for electrons, but not necessarily for ions as this ratio can reach the order of 0.1 or even higher for low magnetic field operation with argon. The impact of the magnetic field on argon ions in the low-field operation can be found in chapter 4.1.1.

Combining A.10 and A.11 results in A.9 taking the following form:

$$0 = qn \left(\overrightarrow{E} + \overrightarrow{v} \times \overrightarrow{B} \right) - \nabla p. \qquad (A.12)$$

The equation can be multiplied with $\times \overrightarrow{B}$ and sorted for $\overrightarrow{v}$ in order to derive the

velocity to be:

$$\overrightarrow{v} = \frac{\overrightarrow{E} \times \overrightarrow{B}}{B^2} + \frac{\nabla p \times \overrightarrow{B}}{qnB^2} = \overrightarrow{v}_{\overrightarrow{E} \times \overrightarrow{B}} + \overrightarrow{v}_{diam}. \tag{A.13}$$

The first term is the known $\overrightarrow{E} \times \overrightarrow{B}$- drift introduced in the single particle drift picture before. The second term is called diamagnetic drift,

$$v_{diam} = \frac{\nabla p}{q \cdot n \cdot B}, \tag{A.14}$$

where $p = p_i + p_e$ is the plasma pressure and q the electric charge of the individual particle. Depending on the ion pressure gradient the ion diamagnetic drift is into or against the direction of the $\overrightarrow{E} \times \overrightarrow{B}$-drift. ∇p can be expressed by means of temperature and density as follows:

$$\nabla p = \nabla (nT). \tag{A.15}$$

An approximation for n_i needs to be made as, presently, there is no way of determining n_i directly in WEGA. As measurements show no detectable line radiation from doubly charged ions, a reasonable approximation for WEGA plasmas with sufficiently small heating power (typically $\lesssim 14$ kW) is $n_i = n_e$. This leads to the following simplification

$$\nabla p_i \propto \nabla (n_e \cdot T_i). \tag{A.16}$$

This results in the ion diamagnetic drift, as utilized in this thesis, to be

$$v_{i,diam} = \frac{\nabla (n_e \cdot T_i)}{q \cdot n_e \cdot B}. \tag{A.17}$$

A.5 Additional Drifts

In a more generalized approach the force balance equation of a force $\vec{K}$ exerted on a charged particle in a magnetic field can be written as

$$\overrightarrow{F} = m\frac{d\overrightarrow{v}}{dt} = \overrightarrow{K} + q\left(\overrightarrow{v} \times \overrightarrow{B}\right). \tag{A.18}$$

Considering only motion perpendicular to the underlying magnetic field (drift motions), the equation can be solved for v, then also called $\vec{v}_D$, which can be expressed

as

$$\overrightarrow{v}_D = \frac{\overrightarrow{K} \times \overrightarrow{B}}{qB^2}. \tag{A.19}$$

A.5.1 ∇B- Drift

Introducing for instance a spatially inhomogeneous magnetic field having a magnetic field gradient $\nabla \vec{B}$, the corresponding drift due to the magnetic field gradient can be calculated using $\overrightarrow{K}_{\nabla \vec{B}} = -\mu \nabla \overrightarrow{B}$ to

$$v_{\nabla \vec{B}} = -\mu \frac{\nabla \overrightarrow{B} \times \overrightarrow{B}}{qB^2}. \tag{A.20}$$

This can be expressed by

$$\left| v_{\nabla \vec{B}} \right| = \left| \frac{q \cdot r_L^2}{2 \cdot m} \nabla B \right| = \left| \frac{m \cdot v_\perp^2}{2 \cdot e \cdot B_0^2} \nabla B \right|. \tag{A.21}$$

A.5.2   Curvature Drift

Drift motion can also be caused by a curved magnetic field. The corresponding force $\overrightarrow{K}_{curv}$ can be written as

$$\overrightarrow{K}_{curv} = m v_\parallel^2 \frac{\overrightarrow{R}_c}{R_c^2}, \tag{A.22}$$

with $\vec{R}_c$ being the radius of curvature. Combining equations A.22 and A.19 this leads to

$$\overrightarrow{v}_c = \frac{m \cdot v_\parallel^2}{q \cdot R_c^2 \cdot B_0^2} \left(\overrightarrow{R}_c \times \overrightarrow{B} \right). \tag{A.23}$$

Combining equations A.23 and A.20 and approximating $\nabla \vec{B}$ using $\frac{B}{R_c} \approx |\nabla \overrightarrow{B}|$ one gets the drift motion of a curved and inhomogeneous magnetic field to be

$$v_{Drift} = v_{curv} + v_{\nabla B} = \frac{m}{q} \cdot \left(v_\parallel^2 + \frac{1}{2} \cdot v_\perp^2 \right) \cdot \frac{\overrightarrow{R}_c \times \overrightarrow{B}}{R_c^2 B_0^2}. \tag{A.24}$$

This can be approximated by introducing the thermal velocity $v_{th} = \sqrt{\frac{kT}{m}}$ by

$$v_{Drift} = \frac{e}{q} \frac{r_L}{R_c} \cdot v_{th}. \tag{A.25}$$

The poloidal ion rotation in WEGA can consist of $\vec{E} \times \vec{B}$-drift and ion diamagnetic drift as ∇B and curvature drift are eliminated by finite rotational transform. Both

components can be derived from probes and spectroscopy and are compared to the spectroscopically measured poloidal rotation in figure A.2.
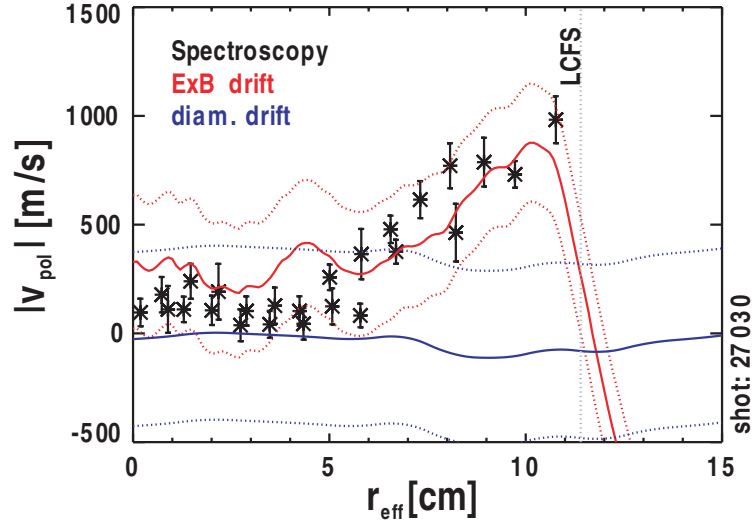
Figure A.2: Poloidal ion rotation as measured spectroscopically (stars), $\vec{E} \times \vec{B}$-drift (red line) and diamagnetic drift (blue line) from probe measurements; error for probe-based measurements is represented by dotted lines.

As can be seen the contribution of the diamagnetic drift is small compared to the $\vec{E} \times \vec{B}$-drift and will be neglected in this thesis. The radial electric field can be determined spectroscopically to be

$$E_r = v_\theta \cdot B_\varphi. \tag{A.26}$$

This will be used frequently during this thesis to derive the radial electric field from spectroscopic measurements. A separate display of the poloidal ion flow velocity will usually not be shown as the relation in equation A.26 is simple.

Appendix B

CCD camera specific issues

This section will deal with issues related to CCD cameras.

The camera used for the ultra-high resolution spectrometer utilizes a back-illuminated frame-transfer CCD chip that is cooled by a multi-stage water-cooled Peltier element. In a brief section, the camera will be characterized and important terms dealing with operating such a camera will be explained.

B.1 Frame Transfer, Blurring & Shutter

A frame transfer camera, as the employed Roper MicroMax, has a distinct difference to regular CCD cameras. The area of the chip is divided into two distinct areas, the image area used for integrating the light and the storage area. The storage area is covered with an opaque mask providing an intermediate storage to the accumulated charges. The frame transfer process rapidly shifts the image from the image area of the chip to the storage area. The image is then read from the covered area while the top half is continually exposed to light.

The camera can be operated in different operational modes as well. In full-chip mode an image is acquired by using the full image area the chip and every pixel line as an individual channel. This is practically the more rare mode as the camera is usually operated in hardware-binned mode combining multiple pixel lines to a single channel. This has two reasons: First being the readout time of $\sim 2.7\,\text{s}$ and secondly, with reading out every pixel line on its own one adds readout noise. In binned operation the readout noise occurs only once - when the binned channel is read. Typically, the cameras are used either with a binning of 12 to 14 lines combined to a single channel, or at 3 - 4 pixel lines per binned channel. The later has the disadvantage of having a 4- to 4.5-fold readout noise compared to the first setting.

The detailed binning table can be found in table B.1.

LOS #	fiber #	lines	r_{eff} [cm]
1	26	6-19	10.8
2	27	23-36	10.0
3	28	41-54	9.1
4	29	59-71	8.3
5	30	74-87	7.5
6	31	92-104	6.7
7	32	112-122	6.0
8	33	128-138	5.2
9	34	144-157	4.5
10	35	161-172	3.7
11	36	176-189	2.9
12	37	194-205	2.2
13	38	211-223	1.4
14	39	229-240	0.8
15	40	245-257	0.0
16	41	262-274	0.8
17	42	279-290	1.4
18	43	296-307	2.2
19	44	314-324	2.9
20	45	331-341	3.7
21	46	351-362	4.5
22	47	365-375	5.2
23	48	382-393	6.0
24	49	399-410	6.8
25	50	414-426	-
26	51	432-443	8.3
27	52	450-460	8.9
28	53	483-493	-
29	54	499-506	-

Table B.1: Employed binning for 29 channels (fiber from channel 25 turned blind, channels 28 & 29 intersect the port structure) during the final campaign.

An additional difference to common cameras is that frame transfer cameras are usually not equipped with a shutter. The shutter function is mimicked by the storage area. Having the advantage of the camera collecting light continuously, allows a higher frame rate. This has to be taken care of when operating the camera with frame rates about the size of the frame transfer time. Here, blurring of the image occurs when the image is transferred to the covered region of the chip. The conditions met in WEGA allow this effect to be neglected as the exposure time of the camera is several orders of magnitude larger than frame transfer time. The

frame transfer time is in the order of a few s, where the exposure time typically 1s. The exposure time is determined by the amount of light reaching the CCD cam at the back of the high resolution spectrometer.

B.2   Linearity

In order to interpret the signals obtained by the CCD camera properly, one has to ensure the linear behavior of the camera. The camera is specified to have a linear full well depth of ∼120,000 electrons before an individual pixel saturates. The readout line has a linear full well capacity of ∼200,000 electrons. The actual dynamic range would be higher, but all above this value will be non-linear.

In order to obtain the data (intensity), the accumulated charge has to be converted to an intensity value, typically given in counts. The conversion factor between charge and intensity is called the read noise and has the units $\frac{e^-}{count}$. The read noise depends on the operating cycle of the attached ADC converter. The Roper Micro-Max CCD ADC can be operated at 1 MHz with a read noise of 8 - 10 $\frac{e^-}{count}$ or 100 kHz with read noise of 4-5 $\frac{e^-}{count}$.

One has to note that the maximum linear range of the CCD camera is limited by two different bottle necks depending on the operational mode. One bottle neck is the linear full well capacity of an individual pixel leading to a maximum dynamic range of ∼15,000 counts (in 1 MHz mode, no binning), respectively 30,000 (in 100 kHz mode, no binning). The other is the full well capacity of the readout line ∼25,000 counts (1 MHz mode, binning factor ≥ 2), respectively 50,000 counts (100 kHz mode, binning factor ≥ 2). In case of the usual settings used during this thesis the limit is imposed by the readout line in 100 kHz mode, so a maximum value of 50,000 counts has not to be exceeded. A linearity study for different binnings is conducted using a white light source. A typical result is shown in figure B.1.
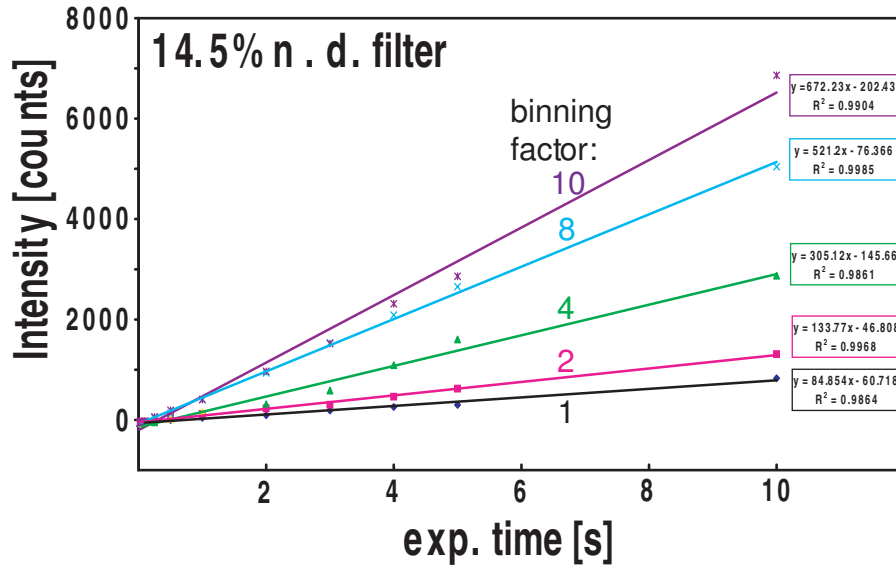
Figure B.1: Linearity of the Roper MicroMax back-illuminated frame transfer CCD camera (SN:D1200100); binning factors ranging from 1 to 10; neutral density filter with 14.5% transmission placed in front of the fiber bundle to reduce intensity of the laser (Picarro CYAN 488nm) used in this calibration; exposure times range from 1 ms to 10 s.

The camera exhibits a linear behavior over the exposure time range. The deviation of the individual points from the line is the size of the average noise level. The slope follows the binning factor linearly.

B.3   Saturation Induced Effects

When a CCD chip is largely overexposed, the camera can produce images that seem reasonable at first, but are hard to explain. The described effects are common to all, but specially corrected cameras, which have measures against them. To make it worse, some of these effects suggest to happen at light levels significantly lower than the saturation value. Especially, in combination with the high resolution spectrometer noticing these can be quite tricky, as the image produced can look like a reasonable spectrum.

The most common effect observed, when a CCD chip is exposed to high light levels, is called blooming and labels the spilling of charges of a pixel to its neighbors. The more electrons accumulate in a pixel, the more the linear relation between light intensity and signal degrades. The reason for this is the trapping potential filled with the already accumulated electrons becoming less likely to capture another electron. This leads to a decreased sensitivity of the pixel. Instead of being captured at

the pixel, the electron moves to one of the pixel's neighbors and is trapped there. Blooming typically causes white blobs or even lines on the image depending on the condition of the neighboring pixels. Blooming can be prevented by one of two means. First way to avoid blooming is called clocked anti-blooming. Here, the clock voltage phases of adjacent pixels are alternately switched. This forces excess charges to flow into the barrier between the Si and SiO layers, confining them there. When the clock phases are switched, the confined charges become detrapped and are lost, while the accumulated charge is retained. The other option is to include charge drains into the CCD's architecture, running in between the pixels, draining excess charges. The disadvantage of such cameras is the reduced efficiency, as the charge drains require space which cannot be used. Charge drains can be useful though, if the light level on the camera varies over many orders of magnitude. A less common type of blooming is called well-braking and refers to certain areas of the camera being spilled with charge and successive confining potential destruction due to the created avalanche. This happens if the pixel as well as its neighbors are highly over-exposed. The danger of well-braking lies in the potential of generating spectra looking reasonable, except for showing a ghost line seemingly separated from the original line.
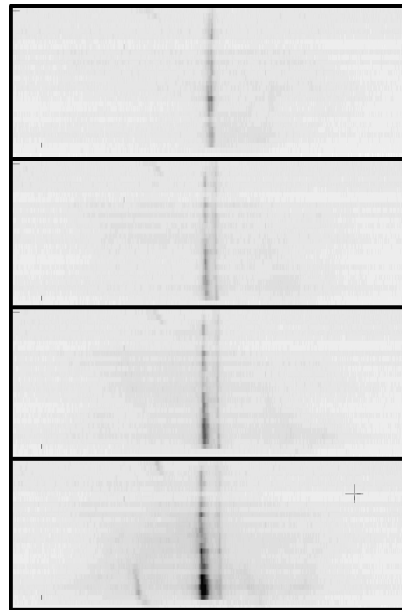
Figure B.2: Movement of a ghost line when adjusting the width of the entrance slit.

Well-braking can suggest to happen way below the maximum dynamic range as the affected pixels show values near the background noise level. A typical behavior of well-braking is displayed in figure B.2. One can see the ghost line (left) approaching the original line when the entrance slit to the spectrometer system is reduced.

B.4   UHRS Camera Specifications

Model	Roper MicroMAX:512 BFT
Number of pixels	512 (H) x 512 (V)
Pixel size	13 m x 13 m
Spectral response	340 nm - 900 nm
Quantum efficiency at 600nm	85 %
Binning	full frame or via defined ROIs
Readout bits & A/D converter	16 bits
Gain factors (H/M/L)	1.1/1.8/3.7
Linear full well (typical)	$<$125k (200k) e$^-$ for single pixel (2x2 pixels)
Read noise @ 1MHz / 100kHz	4.76 / 2.98 e$^-$ rms
Dark current (-45°C)	$<$7.7 e$^-$/p/s

Table B.2: Camera details (as provided by the manufacturer)

Appendix C

Comparison of the Magnetron Sources

The following part of the appendix will compare the 6 kW discharges produced with different magnetron sources. as the magnetron sources are placed at different toroidal positions, this allows insight to the dependency of the heating system on the exact magnetic geometry. The 6 kW source is placed at a toroidal angle of $\varphi = 288°$, the 20 kW magnetron is located at $\varphi = 324°$. In contrast to the manually matched 6 kW source and transfer line, the 20 kW source has an automated matching system is available. Time traces of line-integrated density and neutral line emission for a 6 kW discharge, as shown in figure C.1, are almost identical for both magnetrons.
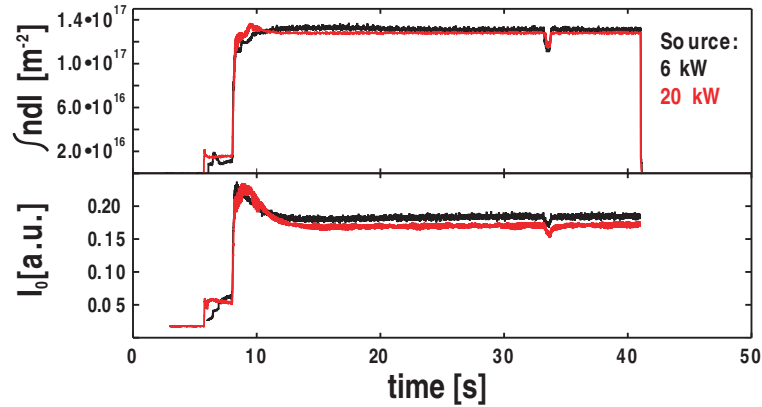
Figure C.1: Time traces of line-integrated density and neutral line emission for a 6 kW discharge with different heating sources.

When looking at the plasma parameter profiles of plasma produced with the two different heating systems, a general trend is observed. The 20 kW source seems to produce more broadened profiles than the 6 kW source when looking at density and

temperature profiles (shown in figure C.2).
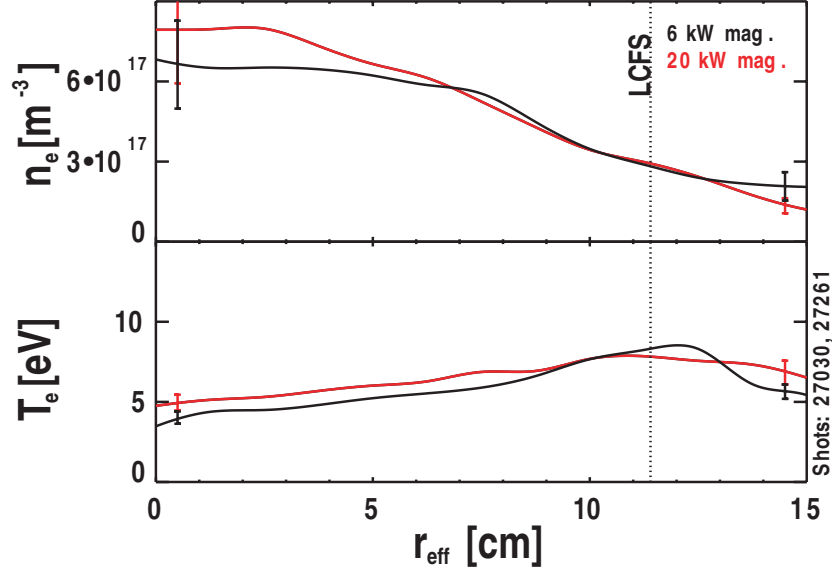
Figure C.2: Density and temperature profiles from probes for different heating sources at 6 kW input ECRH power.

This difference is small and vanishes within the error bars, but is systematic to all measurements. Whether this is simply due to a more robust plasma compared to the plasma produced with the 6 kW source could not be verified. A difference is possible as the position of the magnetrons with respect to the magnetic field are different. The measured plasma potential profiles of the 20 kW sources are not as stable as the ones measured using the 6 kW source, as is displayed in figure C.3.
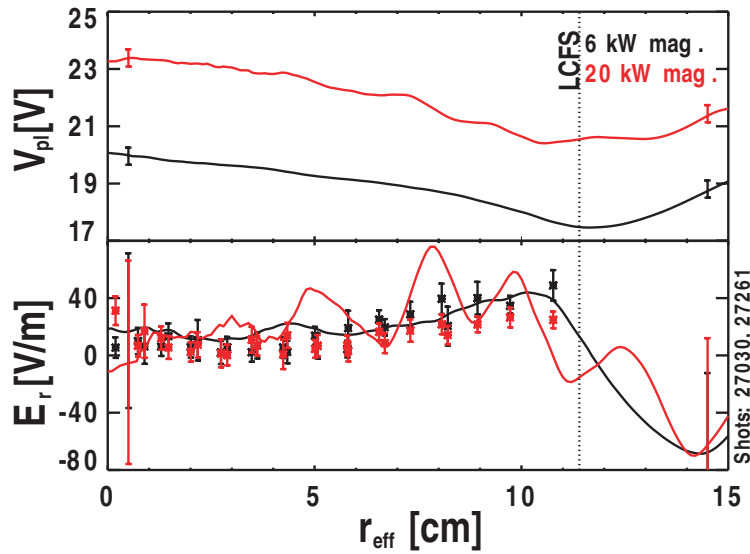
Figure C.3: Plasma potential and radial electric field from probes & spectroscopy for different heating sources with 6 kW of input ECRH power.

When directly comparing the confined energy, using the 6 kW source seems to be lower compared to the 20 kW source, as can be seen in figure C.4.
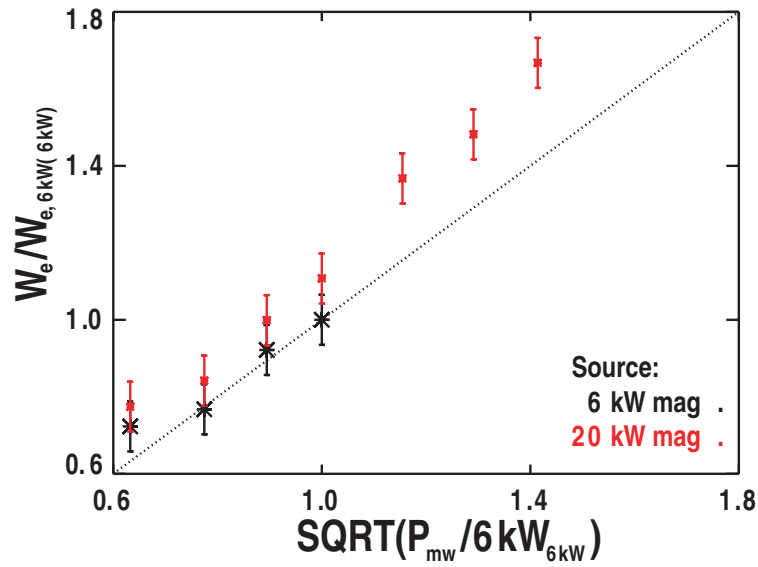
Figure C.4: Scaling of the confined energy of both magnetron sources (black - 6kW, red - 20 kW) ; $W_{e,6}\text{kW}(6\text{ kW}) = 0.14\,\text{J}$.

As the 20 kW source cannot be operated stably at reduced power (see chapter 5.2), respectively with full power due to the vacuum window braking, the 6 kW source is used for studies in this thesis. It can be operated at its maximum power producing stable plasma profiles and the SNR for the spectroscopic measurement is adequate.

Appendix D

Support to the Atomic Model

D.1   Rate Coefficients

The atomic model uses rate coefficients for ionization and recombination according to [LSS02, Vor97] when considering the particle balance. Both rate coefficients are temperature dependent, but depend weakly on density. The temperature characteristic of the rate coefficients is shown in figure D.1.
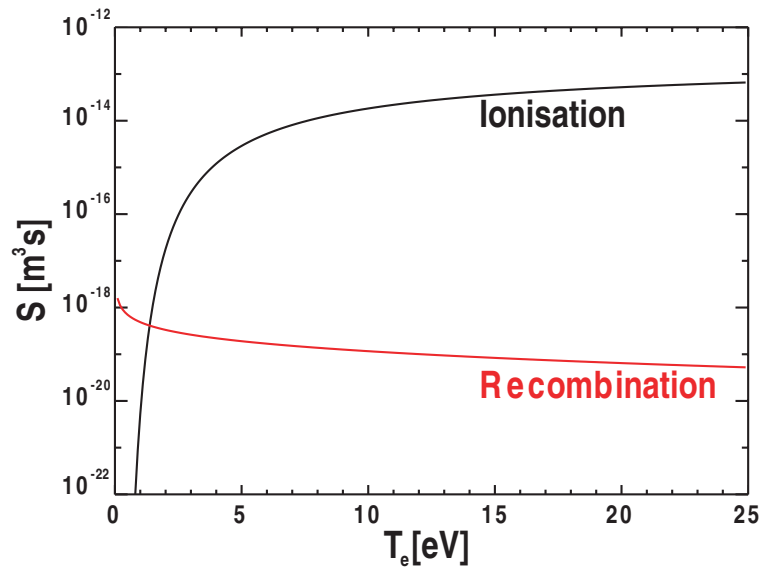
Figure D.1: Ionization and recombination rate coefficients for argon as a function of the plasma temperature.

When looking at the energy balance, the role of the rate coefficients is taken over by energy rate coefficients. As in [Hor04] the energy rate coefficients are used according to [LSS02]. The temperature dependence of the energy rate coefficients for the different processes is displayed in figure D.2.
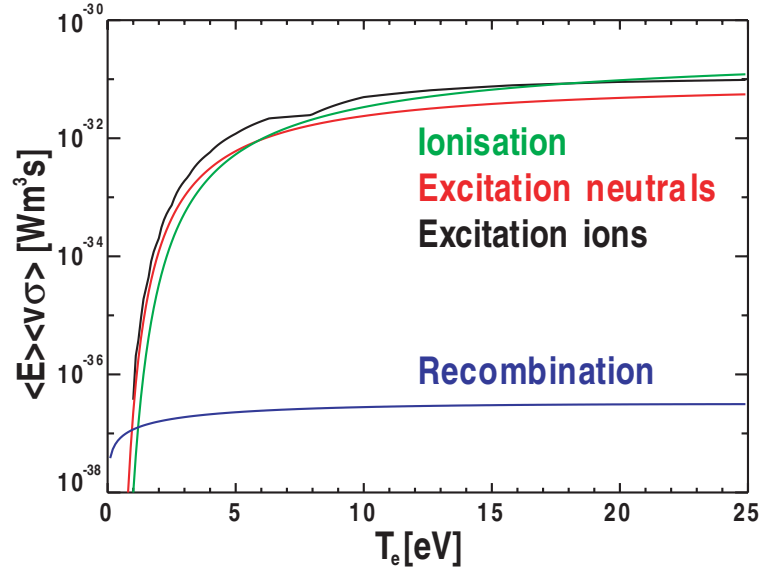
Figure D.2: Energy rate coefficients for relevant atomic processes as function of the electron temperature.

D.2 Particle Balance

The particle balance is dominated by ionization as particle source. Recombination can be neglected as is shown in figure D.3.
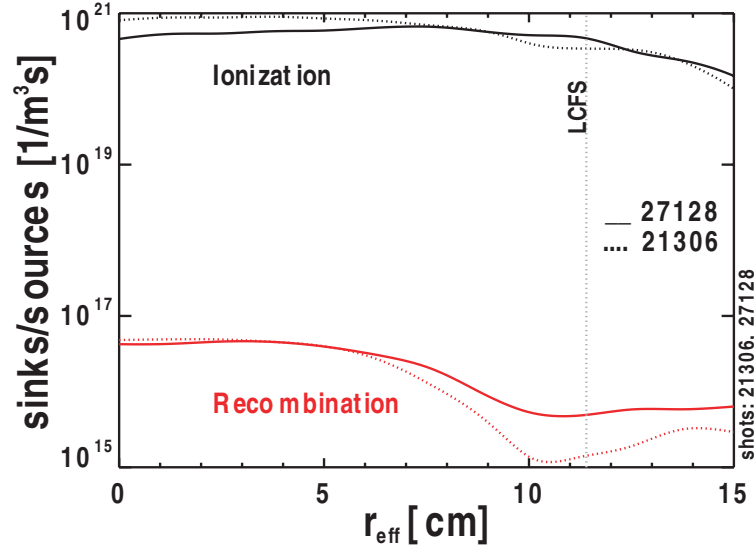
Figure D.3: Particle sources (black) and sinks (red) for the reference discharge without limiter installed (solid lines) and with limiter installed (dotted lines) and placed at BPtip = 9.8 cm.

    The cross section for other processes are smaller than the recombination rate

coefficient.

Appendix E

Support to the Neoclassical Model

E.1   Fluctuations

As stated in chapter 7, the contributions of transport caused by fluctuations are neglected in the models used for modeling. This assumption is based on two arguments: First and foremost, for large parts of the plasma the level of fluctuations is small as is displayed in the top part of figure E.1 for the unbiased probe placed at $r_{eff} = 9.8$ cm. The lower graph shows a wider radial part of the profile showing turbulent character.
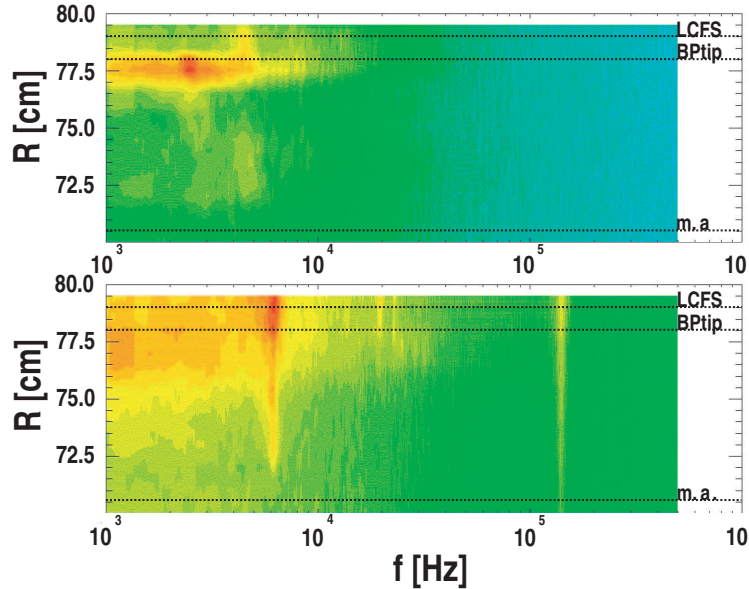
Figure E.1: Power spectral density of floating potential measurements obtained over a radial scan using Langmuir probes for $U_{Bias} = 0$ V (top) and $U_{Bias} = +200$ V (bottom) with biasing probe placed at $r_{eff} = 9.8$ cm; LCFS, magnetic axis and BPtip are marked by horizontal dashed lines.

The HH model is expected to underestimate the energy and particle flux in the region where fluctuations are present. The correct fluxes would have to incorporate the flux caused by turbulence

E.2   Collisionality

The HH model is used to model large aspect-ratio tokamaks in the collisional and plateau regime having circular flux surface cross sections. WEGA argon plasmas in low field operation fall into the Pfirsch- Schlüter- (collisional) regime for the plasma center and the plateau regime for the plasma edge. As the HH model has originally been developed for modeling tokamaks and the stellarator features start becoming important at low $\left(\frac{\nu_{ei}}{\nu_p} \lesssim \varepsilon^{3/2}\right)$ collisionality, the approximation is considered to be, at least, in the correct order of magnitude. In a tokamak three different collisionality regimes exist. These are Pfirsch- Schlüter (or collisional) regime, plateau regime and banana regime. The typical diffusion coefficient as a function of the collision frequency of electrons and ions is shown in figure E.2.
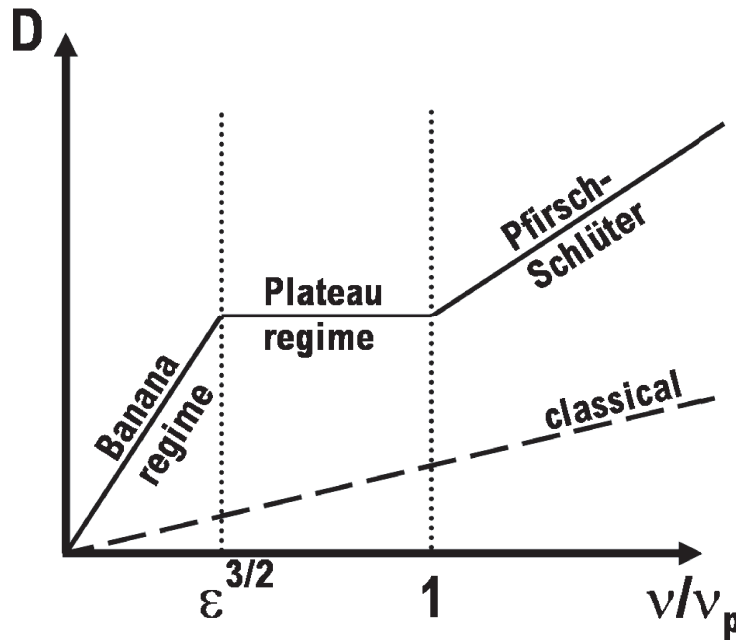
Figure E.2: Collisionality regimes in a tokamak (sketch)

In WEGA the ratio of the electron-ion collision frequency compared to the values of the plateau collisionality is typically $\frac{\nu_{ei}}{\nu_p} \geq 1$. The collisionality profile of different discharges is displayed in figure E.3.
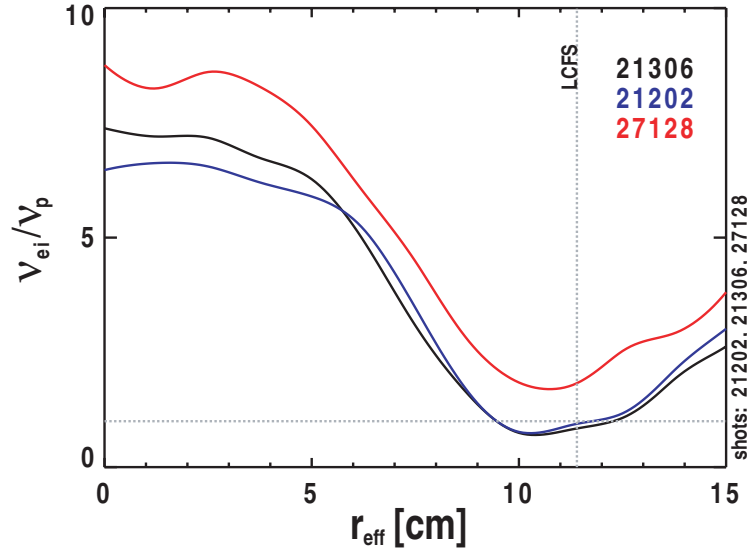
Figure E.3: Collisionality for typical WEGA argon plasma produced in low field operation for discharges with limiter installed (black - BPtip = 9.8 cm, blue - BPtip = 8.2 cm) and without limiter installed (red - BPtip= 9.8 cm).

Diffusion is mostly in the collisional or Pfirsch- Schlüter regime with only the edge reaching the plateau value.

E.3 Diffusion Coefficients

In contrast to [Hor04], the particle flux in this thesis is not attributed to the density gradient only, via $\Gamma_e = -D_{exp} \nabla n_e$, but is calculated from neoclassical theory as described in chapter 7.2. The diffusion coefficient derived by Horvath showed an increase to the edge of the plasma.
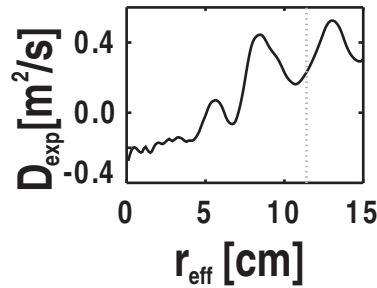
Figure E.4: Diffusion coefficient derived according to Horvath for the reference discharge.

For the NC model, the diffusion coefficients show a centrally peaked profile for the D_{X1} coefficients and a hollow D_{12} profile, as is shown in figure E.5.
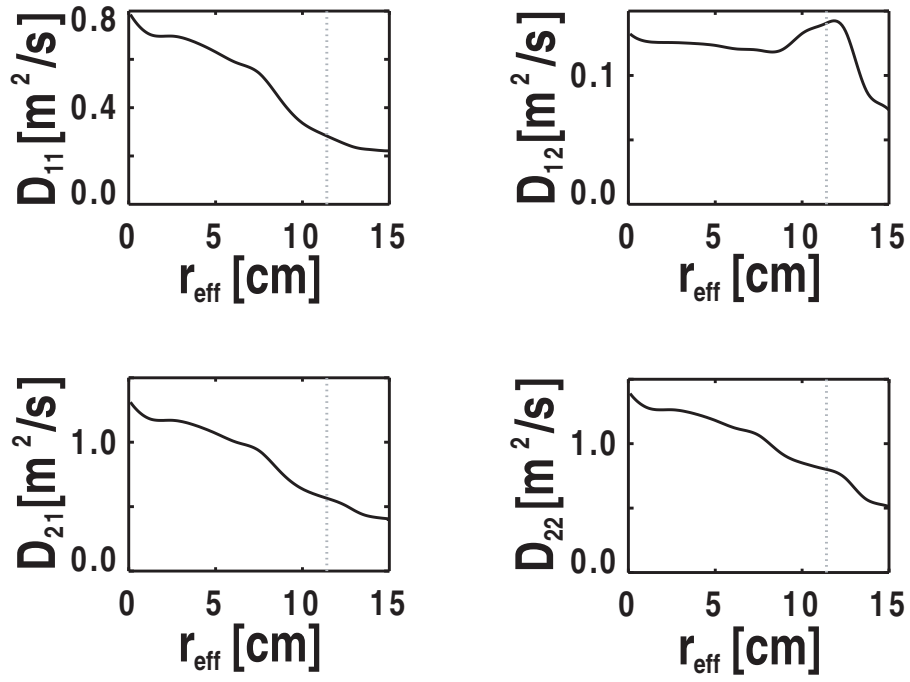
Figure E.5: Diffusion coefficients according the HH model for the reference discharge; the position of the LCFS is indicated by the dotted line.

As the description is more complete, relating the observed flux to the full set of thermodynamic forces, this approach is seen as an improvement of the approach presented in [Hor04].

Appendix F

List of Abbreviations

Unless otherwise noted the symbols used in equations refer to the following quantities:

symbol	description / quantity
a	minor vessel radius
A_{rel}	relative mass
A_R	Richardson's constant
$B, (\vec{B})$	magnetic field (vector)
c	speed of light ; $2.997925 \cdot 10^8 \frac{\text{m}}{\text{s}}$
χ	poloidal magnetic flux
e	elementary charge ; $1.6022 \cdot 10^{-19}\text{C}$
$E, (\vec{E})$	electric field (vector)
ε	inverse aspect ratio ; $\varepsilon = \frac{a}{R}$ (for WEGA: $\varepsilon \approx \frac{1}{6}$)
ε_0	permeability of free space ; $8.85418782 \cdot 10^{-12} \frac{\text{As}}{\text{Vm}}$
Γ	particle flux
h	Planck constant ; $6.62606885 \cdot 10^{-34}\,\text{Js}$
$\hbar$	reduced Planck constant (Dirac constant); $\hbar = \frac{h}{2\pi}$
I	electric current
I_0	light intensity
ι	poloidal angle between two passes of field line of a $\varphi = const.$ surface
ι	rotational transform
j	electric current density
k_B	Boltzmann constant ; $1.38 \cdot 10^{-23} \frac{\text{J}}{\text{K}}$
l	poloidal periodicity of a classical stellarator
λ	wavelength of light

153

$\ln \Lambda$	Coulomb logarithm
m	mass or toroidal periodicity of a classical stellarator
μ_B	Bohr magneton ; $\mu_B = \frac{e\hbar}{2m_e}$
n_e, n_i	electron / ion density
ν	frequency of light
φ	toroidal angle in toroidal coordinates
Φ	toroidal magnetic flux
P_{mw}	microwave power
Ψ	flux function
q	electric charge in units of e
Q	energy flux
r	minor radius in toroidal coordinates
r_{eff}	effective radius
R	major radius in toroidal coordinates or electrical resistance
$\vec{R}$	position vector
S	surface area (of probe)
$S_{ion,res}$	ionization / recombination cross section
σ_{SB}	Stefan- Boltzmann constant ; $5.67 \cdot 10^{-8} \frac{\mathrm{W}}{\mathrm{m^2 K^4}}$
$\tau_{E,p}$	energy / particle confinement time
θ	poloidal angle in toroidal coordinates
T_e, T_i	electron / ion temperature
U	electric potential
$V_{fl,pl}$	floating / plasma potential
W_a	work function of probe material
ω_c	angular frequency of cyclotron motion
Z_{eff}	effective charge of ions

Bibliography

[ABR57]   ALLEN, J E. ; BOYD, R L F. ; REYNOLDS, P: The Collection of
            Positive Ions by a Probe Immersed in a Plasma. In: *Proceedings
            of the Physical Society. Section B* 70 (1957), Nr. 3, S. 297–304

[BGK+00]   BALDZUHN, J ; GIANNONE, L ; KICK, M ; MCCORMICK, K ;
            TEAM, W7-AS: Optimized confinement discharges in the stel-
            larator W7-AS. In: *Plasma Physics and Controlled Fusion* 42
            (2000), Nr. 4, S. 463–487

[Boi92]   BOILEAU: Tokamak Plasma Biasing / Report on the IAEA Tech-
            nical Committee Meeting Sept 1992. 1992. – Forschungsbericht

[BSN93]   BERGMANN, L. ; SCHAEFER, C. ; NIEDRIG, H.: *Lehrbuch der
            Experimentalphysik: Bd.3 Optik.* Berlin; New York : de Gruyter,
            1993

[Che77]   CHEN, Francis F.: *Introduction to Plasma Physics.* Plenum Press,
            New York & London, 1977

[Che01]   CHEN, Francis F.: Langmuir probe analysis for high density plas-
            mas. In: *Physics of Plasmas* 8 (2001), Nr. 6, S. 3029–3041

[Che03]   CHEN, Francis F.: Lecture Notes on Langmuir Probe Diagnostics.
            In: *Mini-Course on Plasma Diagnostics, IEEE-ICOPS meeting,
            Jeju, Korea*, 2003

[Chu04]   CHUNG, J.: *Time Resolved 2D Doppler Imaging of Ion Dynamics*,
            Ernst- Moritz- Arndt- Universität Greifswald, Diss., 2004

[Der16]   DERR, L.: *Photography for Students of Physics and Chemistry.*
            The Macmillan Company, London, 1916

[FBS86]   FALK, D. ; BRILL, D. ; STORK, D.:   *Ein Blick ins Licht.*
                Birkhäuser Verlag Springer Verlag, 1986

[Fin02]   FINK, M.: *Untersuchung der Fluktuationen des Plasmapotentials*
                mit emissiven und nichtemissiven Sonden, Ernst- Moritz- Arndt-
                Universität Greifswald, Diplomarbeit, 2002

[FIS$^+$98]   FUJISAWA, A ; IGUCHI, H ; SANUKI, H ; ITOH, K ; ITOH, S-I
                ; OKAMURA, S ; MATSUOKA, K ; HAMADA, Y: Electric field
                bifurcation and transition in the core plasma of CHS. In: *Plasma*
                Physics and Controlled Fusion 40 (1998), Nr. 5, S. 627–630

[FTK$^+$98]   FUKUDA, T ; TAKIZUKA, T ; KAMADA, Y ; TSUCHIYA, K ; MORI,
                M ; THE JT-60 TEAM: Non-dimensional threshold scaling of edge
                plasma quantities in JT-60U. In: *Plasma Physics and Controlled*
                Fusion 40 (1998), Nr. 5, S. 827–830

[GAAT02]   GERHARDT, S. ; ALMAGRI, A. F. ; ANDERSON, D. T. ; TAL-
                MADGE, J. N.: Initial Results From Biased Electrode Experi-
                ments in HSX. In: *The 13th International Stellarator Workshop*
                Proceedings, 2002

[GC98]   GROEBNER, R J. ; CARLSTROM, T N.: Critical edge parame-
                ters for H-mode transition in DIII-D. In: *Plasma Physics and*
                Controlled Fusion 40 (1998), Nr. 5, S. 673–677

[Gou70]   GOURDON, C.: Programme optimise de calculs numerique dans
                les configurations magnetique toroidales / CEN, Fontanay aux
                Roses. 1970. – Forschungsbericht

[HDH$^+$99]   HRON, M. ; DURAN, I. ; HORACEK, J. ; JAKUBKA, K. ; KRYSKA,
                L. ; STÖCKEL, J. ; ZACEK, F.: Structure of Edge Turbulence at
                Plasma Polarization on the CASTOR Tokamak. In: *Proceedings*
                of the 26th EPS Conference on Controlled Fusion and Plasma
                Physics, 1999

[HH76]   HINTON, F. L. ; HAZELTINE, R. D.: Theory of plasma transport
                in toroidal confinement systems. In: *Rev. Mod. Phys.* 48 (1976),
                Apr, Nr. 2, S. 239–308

[Hin91]   HINTON, F. L.: Thermal confinement bifurcation and the L- to
             H-mode transition in tokamaks. In: *Physics of Fluids B: Plasma
             Physics* 3 (1991), Nr. 3, S. 696–704

[HLLW04]   HORVATH, K. ; LINGERTAT, J. ; LAUX, M. ; WAGNER, F.: Lang-
             muir Probe Measurements in the WEGA Stellarator. In: *Contri-
             butions to Plasma Physics* 44 (2004), Nr. 7-8, S. 650–655

[Hor04]   HORVATH, Kinga: *Charaterisation and Optimisation of the
             WEGA Plasmas*, Ernst- Moritz- Arndt- Universität Greifswald,
             Diss., 2004

[How99]   HOWARD, J.: Modulated optical solid-state spectrometer appli-
             cations in plasma diagnostics, AIP, 1999, S. 368–371

[HPD+04]   HIDALGO, C ; PEDROSA, M A. ; DREVAL, N ; MCCARTHY, K J.
             ; ELISEEV, L ; OCHANDO, M A. ; ESTRADA, T ; PASTOR, I ;
             ASCASÍBAR, E ; CALDERÓN, E ; CAPPA, A ; CHMYGA, A A. ;
             FERNÁNDEZ, A ; GONÇALVES, B ; HERRANZ, J ; JIMÉNEZ, J A. ;
             KHREBTOV, S M. ; KOMAROV, A D. ; KOZACHOK, A S. ; KRUP-
             NIK, L ; LÓPEZ-FRAGUAS, A ; LÓPEZ-SÁNCHEZ, A ; MELNIKOV,
             A V. ; MEDINA, F ; VAN MILLIGEN, B ; SILVA, C ; TABARÉS, F
             ; TAFALLA, D: Improved confinement regimes induced by limiter
             biasing in the TJ-II stellarator. In: *Plasma Physics and Controlled
             Fusion* 46 (2004), Nr. 1, S. 287–297

[Ida98]   IDA, Katsumi: Experimental studies of the physical mechanism
             determining the radial electric field and its radial structure in a
             toroidal plasma. In: *Plasma Physics and Controlled Fusion* 40
             (1998), Nr. 8, S. 1429–1488

[II88]   ITOH, Sanae-I. ; ITOH, Kimitaka: Model of *L* to *H*-Mode Transi-
             tion in Tokamak. In: *Phys. Rev. Lett.* 60 (1988), May, Nr. 22, S.
             2276–2279

[IKT+97]   INAGAKI, S. ; KITAJIMA, S. ; TAKAYAMA, M. ; NAKAMURA, E. ;
             YOSHIDA, T. ; WATANABE, H.: Influence of Biased Electrode on
             Plasma Confinement in the Tohoku University Heliac. In: *Jpn. J.
             Appl. Phys.* 36 (1997), S. 3697–3706

[JOWB98]   JACHMICH, S ; OOST, G V. ; WEYNANTS, R R. ; BOEDO, J A.:
             Experimental investigations on the role of flow shear in improved
             confinement. In: *Plasma Physics and Controlled Fusion* 40 (1998),
             Nr. 6, S. 1105–1113

[Ker75]   KERST, D.W.: In: *Bull. Am. Phys. Soc.* 20 (1975), S. 1334 ff.

[KGK+01]   KIRNEV, G.S. ; GRASHIN, S.A. ; KHIMCHENKO, L.N. ; TIM-
             CHENKO, N.N. ; VANOOST, G.: First Results of Biasing Experi-
             ments on the T-10 Tokamak. In: *Czechoslovak Journal of Physics*
             51 (2001), S. 1011–1019

[KTT+04]   KITAJIMA, S. ; TAKAHASHI, H. ; TANAKA, Y. ; UTOH, H. ;
             SASAO, M. ; TAKAYAMA, M. ; NISHIMURA, K. ; INAGAKI, S.
             ; YOKOYAMA, M.: LH Transition by a Biased Hot Cathode in
             the Tohoku University Heliac. In: *20th IAEA Fusion Energy Con-
             ference, Vilamoura, Portugal*, 2004

[KTT+06a]   KITAJIMA, S. ; TAKAHASHI, H. ; TANAKA, Y. ; UTOH, H. ;
             SASAO, M. ; TAKAYAMA, M. ; NISHIMURA, K. ; INAGAKI, S.
             ; YOKOYAMA, M.: LH transition by a biased hot cathode in the
             Tohoku University Heliac. In: *Nuclear Fusion* 46 (2006), Nr. 2,
             S. 200–206

[KTT+06b]   KITAJIMA, S ; TAKAHASHI, H ; TANAKA, Y ; UTOH, H ;
             YOKOYAMA, M ; INAGAKI, S ; SUZUKI, Y ; NISHIMURA, K ;
             SHINDE, J ; OGAWA, M ; IWAZAKI, K ; AOYAMA, H ; OKAMOTO,
             A ; SHINTO, K ; SASAO, M: Spontaneous L–H transitions
             under marginal hot cathode biasing in the Tohoku University He-
             liac. In: *Plasma Physics and Controlled Fusion* 48 (2006), Nr.
             5A, S. A259–A267

[LA08]   LANGLEY, S.P. ; ABBOT, C.G.: *Annals of the Astrophysical Ob-
             servatory of the Smithsonian Institution, Volume I.* Government
             Printing Office, Washington D.C, 1908

[Laq]   LAQUA, H. *private communication*

[Lar95]   LARMOR, Joseph: A Dynamical Theory of the Electric and Lu-
             miniferous Medium. Part II. Theory of Electrons. In: *Philosoph-*

ical Transactions of the Royal Society of London. A 186 (1895), S. 695–743. – ISSN 0264–3820

[Law55]   LAWSON, J.D: Some Criteria for a Useful Thermonuclear Reactor / A.E.R.E report GP/R 1807. 1955. – Forschungsbericht

[Lis05]   LISCHTSCHENKO, O.: *Poloidal Plasma Rotation and Biasing in the WEGA Stellarator*, Ernst-Moritz-Arndt-Universität Greifswald, Diplomarbeit, 2005

[LSS02]   LECHTE, Carsten ; STOBER, Jennifer ; STROTH, Ulrich: Plasma parameter limits of magnetically confined low temperature plasmas from a combined particle and power balance. In: *Physics of Plasmas* 9 (2002), Nr. 6, S. 2839–2846

[Man94]   MANK, G. (Hrsg.) ; Forschungszentrum Jülich and Ecole Royale Militaire-Koninklijke Militaire School (Veranst.): *Contributions to the Workshop "Edge Biasing on TEXTOR"*. 1994

[Mar08]   MARSEN, S.: *The Spatio-temporal Structure of Electrostatic Turbulence in the WEGA Stellarator*, Ernst-Moritz-Arndt-Universität Greifswald, Diss., 2008

[MVA⁺91]   MAST, K. F. ; VALLET, J. C. ; ANDELFINGER, C. ; BETZLER, P. ; KRAUS, H. ; SCHRAMM, G.: A low noise highly integrated bolometer array for absolute measurement of VUV and soft x radiation. In: *Review of Scientific Instruments* 62 (1991), Nr. 3, S. 744–750

[OLW03]   OTTE, M. ; LINGERTAT, J. ; WAGNER, F.: Operation of the WEGA Stellarator with Vertical Field and Compensation Coils. In: *30th EPS Conference on Controlled Fusion and Plasma Physics*, 2003

[Ott00]   OTTE, M.: *Experimentelle Untersuchungen der Elektronenkinetik schwach ionisierter stossbestimmter Plasmen unter räumlich inhomogenen Bedingungen*, Ernst- Moritz- Arndt Universität Greifswald, Diss., 2000

[PK73]   PREINHAELTER, J. ; KOPECKY, V.:   Penetration Of High-
            Frequency Waves Into A Weakly Inhomogeneous Magnetized
            Plasma At Oblique-Incidence And Their Transformation To Bern-
            stein Modes. In: *Journal Of Plasma Physics* 10 (1973), Nr. AUG,
            S. 1–12

[PLW+07]   PODOBA, Y. ; LAQUA, H.P. ; WARR, G. B. ; SCHUBERT, M. ;
            OTTE, M. ; MARSEN, S. ; WAGNER, F. ; HOLZHAUER, E.: Direct
            Observation of Electron-Bernstein Wave Heating by O-X-B-Mode
            Conversion at Low Magnetic Field in the WEGA Stellarator. In:
            Physical Review Letters 98 (2007), Nr. 25, S. 255003

[Pod]   PODOBA, Y. *private communication*

[Pod06]   PODOBA, Y.: *Radio frequency heating on the WEGA stellarator*,
            Ernst- Moritz- Arndt- Universität Greifswald, Diss., 2006

[Ram05]   RAMISCH, M.: *Scaling and Manipulation of Turbulent Structures
            in the Torsatron TJ-K*, Hans- Christian- Anders- Universität Kiel,
            Diss., 2005

[Rei98]   REINMÜLLER, K.:   *Emittierende Sonden und Entstehung
            von Hot Spots - Untersuchung des Kontaktes zwischen Plasma
            und elektronen-emittierender Wand durch Teilchensimulation mit
            Model für Stossprozesse*, Technische Universität München, Diss.,
            1998

[RFB04]   RIEGG, S. ; FANTZ, U. ; BEHRINGER, K. *Vergleich spektroskopis-
            cher Methoden zur Bestimmung von n_e und T_e am Stellarator
            WEGA*. Frühjahrstagung der DPG, Kiel. March 2004

[RHB+99]   RHODES, T.L. ; HINTON, F.L. ; BURRELL, K.H. ; GROEBNER,
            R.J. ; PEEBLES, W.A. ; RETTIG, C.L. ; WADE, M.R.: Prompt
            radial electric field response to neutral beam injection. In: *Nuclear
            Fusion* 39 (1999), Nr. 8, S. 1051–1056

[RLB+97]   ROHDE, V. ; LAUX, M. ; BACHMANN, P. ; HERRMANN, A. ;
            WEINLICH, M.: Direct measurement of the plasma potential in
            the edge of ASDEX Upgrade using a self emitting probe. In:

Journal of Nuclear Materials 241-243 (1997), Februar, S. 712–715

[RSB+98]   RYTER, F ; SUTTROP, W ; BRÜSEHABER, B ; KAUFMANN, M ; MERTENS, V ; MURMANN, H ; PEETERS, A G. ; STOBER, J ; SCHWEINZER, J ; ZOHM, H ; TEAM, ASDEX U.: H-mode power threshold and transition in ASDEX Upgrade. In: *Plasma Physics and Controlled Fusion* 40 (1998), Nr. 5, S. 725–729

[RTDG02]   RYTER, F. ; THE H-MODE THRESHOLD DATABASE GROUP: Progress of the International H-Mode Power Threshold Database Activity. In: *Plasma Physics and Controlled Fusion* 44 (2002), S. A415–421

[RTDWG98]   RIGHI, E ; MODE THRESHOLD DATABASE WORKING GROUP, The ITER H.: Scaling of the H-mode power threshold for ITER. In: *Plasma Physics and Controlled Fusion* 40 (1998), Nr. 5, S. 857–861

[RTH+97]   RICHARD, N. ; TERREAULT, B. ; HADDAD, E. ; GUNN, J. ; ABEL, G. ; CHIU, S. ; GAUVREAU, J. L. ; MAI, H. H. ; ZUZAK, W. W.: Retention of Ne and N2 in the closed and pumped TdeV divertor with attached and detached plasmas. In: *Journal of Nuclear Materials* 241-243 (1997), S. 760 – 764. – ISSN 0022–3115

[SC89]   SHAING, K. C. ; CRUME, E. C.: Bifurcation theory of poloidal rotation in tokamaks: A model for L-H transition. In: *Phys. Rev. Lett.* 63 (1989), Nov, Nr. 21, S. 2369–2372

[Sch99]   SCHUBERT, M.: *Eichung schneller Metallbolometer und Messung der Plasmastrahlung am Stellarator W7-AS*, Technische Universität München, Diplomarbeit, 1999

[SFN+06]   SILVA, C. ; FIGUEIREDO, H. ; NEDZELSKIY, I. ; GONÇALVES, B. ; VARANDAS, C.A.F.: Control of the Edge Turbulent Transport by Emissive Electrode Biasing on the Tokamak ISTTOK. In: *Plasma Physics and Controlled Fusion* 48 (2006), S. 727–744

[SGH+96]   STROTH, U ; GIANNONE, L ; HARTFUSS, H-J ; THE ECH GROUP ; THE W7-AS TEAM: Fast transport changes and power degrada-

tion in the W7-AS stellarator. In: *Plasma Physics and Controlled Fusion* 38 (1996), Nr. 4, S. 611–618

[SIB⁺08]   SCHRITTWIESER, Roman ; IONITA, Codrina ; BALAN, Petru ; GSTREIN, Ramona ; GRULKE, Olaf ; WINDISCH, Thomas ; BRANDT, Christian ; KLINGER, Thomas ; MADANI, Ramin ; AMARANDEI, George ; SARMA, Arun K.: Laser-heated emissive plasma probe. In: *Review of Scientific Instruments* 79 (2008), Nr. 8, S. 083508

[SIHMTDWG00] SNIPES, J.A. ; THE INTERNATIONAL H-MODE THRESHOLD DATABASE WORKING GROUP: Latest Results on the H-Mode Threshold Using the International H-Mode Threshold Database. In: *Plasma Physics and Controlled Fusion* 42 (2000), S. A299–A308

[SII⁺01]   STROTH, U. ; ITOH, K. ; ITOH, S.-I. ; HARTFUSS, H. ; LAQUA, H. ; THE ECRH TEAM ; THE W7-AS TEAM: Internal Transport Barrier Triggered by Neoclassical Transport in W7-AS. In: *Phys. Rev. Lett.* 86 (2001), Jun, Nr. 26, S. 5910–5913

[SLM⁺91]   SCHAFFER, M.J. ; LIPPMANN, S.I. ; MAHDAVI, M.A. ; PETRIE, T.W. ; STAMBAUGH, R.D. ; HOGAN, J. ; KLEPPER, C.C. ; MIODUSZEWSKI, P. ; OWEN, L. ; HILL, D.N. ; RENSINK, M. ; BUCHENAUER, D.: Particle control in the DIII-D advanced divertor. In: *Fusion Engineering, 1991. Proceedings., 14th IEEE/NPSS Symposium on* (1991), Sep-3 Oct, S. 197–200 vol.1

[Spi51]   SPITZER, L.: U.S. Atomic Energy Commission Report, No. NYO-993 (PM-S-1). 1951. – Forschungsbericht

[SRB⁺96]   SHATS, M. G. ; RUDAKOV, D. L. ; BLACKWELL, B. D. ; BORG, G. G. ; DEWAR, R. L. ; HAMBERGER, S. M. ; HOWARD, J. ; SHARP, L. E.: Improved Particle Confinement Mode in the H-1 Heliac Plasma. In: *Phys. Rev. Lett.* 77 (1996), Nov, Nr. 20, S. 4190–4193

[SS96]   SIEBENFORCHER, A. ; SCHRITTWIESER, R.: A new simple emissive probe. In: *Review of Scientific Instruments* 67 (1996), Nr. 3, S. 849–850

[Sta95a]   STAEBLER, G. M.: Divertor bias experiments. In: *Journal of Nuclear Materials* 220-222 (1995), April, S. 158–170

[Sta95b]   STANGEBY, P C.: A problem in the interpretation of tokamak Langmuir probes when a fast electron component is present. In: *Plasma Physics and Controlled Fusion* 37 (1995), Nr. 9, S. 1031–1037

[Str93]   STRINGER, T.E.: Explanation of the L-H mode transition induced by applied voltage. In: *Nuclear Fusion* 33 (1993), Nr. 9, S. 1249–65

[TBF⁺89]   TAYLOR, R. J. ; BROWN, M. L. ; FRIED, B. D. ; GROTE, H. ; LIBERATI, J. R. ; MORALES, G. J. ; PRIBYL, P. ; DARROW, D. ; ONO, M.: H-mode behavior induced by cross-field currents in a tokamak. In: *Phys. Rev. Lett.* 63 (1989), Nov, Nr. 21, S. 2365–2368

[Ten97]   TENDLER, M: Different scenarios of transitions into improved confinement modes. In: *Plasma Physics and Controlled Fusion* 39 (1997), Nr. 12B, S. B371–B382

[Toi96]   TOI, K. et a.: Transition behaviour in the H-mode of the CHS heliotron/torsatron. In: *Plasma Physics and Controlled Fusion* 38 (1996), Nr. 8, S. 1289–1293

[UAB⁺91]   UCKAN, T. ; ACETO, S.C. ; BAYLOR, L.R. ; BELL, J.D. ; BIGELOW, T. ; ENGLAND, A.C. ; HARRIS, J.H. ; ISLER, R.C. ; JERNIGAN, T.C. ; LYON, J.F. ; MIODUSZEWSKI, P.K. ; MURAKAMI, M. ; RASMUSSEN, D.A. ; WILGEN, J.B. ; WING, W.R. ; ZIELINSKI, J.J.: Biasing Experiments on the ATF Torsatron / 18th European Conference on Controlled Fusion and Plasma Physics, Berlin (Germany). 1991. – Forschungsbericht

[VAA⁺03]   VANOOST, G. ; ADAMEK, J. ; ANTONI, J. ; BALAN, P. ; BOEDO, J. A. ; DEVYNCK, P. ; DURAN, I. ; ELISEEV, L. ; GUNN, J. P. ; HRON, M. ; IONITA, C. ; JACHMICH, S. ; KIRNEV, G. S. ; MARTINES, E. ; MELNIKOV, A. ; SCHRITTWIESER, R. ; SILVA, C. ; STOCKEL, J. ; TENDLER, M. ; VARANDAS, C. ; VANSCHOOR, M.

; VERSHKOV, V. ; WEYNANTS, R. R.: Turbulent transport reduction by E×B velocity shear during edge plasma biasing: recent experimental results. In: *Plasma Physics and Controlled Fusion* 45 (2003), Nr. 5, S. 621–643

[VGM+01] VANOOST, G. ; GUNN, J.P. ; MELNIKOV, A. ; STÖCKEL, J. ; TENDLER, M.: The Role of Radial Electric Fields in the Tokamaks TEXTOR-94, CASTOR, and T-10. In: *Czechoslovak Journal of Physics* 51 (2001), S. 957–975

[Vor97] VORONOV, G.S.: A Practical Fit Formula for Ionization Rate Coefficients of Atoms and Ions by Electron Impact: Z = 1-28. In: *Atomic Data and Nuclear Data Tables* 65 (1997), S. 1–35

[VSG+01] VANOOST, G. ; STOCKEL, J. ; GUNN, J. ; ADAMEK, J. ; DURAN, I. ; HORACEK, J. ; HRON, M. ; JAKUBKA, K. ; KRYSKA, L. ; ZACEK, F.: Direct Measurements of the ExB Flow and its Impact on Edge Turbulence in the CASTOR Tokamak. In: *28th EPS Conference on Controlled Fusion and Plasma Physics, Funchal*, 2001

[WBB+82] WAGNER, F. ; BECKER, G. ; BEHRINGER, K. ; CAMPBELL, D. ; EBERHAGEN, A. ; ENGELHARDT, W. ; FUSSMANN, G. ; GEHRE, O. ; GERNHARDT, J. ; GIERKE, G. v. ; HAAS, G. ; HUANG, M. ; KARGER, F. ; KEILHACKER, M. ; KLÜBER, O. ; KORNHERR, M. ; LACKNER, K. ; LISITANO, G. ; LISTER, G. G. ; MAYER, H. M. ; MEISEL, D. ; MÜLLER, E. R. ; MURMANN, H. ; NIEDERMEYER, H. ; POSCHENRIEDER, W. ; RAPP, H. ; RÖHR, H.: Regime of Improved Confinement and High Beta in Neutral-Beam-Heated Divertor Discharges of the ASDEX Tokamak. In: *Phys. Rev. Lett.* 49 (1982), Nov, Nr. 19, S. 1408–1412

[Wer] WERNER, A.: *w7 code.* – private communications

[WOB+92] WEYNANTS, R.R. ; VAN OOST, G. ; BERTSCHINGER, G. ; BOEDO, J. ; BRYS, P. ; DELVIGNE, T. ; DIPPEL, K.H. ; DURODIE, F. ; EURINGER, H. ; FINKEN, K.H. ; GRAY, D.S. ; HEY, J.D. ; HILLIS, D.L. ; HOGAN, J.T. ; KONEN, L. ; LENERS, R. ; MESSIAEN, A.M. ; POSPIESZCZYCK, A. ; SAMM, U. ; SCHORN, R.P. ;

Schweer, B. ; Telesca, G. ; van Nieuwenhove, R. ; Vandenplas, P.E.: Confinement and profile changes induced by the presence of positive or negative radial electric fields in the edge of the TEXTOR tokamak. In: *Nuclear Fusion* 32 (1992), Nr. 5, S. 837–853

[Wol03]   Wolf, R C.: Internal transport barriers in tokamak plasmas*. In: *Plasma Physics and Controlled Fusion* 45 (2003), Nr. 1, S. R1–R91

[ZOG05]   Zhang, D. ; Otte, M. ; Giannone, L.: Bolometer Results in the Long- Microwave- Heated WEGA Stellarator. In: *Proceedings of the International Conference on Research and Applications of Plasmas (PLASMA 2005)*, 2005

Eigenständigkeitserklärung

Hiermit erkläre ich, dass diese Arbeit bisher von mir weder an der Mathematisch-Naturwissenschaftlichen Fakultät der Ernst-Moritz-Arndt-Universität Greifswald, noch an einer anderen wissenschaftlichen Einrichtung zum Zwecke der Promotion eingereicht wurde.

Ferner erkläre ich, dass ich diese Arbeit selbständig verfaßt habe und keine anderen als die darin angegebenen Hilfsmittel benutzt habe.

Greifswald, im November 2008

Lebenslauf von Oliver Lischtschenko

Geboren am 18. Dezember 1979 in Berlin-Spandau

Familienstand: ledig, 2 Kinder

Schulbildung

bis 1996	Gymnasium Pampow, Pampow. Sekundarstufe 1.
1996 - 1997	Hutchinson High School, Hutchinson, KS (USA). Abschluss: High School Graduate.
1997 - 1999	Gymnasium Pampow, Pampow. Sekundarstufe 2. Abschluss: Abitur (Allgemeine Hochschulreife)

Studium

WS 2000/2001	Immatrikulation an der Ernst-Moritz-Arndt-Universität Greifswald. Studienrichtung: Physik, Diplom
ab SS 2003	Vertiefungsrichtung: *Plasmaphysik*
ab WS 2003/2004	Praxissemester am Max-Planck-Institut für Plasmaphysik, Greifswald. Thema: „*Einrichtung des Messplatzes zur Dopplerverbreiterten Absorptionsspektroskopie mit durchstimmbarem Diodenlaser und Transfer an Experiment WEGA*"
ab WS 2004/2005	Diplomarbeit am Max-Planck-Institut für Plasmaphysik, Greifswald. Thema: „*Poloidal Rotation and Biasing in the WEGA Stellarator*"
2005	Studienabschluss: Diplom-Physiker (dipl. phys.)

Promotion

2005 - 2008	Doktorand am Max-Planck-Institut für Plasmaphysik Thema der Doktorarbeit: „*Edge Biasing in the WEGA Stellarator*"

Lehrtätigkeit

2006   Durchführung des Physikalischen Praktikums für Fort-
geschrittene, Versuch: „*Wellen im Plasma (IPP)*"

Sommerschulen und Konferenzen

69. Frühjahrstagung der Deutschen Physikalischen Gesellschaft, Berlin, 2005.

70. Frühjahrstagung der Deutschen Physikalischen Gesellschaft, Augsburg, 2006.

IPP Summer University for Plasma Physics, Greifswald, September 2007.

72. Frühjahrstagung der Deutschen Physikalischen Gesellschaft, Darmstadt, 2008.

Konferenzbeiträge

Poster

Lischtschenko, O.; König, R.; Otte, M.; Wagner, F.: Edge Biasing in the WEGA Stellarator, In: *69. Frühjahrstagung der Deutschen Physikalischen Gesellschaft, Berlin*, Berlin, Germany, 2006.

Lischtschenko, O.; König, R.; Otte, M.; Wagner, F.: Poloidale Plasmarotation im Stellarator WEGA, In: *70. Frühjahrstagung der Deutschen Physikalischen Gesellschaft, Augsburg*, Augsburg, Germany, 2006.

Lischtschenko, O.; König, R.; Otte, M.; Wagner, F.: Plasmapolarisation mit Graphit-Sonden am WEGA Stellarator, In: *72. Frühjahrstagung der Deutschen Physikalischen Gesellschaft, Darmstadt*, Darmstadt, Germany, 2008.

Veröffentlichungen

Als Koautor

Warr; G. B.; Chmyga, O.; Holzhauer, E.; Howard, J.; Kasparek, W.; Keil, D.; König, R.; Laqua, H. P.; Laux, M.; Lingertat, J.; Lischtschenko, O.; Marsen, S.; Otte, M.; Podoba, Y.; Schubert, M.; Wagner, F.; Weller, A.; Zhang, D.; Zhezhera, O.: Overview of WEGA Stellarator: Results and Plans, In: *7th Australia-Japan Workshop on Plasma Physics and Diagnostics*, Toki, Japan, 2005.

Otte, M.; Lischtschenko, O.; Marsen, S.; Schubert, M.; Podoba, Y.Y. ;Wagner, F.; Warr, G.B.; Krupnik, L.I.; Melnikov, A.V.; Zhezhera, A.I.: Five Years of WEGA Operation at IPP Greifswald. In: *Stellarator News 106 (2006)*, 2006.

Warr, G.B.; Laqua, H.P.; Assmus, D.; Kasparek, W.; Keil, D.; Lischtschenko, O.; Marsen, S.; Otte, M.; Schubert, M.; Wagner, F.: New 28 GHz Plasma ECR Heating System for the WEGA Stellarator, In: *33rd European Physical Society Conference on Plasma Physics*, Rome, 2006.

Otte, M.; Andruczyk, D.; Komarov, A.; Kozachek, A.; Krupnik, L.; Laqua, H.P.; Lischtschenko, O.; Marsen, S.; Podoba, Y.Y.; Schubert, M.; Wagner, F.; Warr, G.B.; Zhezhera, A.: Experimental Results from the WEGA Stellarator, In: *34th European Physical Society Conference on Plasma Physics*, Warsaw, 2007.

Otte, M.; Andruczyk, D.; Holzhauer, E.; Howard, J.; König, R.; Krupnik, L.; Laqua, H. P.; Lischtschenko, O.; Marsen, S.; Schacht, J.; Urban, J.; Podoba, Y. Y.; Preinhalter, J.; Wagner, F.; Warr, G. B.; Zhezhera, A.: The WEGA Stellarator: Results and Prospects, In: *PLASMA 2007: The International Conference Research and Application of Plasmas, 4th German-Polish Conference on Plasma Diagnostics for Fusion and Applications, 6th French-Polish Seminar on Thermal Plasma in Space and Laboratory*, Greifswald, 2007.

Vorträge

Lischtschenko, O.: Poloidal Plasma Rotation in WEGA, In: *W7 seminar*, Greifswald/Garching, June 20th, 2006.

Lischtschenko, O.: Recent Results of Edge Biasing in WEGA, In: *IMPRS Kolloquium*, Greifswald, April 26th, 2007.

Lischtschenko, O.: Biasing Experiments in the WEGA Stellarator, In: *IMPRS Kolloquium*, Greifswald, April 10th, 2008.

Lischtschenko, O.: Edge Biasing in the WEGA Stellarator, In: *Invitation to Upper Austrian Research GmbH*, Linz, August 28th,2008.